Analysis of the ocean dynamics in a wind-jet region using high-resolution models

Laura Ràfols

Barcelona, July 2018

A thesis submitted for the degree of

Doctor in marine sciences

Thesis directors

Manuel Espino

Manel Grifoll

Laboratori d'Enginyeria Marítima
UNIVERSITAT POLITÈCNICA DE CATALUNYA

meteo.cat Servei Meteorològic de Catalunya

DOCTORATS INDUSTRIALS

Dedicated to my family.

Acknowledgements

En primer lloc al Manuel Espino, per proposar-me que em presentés com a candidata a aquest projecte de Doctorat Industrial. També pel seu seguiment, preocupació, implicació i ajuda durant el llarg camí del doctorat.

A l'Abdel Sairouni per obrir-me les portes del Servei Meteorològic de Catalunya (SMC) i per confiar en el projecte i en mi.

Al Manel Grifoll per l'ajuda i seguiment que m'ha proporcionat, però també per les seves rigoroses revisions, que cal reconèixer que m'han permès aprofundir en el meu coneixement i millorar la recerca realitzada.

Al Pablo Cerralbo i a l'Elena Pallarés, companys de fatigues del LIM-UPC, per l'ajuda que m'han donat amb els models numèrics i pels moments viscuts en el despatx, als quals més tard s'ha afegit la Marta.

Als companys de l'SMC (Jordis, Manel, Vicent, J.R., Roger, Toni i Aleix) pels moments compartits durant els esmorzars i la companyia en la tranquil·la àrea de RAM. Cal fer una menció especial al Manel, company d'onatge, que ha hagut de suportar les meves peticions de dades.

A la gent de l'NT3, als que encara seguiu per allà i als que no, (Pablo, Elena, Arnel, Martes, Jaime, Borja, Jonathan, Augusto i Joel) per les estones divertides compartides, monito-monitas, dinars i postres. He de dir que trobo a faltar les postres de l'NT3...

A l'Edgar Olivares, company de màster i fatigues doctorals, pels nostres cafès i dinars on ens hem compadit l'un de l'altre explicant-nos els nostres "progressos" en la tesi.

Al meu tiet Roger per les seves magnífiques fotos.

Als amics per donar-me ànims i distreure'm del meu dia a dia.

Als de casa (mare, pare i Clara) per aguantar-me, per aconseguir distreure'm i fer que aquests anys

de doctorat hagin estat més suportables, tot i els alts i baixos que hem passat.

I finalment, a l'Albert Cardús per aguantar-me, per donar-me suport, per fer-me riure inclús quan no em venia de gust, pels moments viscuts, per tot.

Abstract

The water currents and the wave field at the Catalan coast, in the Northwestern Mediterranean Sea, are investigated. However, the main research is focused at the northern margin of the Ebro Shelf, where there is a relatively high amount of data for study purposes and where episodes of strong northwesterly wind occur. In such cases, the wind is channeled through the Ebro Valley and intensifies upon reaching the sea, resulting in a wind jet.

First, the wind-jet response in terms of water circulation and vertical density structure is investigated using the Regional Ocean Modeling System (ROMS) numerical model. The numerical outputs agree with water current observations from a high frequency (HF) radar. Additionally, water temperature, sea level and wind measurements are also used for the skill assessment of the model. For the wind-jet episodes, the numerical results show a well-defined two-layer circulation in the cross-shelf direction, with the surface currents in the direction of the wind. This pattern is consistent with sea level set-down due to the wind effect. The comparison of the vertical structure response for different episodes reveals that the increase of stratification leads to an onshore displacement of the transition from inner shelf to mid-shelf. In general, the cross-shelf momentum balance during a wind-jet episode exhibits a balance between the frictional terms and the pressure gradient in shallow waters, shifting to a balance between the Coriolis force and the wind stress terms in deeper waters.

Secondly, the wind-wave generation, development and fading at the wind-jet region is investigated. The third-generation wave model Simulating WAves Nearshore (SWAN) is implemented and fed by high-resolution wind fields. A combination of buoy and HF radar data are used for model validation, resulting in a reasonable level of agreement. The numerical results characterize the wind-wave evolution during a wind jet. A bimodal spectrum is observed due to the interaction of swell and sea systems. The wave directional spreading exhibits lower values at the wind-jet axis. A reliability analysis of the wave data from a HF radar deployed at the region is also carried out. It is the first time that such data is used and the results show that the post-processed data is rather good but present two main drawbacks: the high amount of data gaps and the homogenization of

the samples along a range cell, which might result in unrealistic measures in areas with big wave gradients.

Thirdly, the Wave–Current Interactions (WCIs) are investigated. The aim is to validate the implemented coupled system and investigate the impact of WCIs on the hydrodynamics of a wind-jet region. The Coupled Ocean-Atmosphere-Wave-Sediment Transport (COAWST) Modeling System, which uses ROMS and SWAN models, is used. Results from uncoupled numerical models are compared with a two-way coupling simulation. The results do not show substantial differences in the water current field between the coupled and the uncoupled runs. The main effect observed when the waves are considered is in the water column stratification, due to the turbulent kinetic energy injection and the enhanced surface stress, leading a larger mixed-layer depth. Additionally, when the water currents are considered, the modeled wave period significantly improves and the wave energy (and thus the significant wave height) decreases when the current flows in the same direction as the waves propagate.

Finally, with the aim of forecasting waves and currents at the Catalan coast, an operational forecasting system is designed and implemented at the Meteorological Service of Catalonia (SMC). The system design is based on the model configurations used previously to investigate the ocean dynamics at the wind-jet region. In particular, the wave forecasting system is implemented by means of the SWAN model with an horizontal resolution up to 3 km and the hydrodynamics forecasting system is implemented using the ROMS model in five coastal domains with a horizontal resolution of 400 m. The numerical results have been validated using in-situ buoy measurements, HF radar data and satellite data, showing a reasonable agreement. As in any forecasting system, the systems presented here require a daily monitoring and a follow-up focused on improving them. In this sense, some potential future works are proposed.

Overall, this thesis has allowed to analyze the North Ebro shelf hydrodynamic response to a wind jet in terms of waves and currents, study the coupling effects of waves on currents and vice versa and determine that the numerical models used in this study are able to reproduce patterns that are physically reliable. Finally, the knowledge gained with this research has allowed to implement a forecasting system.

Resum

S'investiguen els corrents marins i l'onatge a la costa catalana, al nord-oest del Mar Mediterrani. No obstant, la recerca principal es centra al marge nord de la plataforma de l'Ebre, on hi ha una quantitat relativament alta de dades útils per a la investigació i on tenen lloc episodis de fort vent del nord-oest. En aquests casos, el vent és canalitzat al llarg de la vall de l'Ebre i s'intensifica quan arriba al mar, resultant en un *wind jet*.

En primer lloc, s'estudia la resposta del *wind jet* en termes de circulació de l'aigua i de l'estructura vertical de la densitat utilitzant el model numèric Regional Ocean Modeling System (ROMS). Els resultats numèrics són coherents amb els corrents mesurats amb un radar d'alta freqüència. A més, també s'utilitzen mesures de temperatura de l'aigua, nivell del mar i vent per validar el model. Pels episodis de *wind jet*, els resultats numèrics presenten una circulació de dues capes ben definida en la direcció perpendicular a la costa, amb els corrents superficials en la direcció del vent. Aquest patró és consistent amb la reducció del nivell del mar deguda a l'efecte del vent. La comparació de la resposta de l'estructura vertical per a diferents episodis revela que l'increment d'estratificació comporta un desplaçament cap a la costa de la regió de transició entre la plataforma interna i la plataforma mitja. En general, el balanç del moment durant un episodi de *wind jet* en la direcció perpendicular a la costa mostra un balanç entre els termes friccionals i el gradient de pressió en aigües poc profundes, canviat a un balanç entre els termes de la força de Coriolis i la tensió del vent en aigües més profundes.

En segon lloc, s'investiga la generació, el desenvolupament i el decaïment de l'onatge en la regió de *wind jets*. S'implementa el model de tercera generació Simulating WAves Nearshore (SWAN) alimentat amb vents d'alta resolució. S'utilitza una combinació de dades de boies i d'un radar d'alta freqüència per a validar el model, proporcionant un nivell de concordança raonable. Els resultats numèrics caracteritzen l'evolució de l'onatge durant un *wind jet*. S'observa un espectre bimodal a causa de la interacció entre el mar de vent i el mar de fons. La dispersió direccional de l'onatge mostra valors inferiors en l'eix del *wind jet*. També es realitza una anàlisi de la fiabilitat de les dades d'onatge que proporciona un radar d'alta freqüència situat a la regió. És el primer cop que

s'utilitzen aquestes dades i els resultats mostren que les dades postprocessades són prou bones però presenten dos inconvenients principals: l'elevada quantitat de buits de dades i l'homogeneïtzació de les mostres al llarg d'una cel·la de rang, fet que podria resultar en mesures poc realistes en zones amb importants gradients d'onatge.

En tercer lloc, s'investiguen les interaccions ona–corrent . L'objectiu és validar el sistema acoblat implementat i investigar l'impacte de les interaccions ona–corrent en la hidrodinàmica d'una zona de *wind jets*. S'utilitza el sistema Coupled Ocean-Atmosphere-Wave-Sediment Transport (COAWST), el qual utilitza els models ROMS i SWAN. Es comparen els resultats dels models no acoblats amb els d'una simulació acoblada. Els resultats no mostren diferències substancials en el camp de corrents entre la simulació no acoblada i l'acoblada. El principal efecte observat quan es té en consideració l'onatge és en l'estratificació de la columna d'aigua, deguda a la injecció d'energia cinètica turbulenta i l'increment de la tensió superficial, comportant una major profunditat de la capa de mescla. A més, quan es consideren els corrents, el període de l'onatge millora i l'energia de l'onatge (i per tant l'alçada d'ona significant) disminueix quan el corrent flueix en la mateixa direcció que es propaguen les ones.

Finalment, amb l'objectiu de predir onatge i corrents a la costa catalana, s'ha dissenyat i implementat un sistema operacional de predicció al Servei Meteorològic de Catalunya (SMC). El disseny del sistema es basa en la configuració dels models utilitzats prèviament per a investigar la dinàmica oceànica a la regió de *wind jet*. En particular, el sistema de predicció d'onatge s'implementa mitjançant el model SWAN amb una resolució horitzontal de 3 km i el sistema de predicció de corrents s'implementa utilitzant el model ROMS en cinc dominis costaners amb una resolució horitzontal de 400 m. Els resultats numèrics s'han validat mitjançant mesures de boies, dades de radar d'alta freqüència i dades de satèl·lit, mostrant un acord raonable. Com en tot sistema de predicció, els sistemes que es presenten aquí requereixen un monitoratge diari i un seguiment enfocat en millorar-los. En aquest sentit, es proposen treballs futurs potencials.

En general, aquesta tesi ha permès analitzar la resposta hidrodinàmica a un *wind jet* a la part nord de la plataforma de l'Ebre en termes d'onatge i corrents, estudiar els efectes d'acoblament que té l'onatge sobre els corrents i viceversa i determinar que els models numèrics utilitzats en aquest estudi són capaços de reproduir comportaments que són físicament confiables. Finalment, el coneixement adquirit amb aquesta recerca ha permès implementar un sistema de predicció.

Publications

Peer Reviewed International Journals

Grifoll, M., Navarro, J., Pallares, E., Ràfols, L., Espino, M., and Palomares, A. (2016). Ocean-atmosphere-wave modelling of a wind-jet (Ebro shelf; NW Mediterranean Sea). *Nonlinear Processes in Geophysics*, 23:143-158. doi:10.5194/npg-23-143-2016.

Ràfols, L., Pallares, E., Espino, M., Grifoll, M., Sánchez-Arcilla, A., Bravo, M., and Sairouní, A. (2017). Wind-wave characterization in a wind-jet region: the Ebro Delta case. *Journal of Marine Science and Engineering*, 5(1), 12. doi:10.3390/jmse5010012.

Ràfols, L., Grifoll, M., Jordà, G., Espino, M., Sairouní, A. and Bravo, M. (2017). Shelf circulation induced by an orographic wind jet. *Journal of Geophysical Research: Oceans*, 122. doi:10.1002/2017JC012773.

Publications under review

Ràfols, L., Grifoll, M., Espino, M. (expected 2018). Wave–Current Interactions in a Wind-jet Region. Under review.

Conference contributions

Pallares, E., Ràfols, L., Espino, M., Grifoll, M., López, J., Bravo, M., Moré, J., Sairouní, A., Garcia, M., Marzeddu, A., Gracia, V. and Sánchez-Arcilla, A. (2014). High resolution ocean modeling forecast for coastal early warning system in the Catalan Coast. *7th EuroGOOS Conference: Operational Oceanography for Sustainable Blue Growth.*

Ràfols, L., Sairouní, A., Bravo, M., Espino, M. and Grifoll, M. (2015). Sea level and current validation for an early warning coastal system on the Catalan coast (NW Mediterranean Sea). *Geophysical Research Abstracts*, 17, EGU2015-9669-1.

Ràfols, L., Grifoll, M., Espino, M., Sairouni, A., Bravo, M. (2016). Study of the local circulation induced by a wind jet at the northern margin of the Ebre Shelf. *IV Encuentro Oceanografía Física Española.*

Ràfols, L., Grifoll, M., Espino, M., Cerralbo, P., Sairouni, A., Bravo, M. (2017). Wave-Current Interactions in a wind-jet region. *Geophysical Research Abstracts*, 19, EGU2017-15352-1.

Cerralbo, P., Ràfols, L., Espino, M., Ahsbahs,T., Badger, M., Grifoll, M. and Sánchez-Arcilla, A. (2018). Evaluating the Sentinel 1 wind product quality near the coast: the role of high resolution numerical models. *Geophysical Research Abstracts*, 20, EGU2018-12967.

Espino, M., Ràfols, L., Grifoll, M. and Sánchez-Arcilla, A. (2018). Wave-Current Interactions in a wind-jet region. *V Encuentro Oceanografía Física Española.*

Contents

List of Figures

Chapter I

Chapter II

Chapter III

Chapter IV

Chapter V

Chapter VI

List of Tables

Chapter II

Chapter III

Chapter IV

Chapter V

Chapter VI

Nomenclature

Acronyms

ADCP	Acoustic Doppler Current Profiler.
BC	Boundary Conditions.
COAWST	Coupled Ocean–Atmosphere–Wave–Sediment Transport.
ECMWF	European Centre for Medium-Range Weather Forecasts.
GEBCO	General Bathymetric Chart of the Ocean.
GFS	Global Forecast System.
HF	High Frequency.
IBI-MFC	Iberian Biscay Irish - Monitoring and Forecasting Centre.
IC	Initial Conditions.
NES	North Ebro shelf.
MCT	Model Coupling Toolkit.
POLCOMS	Proudman Oceanographic Laboratory Coastal-Ocean Modeling System.
RANS	Reynolds-Averaged Navier-Stokes.
RC	Range Cell.
ROMS	Regional Ocean Modeling System.
SBL	Surface Boundary Layer.
SMC	Servei Meteorològic de Catalunya.
SML	Surface Mixed Layer.
SWAN	Simulating Waves Nearshore.
TKE	Turbulent Kinetic Energy.
VF	Vortex Force.
WCI	Wave–Current Interactions.
WEC	Wave Effects on Currents.
WRF	Weather Research and Forecasting.

Parameters

d	skill score.
DSPR	Directional Spreading.
Dir	wave mean direction.
Hs	significant wave height.
MAE	Mean Absolute Error.
RMSD	Root Mean Square Deviation.
ssh	sea surface height.
Tp	wave peak period.
$\mathbf{Tm_{02}}$	wave mean period.
r	Pearson's correlation.
u, **v**	water current velocity components.

"Our knowledge is a little island in a great ocean of nonknowledge."

Isaac Bashevis Singer

Chapter I

Introduction

"Land is the secure ground of home, the sea is like life, the outside, the unknown."

Stephen Gardiner

1 Motivation

The coastal zone has always been a place where humans have developed many different activities. As a matter of fact, almost half the population of the European Union live within 50 km of the sea, and most of the large cities are on the coast (Suárez and Rodríguez, 2007). Specifically in Catalonia, the area comprised between the coastline and 500 m inland represents a 7% of the Catalan territory but it concentrates almost half of the population (PDUSC, 2004). The population concentration at the coastal regions, makes these areas very important from an economical and social point of view. Many different activities are carried out near the coast and thus there is a wide range of infrastructures (e.g. factories, seafronts, railroads, tracks, beaches, buildings, fisheries, etc.). During most of the year, the Catalan coast present a gentle sea state that promote a security sense and which favors the tourist claim. However, sometimes there are severe storm events that cause significant damages. For instance, during the last 20 years, storm surges have been responsible of at least 50 victims and many infrastructure damages throughout the Catalan coast. Figure 1.1 shows the spatial distribution of the overall damage integrated during the period 1910-2008. The values correspond to damage reported for all beaches within the coastal region.

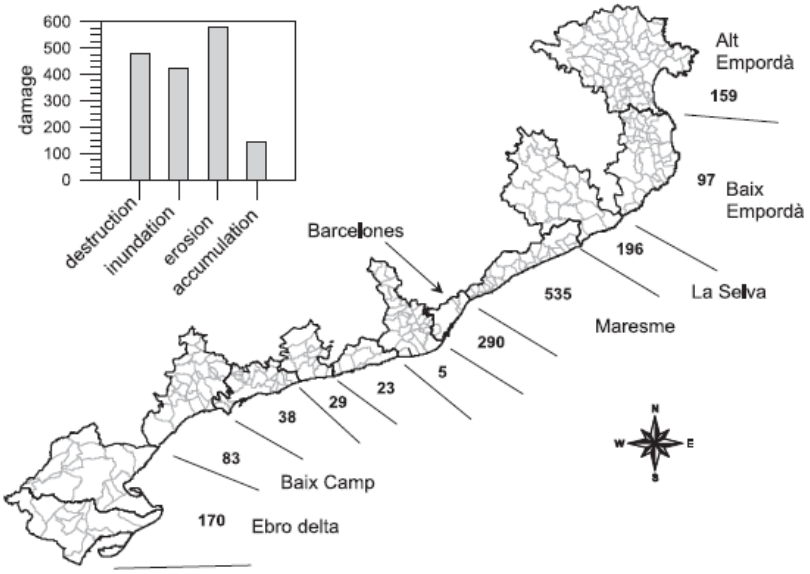

Figure 1.1: Time- and spatially-integrated damage along the Catalan coast during the period 1910-2008. Bar chart presents the contribution of each type of damage to the overall value. (Source: Jimenez et al., 2012)

With all this in mind, in this work the hydrodynamics at the Catalan coast are studied with the aim of understanding its dynamics and implementing a forecasting system in order to be able to predict quite accurately the sea conditions and prevent future damages.

In oceanographic terms, the study is focused at the continental shelf (see Figure 1.2). The continental shelf is the extension of a continent landmass under the ocean and extends from the coastline up

to an edge where the slope increases sharply, the shelf break, which is usually at 100–200 m depth. The sea floor below this break is called the continental slope, which is a much steeper zone. Below the continental slope is the continental rise, another sloping area that merges into the deep ocean floor, the abyssal plain. The continental shelf area is commonly subdivided in three dynamically different regions: the inner shelf, mid-shelf and outer shelf. Thus, the inner shelf is a transition zone from surf zone (where waves break) to mid-shelf (where theoretical Ekman transport occurs) that extends water depths up to tens of meters.

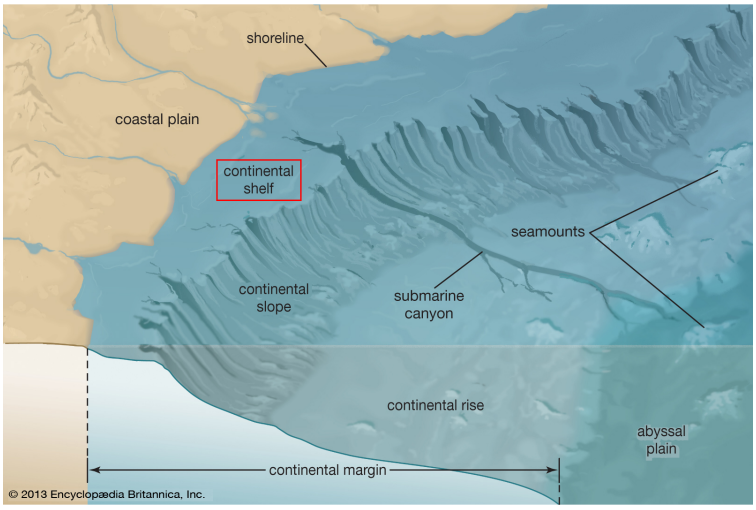

Figure 1.2: Continental margin (source: Encyclopædia Britannica Online; `https://www.britannica.com/media/full/134970/147308`).

Although the study area of this investigation is the Catalan shelf, the main scientific research will be carried out in a local wind-jet zone at the Southwest (SW) of the Catalan shelf, the Ebro Delta. Specifically, the Sant Jordi Bay, which is part of the North Ebro Shelf (NES). The NES is an appropriate location to investigate meteo-oceanographic conditions at coastal scales because it is a wind-jet zone, there is a relatively high amount of data for validation purposes and there are operational products where the model can be nested. The fact that it is a wind-jet zone makes it an interesting study area because the variable wind conditions that entail wind jets can influence the wind-wave generation and modify the ocean circulation patterns. Besides, during stratified periods (summer), cross-shelf winds result in an upwelling region that decisively influences the exchange of water mass and material along the shelf.

2 Study area

The Catalan coast is located in the Balearic Sea (Northwest Mediterranean) between latitudes 40°45' – 42°25' N and longitudes 0°45' – 3°15' E (see Figure 1.3) and the Ebro Delta region is the most southern part of it (40.4° – 41° N and 0.4° – 1.2° E). The aim of the below sections is to describe the main meteo-oceanic conditions of the study area.

Figure 1.3: The Mediterranean sea and, in white, the Balearic Sea [map data from Google Earth: SIO, NOAA, U.S. Navy, NGA, GEBCO, Image Landsat / Copernicus].

2.1 The Catalan coast

The Catalan coast, along its approximately 600 km long coastline, comprises a large variety of coastal types such as cliffs, deltas, embayed beaches, bays and long straight beaches. The bathymetry of the Catalan coast (see Figure 1.4), goes from a narrow continental shelf (at the North) to a wider continental shelf (at the South), which is an important feature for the hydrodynamic properties of the Catalan coast. The most important river is the Ebro river, with a length of 910 km and a basin area of 85.362 km^2.

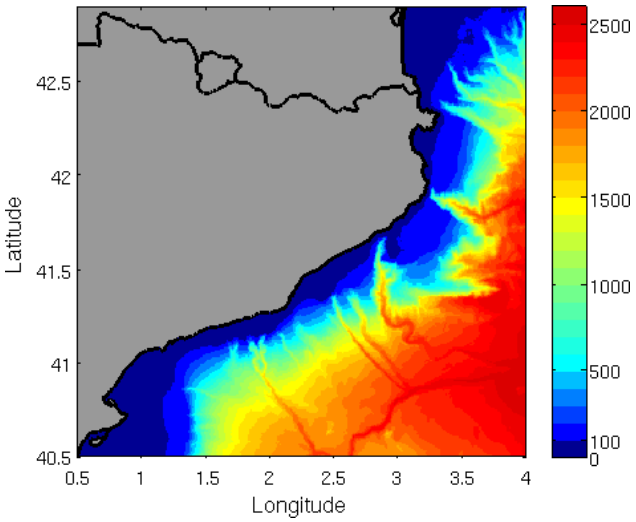

Figure 1.4: Catalan coast bathymetry.

2.1.1 Weather conditions

The complex orography and the location of the Catalan territory between the tropical and the polar air masses and between two seas makes Catalonia a place with a complex and variant weather. Catalonia is located in the temperate zone of the northern hemisphere and presents a Mediterranean climate with relatively high averaged temperatures, which go from 0° C at the Pyrenees to 17° C at the coast. The higher annual temperature range is found at the interior plains, with a variation between 18–21° C, and at the coastal zone, with an oscillation between 13–15° C (ICGC, 2010). The sea plays a very important role in the distribution of the temperature, since it acts as a thermal regulator. In general, two large air masses can be distinguished: the maritime tropical, characterized by an anticyclone from Africa with dry and hot wind (during summer), and the maritime polar, a dry and cool air mass from the northern Atlantic (during winter).

There is an irregular rainfall pattern, both in time and space, in the Catalan territory due to the relief configuration. On the one hand, at high mountain areas, values above 1.200 mm can be found, while at the western plains, there are values below 300 mm. On the other hand, the annual rainfall is not very high, but there are downpours where the precipitation can reach one quarter of the total annual precipitation. The Catalan coast is located inside the so called “dry Catalonia”, which means that the precipitation is less than 700 mm. At the coast, the season with more rain is the fall, especially the months of September and October, and the months with less rain are July, January and February.

The complex orography of the Catalan territory plays a very important role in the modification of the wind patterns. The predominant winds come from the northwest (NW; Mistral) and from the north (N; Tramontane) during December and January. Southerly and easterly winds are also important during February, March, April and November. In fall season the dominant wind is the Tramontane and is associated with the strongest mean velocities. Winter is characterized by the highest percentage (50%) of NW winds of the year but eastern wind conditions are also characteristic. In summer there is a dominance of southwesterly winds but the maximum wind speed corresponds to northwesterly winds. Mistral and Tramontane winds are developed due to the physical barrier that represent the Pyrenees. The influence of these winds can be noticed hundreds of kilometers offshore, carrying cold and dry air over the Mediterranean Sea (Bolaños et al., 2009).

2.1.2 Waves

The Catalan coast has some special features that determine the wave climate (Sánchez-Arcilla et al., 2008): complex bathymetry, high wind field variability in time and space, wave calms during the summer and energetic events from October to May, wave storms duration of less than 24 h, shadow effect for waves from south and east and short fetches (the maximum fetch, the length of water over which a given wind has blown, is about 600 km from the east). In spite of its limited fetch, the NW Mediterranean is able to generate harmful storms. The prediction of such storms near the coast is a tough challenge for operational oceanography due to the wind interaction with local topography, the sharply varying fields, the resulting sea-swell interaction and the influence of the land-sea border (Bolaños et al., 2009).

Some studies of wave climate have been done to determine the main wave features in the zone. In Figure 1.5 the directional wave distribution at four buoys distributed along the Catalan coast is shown. It can be observed that at the *Cap Tortosa* buoy (the southern-most position) there is a predominance of eastern wave conditions with also an important contribution of north-western waves. At *Llobregat* and *Tordera* buoys (i.e. at the central region), eastern and southern wave conditions dominate and, at the *Begur* buoy (which is the northern-most position), the main component is the north one.

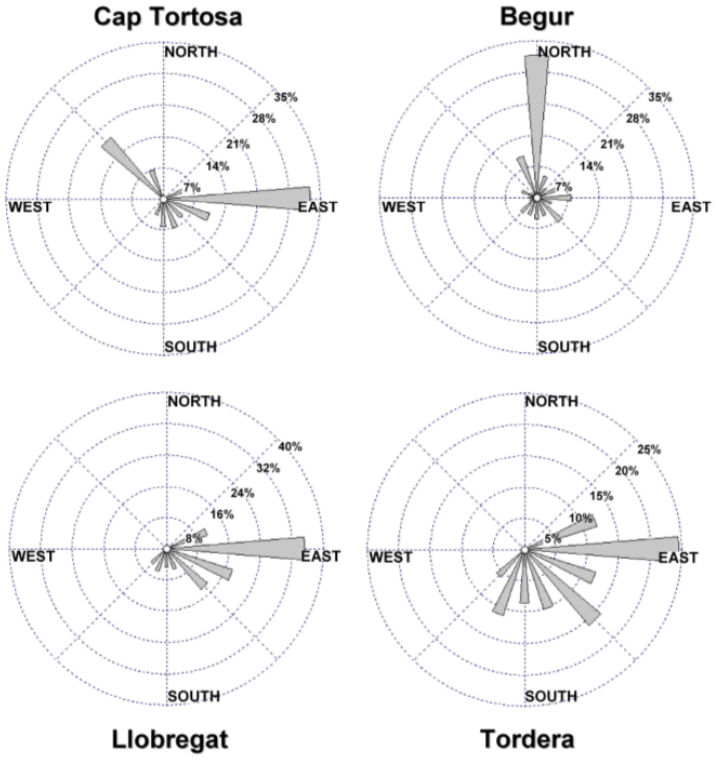

Figure 1.5: Directional wave distributions along the Catalan coast. The radial axis indicates frequencies of occurrence. (Source: Sánchez-Arcilla et al., 2008)

2.1.3 Sea level

The Mediterranean Sea is a microtidal environment where the astronomical tide is very small and the sea level variation is not as important as in other seas. The high frequency oscillations (with periods between hours and weeks) are mainly due to the astronomical tide and the meteorological induced effects (storm surges). For low frequency oscillations (seasonal frequencies) the main term is the steric effect, i.e. the changes of the sea level due to the volumetric change in the water column, which is a result of the changes in the water temperature.

The low pressures in the Mediterranean induce easterly fluxes that generate strong winds and high waves. The combination of all these, produces a significant rise of the sea level. High pressure areas are also common during summer and some weeks of January and February and, combined with the steric effect, produce an important variation of the sea level (Bolaños et al., 2009).

2.1.4 Ocean currents

The circulation in the NW Mediterranean Sea has been a study subject for many years. Ovchinnikov (1966) evaluated the general circulation in the Mediterranean and found a well-defined cyclonic structure that covered all the Balearic Sea. However, the computed current paths are not reliable in every area, since the study was based on mean seasonal temperature and salinity values. Now it is known that, in some areas, mesoscale phenomena are of major importance (Millot, 1987; Font et al., 1988). The modifications of the main circulation pattern have been studied by Tintoré et al. (1990); La Violette et al. (1990); Masó and Tintoré (1991); García et al. (1998); Pascual et al. (2002), among others.

In Figure 1.6 the main circulation patterns at the Western Mediterranean are presented. The predominant current in the Balearic Sea is the quasi-permanent current known as the Northern Current, which is an entity flowing south-westward along the continental slope (Millot, 1999) that can be modified by mesoscale events such as current meandering or eddies (Font et al., 1995). Using three current meters, Font et al. (1995) studied the current behavior and found that the general flow is along-slope, with a marked barotropic character, and presents occasional disruptions for periods of several days (mesoscale events). They also found that this mesoscale activity is strongly increased in autumn, followed by a rapid decrease in winter and then by a continuous decline until the end of the summer.

In winter, the Northern Current becomes deeper and narrower, flowing closer to the slope and developing relatively intense mesoscale meanders (Millot, 1999; Flexas et al., 2002). The mean

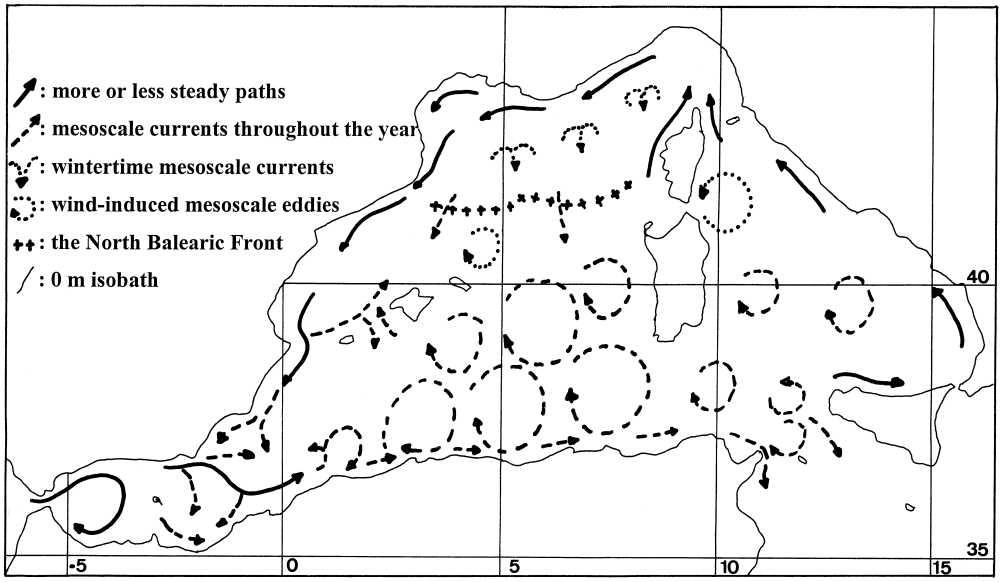

Figure 1.6: Western Mediterranean circulation in the upper layer (from Millot (1999)).

current intensity is not very strong (∼10 cm/s at 100 m depth) but it shows a seasonal intensification in winter when velocities can reach higher values (∼40 cm/s at 100 m depth) (Bolaños et al., 2009). The wind effects are restricted to the surface mixed layer (SML) and have little effect on the slope current.

2.2 The Ebro Delta

The Ebro Delta, with 320 km^2, is one of the largest wetland areas in the western Mediterranean region. It is characterized by the transition from a narrow shelf (∼10 km) at its northern end to a broader shelf (∼60 km) towards the south. The shelf break is at approximately 160 m water depth.

2.2.1 Weather conditions

At the Ebro Delta the local topography (see Figure 1.7c), with the coastal mountain chain breached by the Ebro river valley, exerts a significant control on wind climate (Bolaños et al., 2009). The most characteristic wind of the zone is the Mistral, which is channeled through the Ebro valley induced by the lee of the Pyrenees, resulting in an intensified wind when it reaches the sea, i.e. a "wind jet". This wind-jet is dry, cold, perpendicular to the coastline (cross-shelf wind jet) and associated with high wind intensities. Figure 1.7b shows an example of a NW wind-jet event. An intensification of the mean conditions is observed at the northern margin of the Ebro Delta, delimiting the wind-jet area.

The synoptic situation that causes these wind-jets is related with a high-pressure area over the

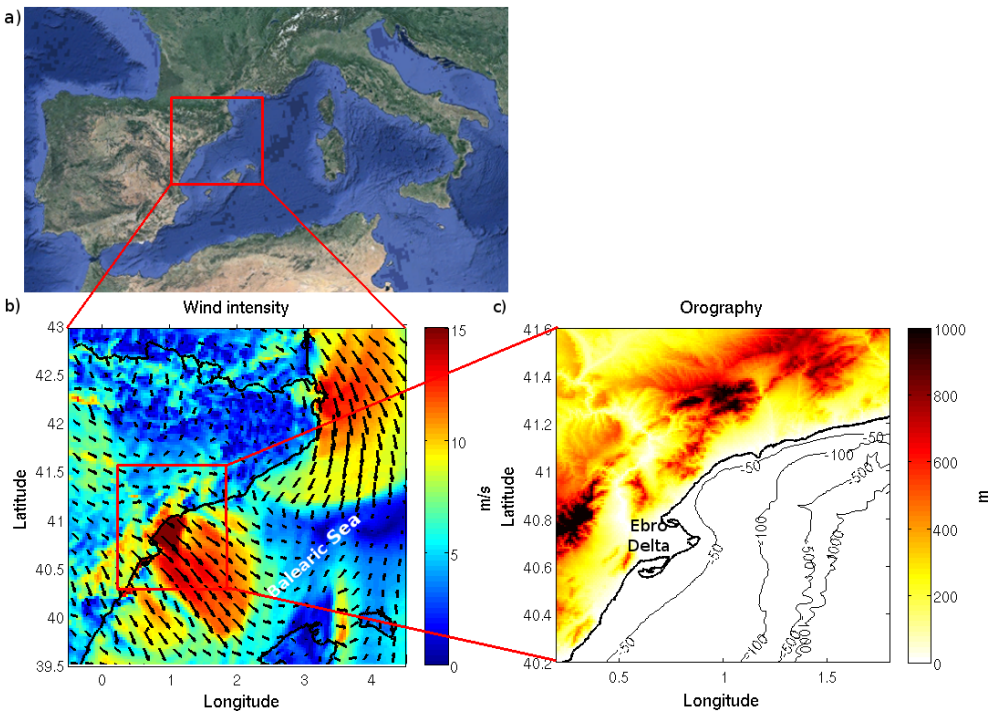

Figure 1.7: a) NW Mediterranean Sea [map data from Google, TerraMetrics]. b) Example of a NW wind-jet event. c) Ebro Delta orography and isobaths.

Bay of Biscay and a low-pressure area in the western Mediterranean Sea (Riosalido et al., 1986). An example of this synoptic situation can be seen in Figure 1.8. The wind jets are more usual and intense during autumn and winter, when larger atmospheric pressure gradient take place but a small pressure difference along the Ebro valley is enough to initiate wind at any season (Riosalido et al., 1986). Grifoll et al. (2015) analyzed the percentage of time that a NW wind blows for each month and found that during winter this percentage reaches 80 %, decreasing significantly during summer (with less than 20 %).

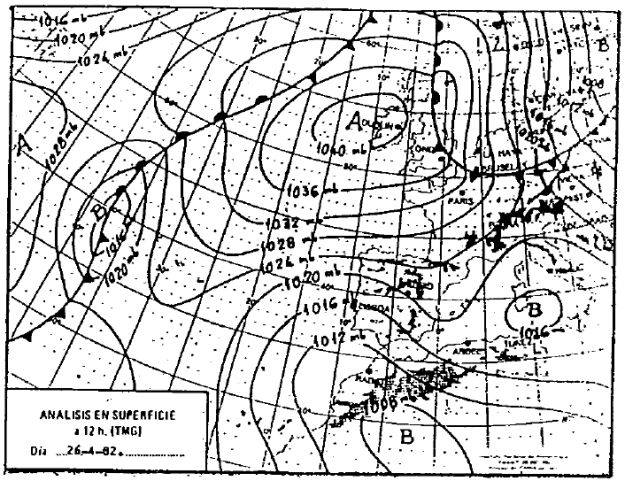

Figure 1.8: Surface analysis for 12 UTC on 26 April 1982. Synoptic situation where a pressure gradient is established in the Ebro valley from NW to SE. Source: Riosalido et al. (1986).

2.2.2 Waves

The Ebro Delta wave climate is characterized by a predominance of NW conditions (which coincides with the predominance of NW winds) with also significant east and south storms. These storms tend to develop a bimodal directional spectrum due to the coexistence of sea and swell waves (Sánchez-Arcilla et al., 2008). An example of a typical bimodal wave spectra at the Ebro Delta is shown in Figure 1.9. Bolaños et al. (2009) found that, during the eastern and southern storms, swell dominates (60%), while for NW storms (offshore winds), the sea system dominated (96%). Although there are more deltas along the Catalan coast, the Ebro Delta is the one that shows a greater presence of bimodal wave spectra.

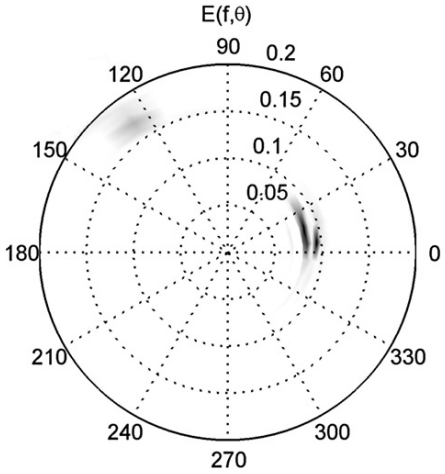

Figure 1.9: Typical bimodal wave spectrum at the Ebro delta. The plot shows the swell component from E and the sea component from NW. Source: Bolaños et al. (2009).

2.2.3 Ocean currents

The widening of the continental shelf at the Ebro Delta produces a gyre of almost 90° in the direction of the isobaths, becoming a barrier to the SW circulation of the Northern Current, which is deviated to the south. Some studies have examined the likely presence of an anticyclonic circulation pattern controlled by the bathymetry in the zone (Font, 1986; Espino et al., 1998). Using 1-year water velocity observations measured at 43.5 m, Grifoll et al. (2015) showed that the mean flow was polarized following the isobaths at the shelf region, but significant seaward near-surface velocities occurred predominantly during offshore wind events.

The river discharge off the Ebro Delta may have a relevant influence in the circulation pattern of the area. The freshwater enters the sea flowing to the NE but is deviated by the SW circulation to the E and then to the S, due to the Coriolis force (Durand et al., 2002). This mesoscale event

of confrontation of flows with different salinity (and therefore different density) can produce an anticyclonic circulation (Font, 1986). Nevertheless, Durand et al. (2002) and Mestres et al. (2003), showed that the effects of the river plume on the circulation are only important near the river mouth (∼10 km offshore).

3 Objectives and outline of the thesis

The main objective of this research is to use numerical models to investigate the ocean dynamics at a wind-jet region of the Catalan coast, the north Ebro Shelf (NES), with the final aim of implementing an operational forecasting system for the whole Catalan coast.

The above objective can be divided into four partial objectives, which are supposed to be more specific and focused on an specific aspect of the main objective.

1. **Study the local circulation induced by a wind jet**.
2. **Study the effect of wind jets on waves**.
3. **Study the wave–current interactions under wind-jet conditions**.
4. **Implement an operational system**.

This thesis has been organized following the objectives exposed above. The overall structure is as follows:

- **Chapter I. Introduction**
  The aim of the present chapter is to introduce the reader with the research motivation and objectives, as well as presenting the main characteristics of the study area and showing the thesis structure.
- **Chapter II. Methodology**
  This chapter has an explanation of the numerical models, data and methods used throughout this study.
- **Chapter III. Circulation induced by a wind jet**
  This chapter deals with **objective 1**: *study the local circulation induced by a wind jet.* For this purpose, the ROMS oceanic model has been implemented and calibrated at the NES study domain. The model has been validated with in-situ buoy measurements and high frequency (HF) radar data. The study include an analysis of the momentum balance and the vertical structure of the water column.
- **Chapter IV. Wave dynamics induced by a wind jet**
  This chapter deals with **objective 2**: *study the effect of wind jets on waves.* With this aim, the SWAN wave model has been implemented and calibrated at the NES study domain. The model has been validated with in-situ buoy measurements and HF radar data. The study

include analysis of bimodal spectra and directional spreading as well as an investigation of the reliability of the HF radar wave data.

- **Chapter V. Wave–current interactions under wind-jet conditions**
  This chapter deals with **objective 3**: *study the wave–current interactions under wind-jet conditions*. For this end, the ROMS and SWAN models have been coupled at the same NES domain and study period as in the previous two chapters. The coupled system has been validated with in-situ buoy measurements and HF radar data. The study has been based on the comparison between coupled and uncoupled models.

- **Chapter VI. Implementation of an operational forecasting system**
  This chapter deals with **objective 4**: *implement an operational system*. With this objective, the numerical model configurations used to investigate the waves and currents at the NES region has been extrapolated to the whole Catalan coast and an operational forecasting system has been implemented. The system has been validated using in-situ measurements, HF radar data and satellite data.

- **Chapter VII. Final discussion and main conclusions**
  This chapter includes a general discussion and the main conclusions.

The work presented in Chapters III, IV and V have been structured as scientific articles, since most of them have already been published. Besides, this allows a separate reading of each chapter.

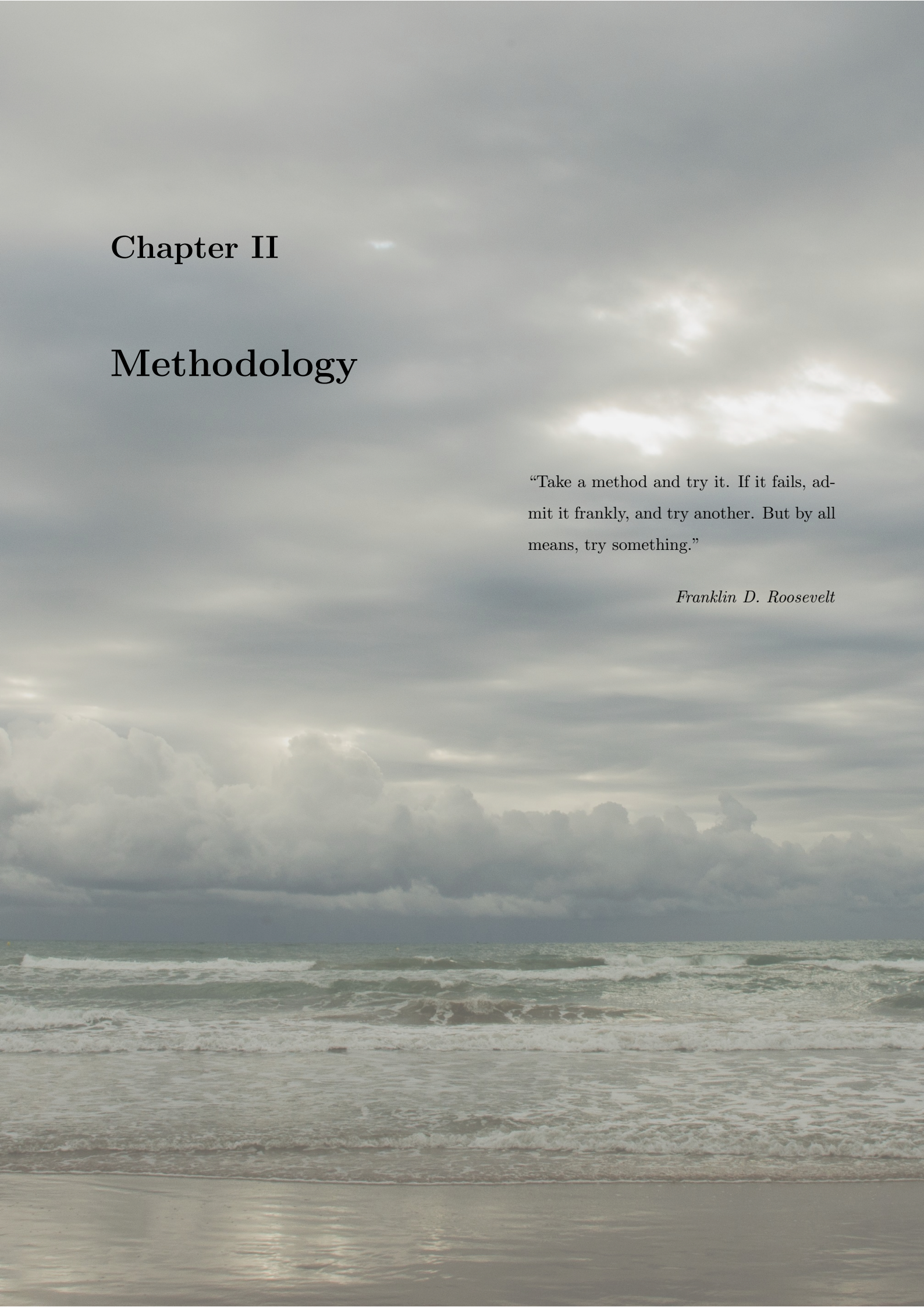

Chapter II

Methodology

"Take a method and try it. If it fails, admit it frankly, and try another. But by all means, try something."

Franklin D. Roosevelt

1 Numerical models

The numerical models used in this study are the ROMS model for the ocean dynamics and the SWAN model for the waves. In order to couple these two models, the COAWST Modeling System is used. Each of these models is described in the following sections.

1.1 ROMS

The Regional Ocean Modeling System (ROMS) is a split-explicit, free-surface, terrain-following, primitive equations oceanic model that solves the 3D Reynolds-Averaged Navier-Stokes (RANS) equations using the hydrostatic and Boussinesq assumptions (Shchepetkin and McWilliams, 2005; Haidvogel et al., 2008). The model uses finite-difference approximations on a terrain-following vertical coordinate (sigma-coordinate) and on a horizontal curvilinear Arakawa C grid.

The governing equations in Cartesian coordinates are:

$$\frac{\partial u}{\partial t} + \overrightarrow{v} \cdot \nabla u - fv = -\frac{\partial \phi}{\partial x} - \frac{\partial}{\partial z}\left(\overline{u'w'} - \nu \frac{\partial u}{\partial z}\right) + F_u + D_u \tag{2.1}$$

$$\frac{\partial v}{\partial t} + \overrightarrow{v} \cdot \nabla v - fu = -\frac{\partial \phi}{\partial y} - \frac{\partial}{\partial z}\left(\overline{v'w'} - \nu \frac{\partial v}{\partial z}\right) + F_v + D_v \tag{2.2}$$

$$\frac{\partial \phi}{\partial z} = \frac{-\rho g}{\rho_0} \tag{2.3}$$

with the continuity equation

$$\frac{\partial u}{\partial x} + \frac{\partial v}{\partial y} + \frac{\partial w}{\partial z} = 0 \tag{2.4}$$

the scalar transport

$$\frac{\partial C}{\partial t} + \overrightarrow{v} \cdot \nabla C = -\frac{\partial}{\partial z}\left(\overline{C'w'} - \nu_\theta \frac{\partial C}{\partial z}\right) + F_C + D_C \tag{2.5}$$

and equation of state

$$\rho = \rho\left(T, S, P\right) \tag{2.6}$$

where F_u and D_u are the effects of forcing and horizontal dissipation, respectively. Equations (2.1) and (2.2) express the momentum balance in the x- and y-directions. Note that in these equations density variations are neglected due to the Boussinesq approximation. The only contribution of density is to the buoyancy force in the vertical momentum equation (2.3). Under the hydrostatic approximation, it is further assumed that the vertical pressure gradient balances the buoyancy force. The continuity equation for an incompressible fluid is given by equation (2.4). The time evolution of all scalar concentration fields, including those for $T(x, y, z, t)$ and $S(x, y, z, t)$, are governed by the advective-diffusive equation (2.5). Lastly, equation (2.6) expresses the equation of state.

1.2 SWAN

The Simulating Waves Nearshore (SWAN) model is a third-generation numerical wave model which computes random, short-crested waves in coastal regions with shallow water and ambient currents (Booij et al., 1999).

Usually, wave models work with the energy balance equation in terms of energy density E but, since SWAN accounts for wave-current interactions, it is based on the action balance equation in terms of action density N (Bretherton and Garrett, 1968). Notice that $N(\sigma, \theta) = E(\sigma, \theta)/\sigma$ (where σ is the relative frequency and θ is the propagation direction) and that N is conserved during propagation in presence of ambient current, whereas E is not. The evolution of the action density N is governed by the action balance equation, which is resolved by means of implicit schemes and which, expressed in Cartesian coordinates, is:

$$\frac{\partial N}{\partial t} + \frac{\partial c_x N}{\partial x} + \frac{\partial c_y N}{\partial y} + \frac{\partial c_\sigma N}{\partial \sigma} + \frac{\partial c_\theta N}{\partial \theta} = \frac{S_{tot}}{\sigma} \tag{2.7}$$

with $N(x, y, t, \sigma, \theta)$. The first term of the left-hand side of the equation accounts for the kinematics of the energy balance, the second and third one denote the wave energy propagation in the spherical space (with c_x and c_y propagation velocities), the fourth term represents the effect of shifting of the radian frequency due to variations in depth and mean currents and the last term accounts for the wave refraction due to depth and current. In the right-hand side, S_{tot} describes the terms of energy source and sink. In shallow water, there are six processes that contribute to S_{tot}:

$$S_{tot} = S_{in} + S_{nl3} + S_{nl4} + S_{ds,w} + S_{ds,b} + S_{ds,br} \tag{2.8}$$

The right-hand side terms denote, form left to right, wave growth due to wind, nonlinear transfer

of wave energy through three-wave and four-wave interactions and wave energy dissipation due to whitecapping, bottom friction and depth-induced wave breaking.

1.3 COAWST Modeling System

The Coupled Ocean-Atmosphere-Wave-Sediment Transport (COAWST) Modeling System (Warner et al., 2010) is an agglomeration of open-source modeling components that has been tailored to investigate coastal processes of the atmosphere, ocean, waves and coastal environment. COAWST incorporates a three-dimensional hydrostatic ocean model (ROMS), a wave generation and propagation model (SWAN), a non-hydrostatic meteorological model (WRF; Weather Research and Forecasting) and a coupler (MCT; Model Coupling Toolkit).

In this study, the COAWST is used to couple the ROMS model with the SWAN model by means of the MCT (Larson et al., 2004; Jacob et al., 2004), which is is a Fortran90 program that works with the MPI protocol. It allows the transmission and transformation of various distributed data between component models using a parallel coupled approach. When the models are initialized, each model decomposes its own domain into different sections, which are distributed to processors. On each processor, each grid section initializes into MCT and a global map of the distribution of the segments is computed. Each segment also initializes an attribute vector that contains the fields to be exchanged and establishes a router to provide an exchange pathway between model components. While the simulation is run, the models reach a synchronization point, fill the attribute vectors with data and exchange fields. Further details are described in Warner et al. (2008a).

2 Data

In this section, the data used throughout the study is presented. First the data used to run the models is exposed, which is the WRF model data and the IBI-MFC model data. Then, the data used to validate the models is introduced, which includes in-situ measurements, High Frequency (HF) radar measurements and Satellite data.

2.1 WRF model data

In this work, the ROMS and SWAN model are forced with atmospheric data from a previous WRF model run provided by the Meteorological Service of Catalonia (SMC).

The WRF model is a numerical weather prediction system designed for research and operational forecasting applications. The dynamic solver used in the WRF model implemented at the SMC is the Advanced Research WRF (ARW; Skamarock et al., 2008) core, developed primarily at the NCAR (National Center for Atmospheric Research, EUA). This core integrates the fully compressible, nonhydrostatic Euler equations formulated using a terrain-following hydrostatic-pressure vertical coordinate. It includes boundary layer physics schemes and a variety of physical parametrization of sub-grid scale processes for predicting meso- and micro-scales of motion.

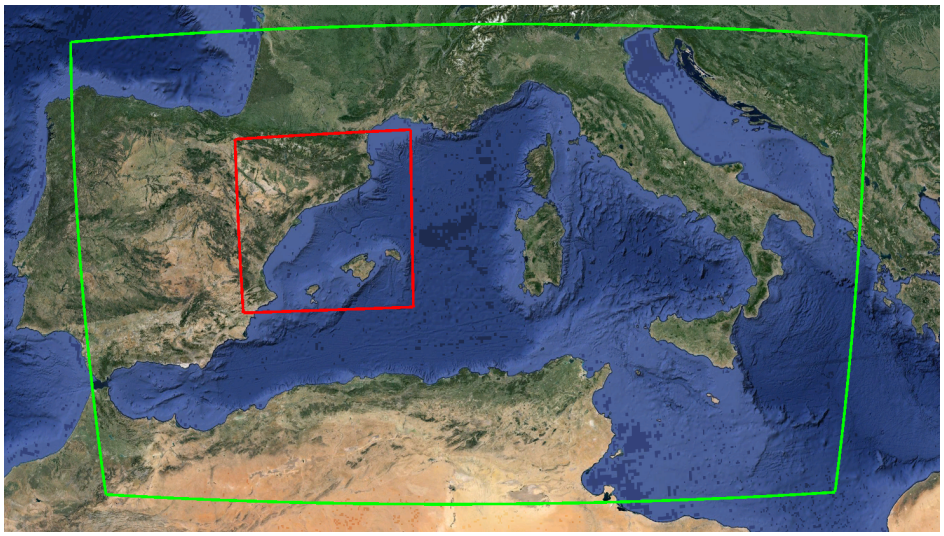

Figure 2.1: Numerical domains of the WRF model implemented at the SMC. In green, the WRF15 domain and, in red, the WRF3 domain.

The WRF model implementation at the SMC is based in a downscaling technique. A first level domain (named WRF15) attempts to provide meteorological data at an intermediate scale of 15 km grid length. In this case, the model is run using data from the Global Forecast System (GFS) as initial and boundary conditions. The GFS is a weather forecast model produced by the National

Centers for Environmental Prediction (NCEP), which meteorological outputs are available for free in the public domain under provisions of U.S. law. Then, a second level domain (named WRF3) is nested to the WRF15 one in order to obtain meteorological data at higher resolution (3 km). The numerical domains are presented in Figure 2.1 and the technical details of each model domain configuration is shown in Table 2.1.

Table 2.1: Technical details of the WRF model implementation at the SMC. Number of cells and vertical levels (X×Y×Z), grid resolutions (Grid), lead time (Time), boundary conditions actualization (BC), data output (DT), use of nudging (Nudging) and nesting type (Nesting).

	X×Y×Z	Grid	Time	BC	DT	Nudging	Nesting
WRF15	176×106×31	15 km	172 h	6 h	1 h	Yes	-
WRF3	191×191×31	3 km	72h	1 h	1 h	No	1-way

2.2 IBI-MFC model data

As initial and boundary conditions for the ROMS model, data from the IBI-MFC (Iberian Biscay Irish - Monitoring and Forecasting Centre) forecast product are used.

This product (IBI_ANALYSIS_FORECAST_PHYS_005_001; `http://marine.copernicus.eu/`) is based on a (eddy-resolving) NEMO model application run at 0.028° horizontal resolution and provides a 5-day hydrodynamic forecast. The IBI-MFC forecasting run is forced every 3 hours with atmospheric fields provided by ECMWF (European Centre for Medium-Range Weather Forecasts), has a vertical coverage up to -5,500 m and the numerical domain spans between longitudes -19° and 5° and between latitudes 26° and 56°.

The IBI-MFC product data is available since 1st January 2013 and is daily generated by Puertos del Estado (Nominal IBI System) and Mercator-Ocean (as Back-up System) and include 3D daily means fields of temperature, salinity, sea surface height, zonal velocity and meridional velocity, as well as hourly means of surface fields (sea surface height and surface temperature and currents).

2.3 In-situ measurements

In order to validate the numerical model results, oceanographic and coastal meteorological measurements from the Spanish Harbor Agency (Puertos del Estado, `http://www.puertos.es`) are used. Along the Catalan coast there are two coastal wave buoys (Tarragona Coast and Barcelona Coast), two deep water buoys (Tarragona and Begur) and two tide gauges (Tarragona TG and Barcelona

Table 2.2: Summary of the buoys from the Puertos del Estado network at the Balearic Sea.

Buoy	Location	Depth	Start date	Available data
Tarragona	1.47° E 40.68° N	688 m	August 2004	wave spectra, wind velocity and direction, water current speed and direction, water temperature and water salinity
Begur	3.65° E 41.92° N	1200 m	March 2001	wave spectra and wind velocity and direction
Dragonera	2.10° E 39.56° N	135 m	November 2006	wave spectra, water current speed and direction and water temperature
Maó	4.42° E 39.72° N	300 m	April 1993	wave spectra and wind velocity and direction
Valencia	0.21° E 39.52° N	260 m	September 2005	wave spectra, water current speed and direction, water temperature and water salinity
Tarragona Coast	1.19° E 41.07° N	15 m	November 1992	wave statistics and spectra and water temperature
Barcelona Coast	2.20° E 41.32° N	68 m	March 2004	wave statistics and spectra and water temperature
Tarragona TG	1.21° E 41.08° N	-	May 2011	sea level and wind velocity and direction
Barcelona TG	2.17° E 41.34° N	-	January 1993	sea level and wind velocity and direction

TG). Out of the Catalan coast, extending to the Balearic Sea, there are three deep buoys more (Mahón, Dragonera and Valencia). See table 2.2 for more detailed information.

Since the wind measured by the buoys is at 3 m heigh and the numerical models output wind is at 10 m heigh, in order to be able to compare both data, the modeled data have been extrapolated from 10 m to 3 m using the logarithmic profile

$$U_z = \frac{U^*}{\kappa} \ln\left(\frac{z}{z_0}\right) \tag{2.9}$$

where U_z is the mean horizontal wind velocity at a given height z, U^* is the frictional velocity, κ is the von Kármán constant ($\kappa \simeq 0.4$) and z_0 is the aerodynamic roughness length.

The roughness length is estimated by means of the Charnock's relation

$$z_0 = \frac{\alpha_{CH} U^{*2}}{g} \tag{2.10}$$

where g is the gravitational constant and α_{CH} is the Charnock parameter (in this study an α_{CH} equal to 0.011 has been considered).

The friction velocity is related to the known wind speed at 10 m elevation (U_{10}) with

$$U^{*2} = C_D U_{10}^2 \tag{2.11}$$

where C_D is the drag coefficient from Wu (1982)

$$C_D(U_{10}) = \begin{cases} 1.2875 \cdot 10^{-3}, & \text{for } U_{10} < 7.5 \text{ m/s} \\ (0.8 + 0.065 \cdot U_{10}) \cdot 10^{-3}, & \text{for } U_{10} \geq 7.5 \text{ m/s} \end{cases} \tag{2.12}$$

2.4 High Frequency radar

The High Frequency (HF) radar system used in this work is a CODAR SeaSonde standard-range system composed by three remote shelf-based sites (Salou, Alfacada and Vinaroz; see locations in Figure 2.2b). Each site comprises a transmitter-receiver antenna that operates at a nominal frequency of 13.5 MHz with a 90 KHz bandwidth. It became operational in December 2013 and both wave and water current data are available.

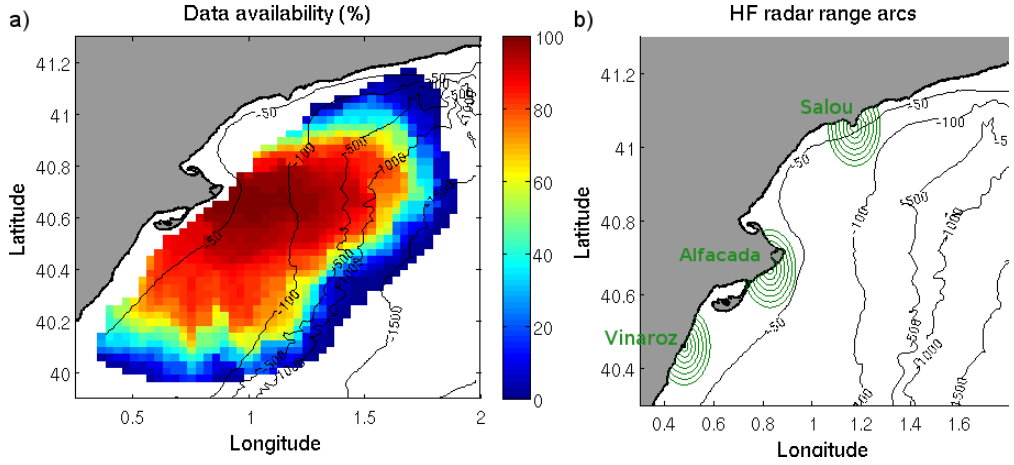

Figure 2.2: High Frequency radar a) water current data availability and b) wave data range arcs.

Regarding the water current data, the system provides hourly measurements of the current velocities

in the first upper meter of the water column with a horizontal resolution of 3 km and a cut-off filter of 100 cm/s. See Lorente et al. (2015) for further information about the system. HF radar measurements are subject to many potential errors (Graber and Haus, 1997). With the aim of minimizing them, an analysis of the data availability is carried out in order to reject low-confidence measuring points. Figure 2.2a shows that the central area of the radar domain has more than 80% data available, but near the boundary there are points with lower data availability (in some cases less than 10%). Following the criteria used by Lorente et al. (2015), only the HF radar points with more than 50% of data availability are used in the validation.

Regarding the wave data, each site provides measurements of wave height, central period and direction along seven concentric arcs (plotted in green in Figure 2.2b) every 30 minutes, with the most offshore arc situated 11.6 km from the antenna.

2.5 Satellite wave data

The Jason-3 (J3) and Sentinel-3A (S3A) altimeter missions data are used, which are available at the Copernicus catalogue (`http://marine.copernicus.eu/`). These are processed by the SL-TAC multimission altimeter data processing system. To produce the near real time Hs data, the system acquires altimeter data for each mission and then performs an editing process that consist in selecting the valid data using a combination of criteria and thresholds on parameter values. Finally, the Hs values form the S3A mission are calibrated on the reference mission, the J3 mission, which is calibrated with buoys data. The measurements are available since July 2017 and have a 7 km along-track resolution. For J3 the latitude limits are 66° S and 66° N and for S3A the coverage is between 80° S and 80° N.

In order to be able to compare satellite measurements (along tracks) with buoy measurements (fixed points) or numerical model results (2D mesh) the data need to be collocated in time and space. Regarding the time collocation, the satellite data is collocated to the nearest time step of the model/buoy data, which have an interval of 1 h. Thus, just the time steps where the difference between the two time stamps is less than 30 min are considered. And regarding the space collocation two methods are distinguished: one for point measurements and one for 2D meshes. In the 2D mesh cases, the meshed data is interpolated to the satellite data points. In contrast, in the point collocation cases, a collocation radius of 0.25° is used to collocate the satellite data to the desired point. If there are more than one measure that satisfy the collocation condition, then a mean value of all them is used. In Figure 2.3 an example of the spatial collocation at a buoy location is presented. In this case, the point collocation of satellite data would be the mean value of the green

points, which are inside the collocation radius.

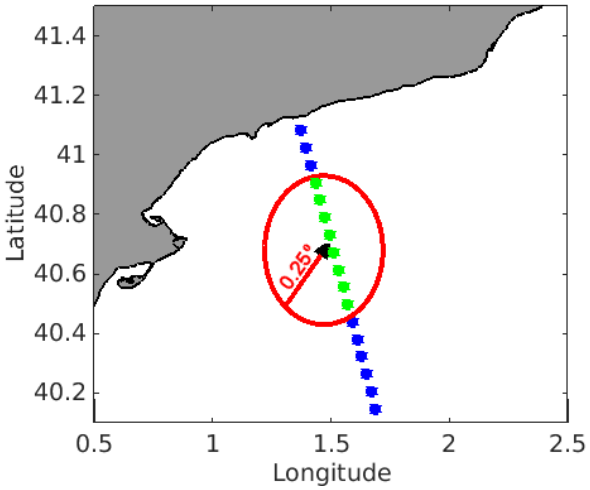

Figure 2.3: Example of satellite data collocation method. The black triangle is the buoy location, the red circle the collocation radius and the blue and green points the satellite data (being the green points the ones that are inside the collocation radius).

Finally, in order to filter spurious data, satellite data points where the Hs difference with respect to the Hs of the corresponding successive along-track point are greater than 0.5 m have been omitted.

3 Skill assessment

In order to assess the model behavior, the estimation of the bias, the Mean Absolute Error (MAE), the Root Mean Square Deviation (RMSD), the Pearson's correlation (Pearson's r) and the model skill score (d, following the method presented in Willmott (1981)), are undertaken. These values are defined as follows:

$$bias = \frac{1}{N}\sum\left(X_{model} - X_{obs}\right) \tag{2.13}$$

$$MAE = \frac{1}{N}\sum\left|X_{model} - X_{obs}\right| \tag{2.14}$$

$$RMSD = \sqrt{\frac{1}{N}\sum\left(X_{model} - X_{obs}\right)^2} \tag{2.15}$$

$$r = \frac{\sum\left(\left(X_{model} - \overline{X_{model}}\right)\left(X_{obs} - \overline{X_{obs}}\right)\right)}{\sqrt{\sum\left(X_{model} - \overline{X_{model}}\right)^2}\sqrt{\sum\left(X_{obs} - \overline{X_{obs}}\right)^2}} \tag{2.16}$$

$$d = 1 - \frac{\sum\left|X_{model} - X_{obs}\right|^2}{\sum\left(\left|X_{model} - \overline{X_{obs}}\right| + \left|X_{obs} - \overline{X_{obs}}\right|\right)^2} \tag{2.17}$$

where N is the number of samples. Pearson's r describes consistent proportional increases or decreases about respective means of the two quantities, but it makes too few distinctions among the type or magnitudes of possible covariations (Willmott, 1981). By contrast, d is not a measure of correlation or association in the formal sense but rather a measure of the degree to which a model's predictions are error free. Unlike r, d is sensitive to differences between the observed and predicted means as well as to certain changes in proportionality (Willmott, 1981). Note that analogously to r, d is measured from 0 to 1, 1 denoting maximum agreement.

For circular data, e.g. wave direction, the metrics are computed as follows:

$$bias = \tan^{-1}\left(\frac{\frac{1}{N}\sum\sin\left(X_{model} - X_{obs}\right)}{\frac{1}{N}\sum\cos\left(X_{model} - X_{obs}\right)}\right) \tag{2.18}$$

$$RMSD = \sqrt{-2\cdot\ln\left(\frac{1}{N}\sum\cos\left(X_{obs} - X_{model}\right)\right)} \tag{2.19}$$

$$r = \frac{\sum \left(\sin\left(X_{model} - \overline{X_{model}}\right) \sin\left(X_{obs} - \overline{X_{obs}}\right)\right)}{\sqrt{\sum \sin^2\left(X_{model} - \overline{X_{model}}\right) \sum \sin^2\left(X_{obs} - \overline{X_{obs}}\right)}} \tag{2.20}$$

Chapter III

Circulation induced by a wind jet

"The more violent the storm, the quicker it passes."

Paulo Coelho

The content of this chapter has been published in:

Ràfols, L., Grifoll, M., Jordà, G., Espino, M., Sairouní, A. and Bravo, M. (2017). Shelf circulation induced by an orographic wind jet. *Journal of Geophysical Research: Oceans*, 122, doi: 10.1002/2017JC012773.

1 Introduction

Wind-driven shelf circulation investigations have focused their attention on the effects of along-shelf winds, which result in upwelling or downwelling. However, cross-shelf circulation due to cross-shelf winds is larger than cross-shelf circulation due to along-shelf winds of the same magnitude in water depths that are less than the surface boundary layer (SBL) thickness (Lentz and Fewings, 2012). In this region, cross-shelf winds can generate substantial cross-shelf transport and, therefore, upwelling and downwelling (Tilburg, 2003).

The continental shelf is constrained by the shoreline and the continental slope and can be divided in three dynamically different regions. Going from shallower to deeper waters, there is the inner shelf, the mid-shelf and the outer-shelf. Thus, the inner shelf is a transition zone (from surf zone to mid-shelf) that extends water depths up to tens of meters. Since the surf zone dynamics are dominated by breaking waves and the mid-shelf is usually in geostrophic balance, the inner shelf may have elements of both (Fewings and Lentz, 2010). In this sense, previous investigations (collected in Lentz and Fewings, 2012) have analyzed the cross-shelf circulation response due to cross-shelf winds and found two dynamical regions: onshore (inner shelf) and offshore (mid-shelf) of the location where the SBL intersects the bottom. Those studies also established that during cross-shelf winds, the cross-shelf circulation is confined to the SBL. Thus, in this work, since it is focused on the shelf circulation due to cross-shelf winds, the SBL is defined as the depth at which the cross-shelf circulation in the upper layer shuts off and the inner shelf is defined as the region onshore of where the SBL intersects the bottom (similarly to Tilburg (2003) and Horwitz and Lentz (2014) when analyzing the response to a cross-shelf wind stress).

Regions with coastal wind jets induced by orographic effects are areas with complex dynamics in terms of water circulation response (Jordà, 2005; Grifoll et al., 2015; Trasviña et al., 1995), spatial and temporal wind variability (Jiang et al., 2009) and sharp wave height variations (Shimada and Kawamura, 2006). In this sense, several researchers have focused on the description of different aspects such as the wave generation/decaying process (Shimada and Kawamura, 2006), the surface water cooling effect due to upwelling (Trasviña et al., 1995) or the influence of the sea surface roughness variation due to the wave climate (Grifoll et al., 2016a). However, these regions have still not been thoroughly investigated and some aspects of the water circulation response to wind jets remain unclear. Thus, regions where the circulation pattern may be rapidly modified under the presence of a wind jet deserve special attention. (Grifoll et al., 2015) performed an observational study and found a seasonal response of the water circulation due to cross-shelf winds. They also highlighted the presence of cold water at the surface and attempted to discern between an upwelling process and a cooling effect due to mixing. However, the common sparsity of their measurements

does not allow one to extrapolate their conclusions to the whole region since the shelf response to cross-shelf winds is highly dependent on water depth. Tilburg (2003) showed that at the inner shelf, cross-shelf winds can result in cross-shelf velocities in the top few meters of the water column that are similar in magnitude to those generated by along-shelf winds. In fact, the author found that cross-shelf winds can be the primary mechanism for cross-shelf transport within the friction-dominated inner shelf. Horwitz and Lentz (2014) noted that it is the cross-shelf rather than vertical density gradient that is critical to predict transport driven by a cross-shelf wind stress. To investigate these processes, the use of numerical modeling has been proven to be a powerful tool (e.g., Tilburg, 2003; Horwitz and Lentz, 2014; Grifoll et al., 2016a).

At the north Ebro Shelf (NES) in the NW Mediterranean Sea, when the wind approaches from the NW, channeled through the Ebro Valley, it results in an intensified wind upon reaching the sea, commonly known as an orographic wind jet. This wind is dry, cold, perpendicular to the coastline (cross-shelf wind) and associated with high wind intensities. The synoptic situation that causes this wind jet is related to a high-pressure area over the Bay of Biscay and a low-pressure area in the western Mediterranean Sea (Riosalido et al., 1986). The wind jet is more common and intense in autumn and winter, when a larger atmospheric pressure gradient exists, but a small pressure difference along the Ebro Valley is enough to initiate wind during any season (Riosalido et al., 1986). In addition, cross-shelf winds can have a significant contribution to cross-shelf transport of water and material on the continental shelf (Tilburg, 2003), with further implications to suspended matter and biological processes.

The main goal of this study is to describe the effects of a wind jet on the circulation and hydrographic properties of the continental shelf. To do that, a numerical model has been implemented in the NES and run for a period of 6 months (from 1 March to 1 September 2014). This period was selected due to the high availability of different types of observational data, which has allowed for the skill assessment of the numerical model results. The influence of the stratification at the initial stages of the wind jet episodes and the main mechanisms that govern the cross-shelf circulation during those episodes are investigated.

This chapter is organized as follows. Section 3 contains the results. First, the wind data are analyzed to locate and characterize the wind-jet events, then the numerical model is validated using data from an HF radar and finally a selected wind-jet episode is analyzed in detail, while a more general description is compiled for the remaining set of events. Section 4 contains a discussion, where the results are compared with previous studies focusing on the role of the stratification and the estimation of the momentum balance terms. Finally, the most relevant conclusions are summarized in Section 5.

2 Methodology

2.1 Numerical Model

The Regional Ocean Modeling System (ROMS) is used in this study. A high-resolution domain is implemented at the NES. It has 20 vertical sigma levels and a horizontal grid of 260 × 166 points with a resolution of 350 m in both directions that covers an area of 91 × 58.1 km (see Figure 3.1). The model implementation includes a Generic Length-Scale turbulent vertical mixing scheme with the $k - \epsilon$ parametrization, a logarithmic profile for the bottom boundary layer with a bottom roughness of 0.005 m and horizontal mixing terms in geopotential surfaces.

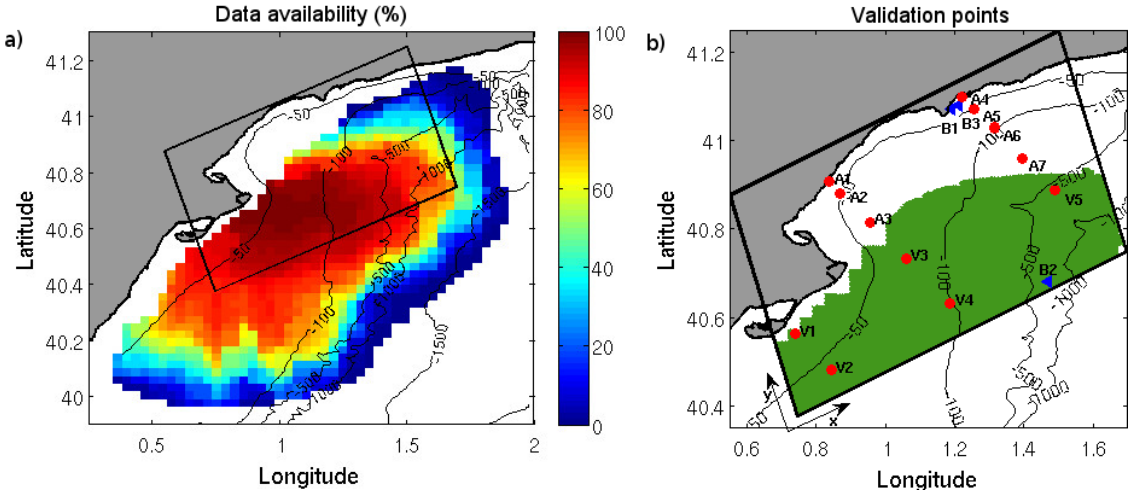

Figure 3.1: (a) HF radar data availability for the studied period. The black rectangle specifies the model domain. (b) Resultant validation area and validation points' locations. The black rectangle is the numerical model domain, the tide gauge (TG), the deep water buoy (DB) and the coastal wave buoy (CB) are represented with blue triangles. The red dots are the points chosen for validation and analysis in the results and discussion sections. The "V" points mark where the results can be validated with HF radar data. The green area shows where more than 50% of the HF radar data is available. The figure also includes the reference x/y axis used.

As initial and boundary conditions, data from IBI-MFC (Iberian Biscay Irish - Monitoring and Forecasting Centre) product are used. This product (`http://marine.copernicus.eu`) includes all main forcings (i.e., tidal forcing, high-frequency atmospheric forcing, fresh water river discharge, etc.) and is based on a (eddy-resolving) NEMO model application run at 1/36° horizontal resolution. The outputs provided by the IBI-MFC used in our numerical model are 3D daily means of fields of temperature, salinity, sea surface height, zonal velocity and meridional velocity and hourly means of surface fields (sea surface height and barotropic currents).

For atmospheric forcing, the outputs from the Weather Research and Forecasting (WRF Skamarock et al., 2008) model implemented at high resolution (3 km) at the Meteorological Service of Cat-

alonia (SMC; `http://www.meteo.cat`) are used. Specifically, the wind velocity, the atmospheric pressure, humidity and temperature, the longwave and shortwave radiation and the rainfall rate are used. Moreover, the turbulent heat fluxes (latent and sensible) are derived from the atmospheric parameters using the bulk parametrization of Fairall et al. (1996).

Finally, the Ebro River discharge is characterized by using data from the Automatic Hydrologic Information System of the Ebro River basin (owned by the Confederación Hidrográfica del Ebro), which has a network of measurement and remote control instruments that transmits and processes data periodically. The data used to force the numerical model consist of daily measurements of river runoff and temperature.

The points where the model results are validated and analyzed (see Figure 3.1b) are selected according to the wind-jet intensification zone. Points A1, A2, A3, V3, V4 correspond to a cross-section where the mean wind velocities are higher (wind-jet axis). Seven additional points correspond to two parallel cross-sections of the previous one which are located "outside" the wind-jet axis (V1, V2 along the west of the wind-jet axis and A4, A5, A6, A7, V5 along the east of it).

2.2 Observations

For validation purposes, data obtained from the Tarragona TG, the Tarragona Coast buoy, the Tarragona deep buoy and the HF radar are used (see Sections 2.3 and 2.4 in Chapter II).

For the study period, the tide gauge (TG) had 98% data availability. The deep water buoy (DB) measures water velocity and water temperature at the sub-surface (nominal depth of 3 m) and wind vectors at 3 m above the sea surface, among other parameters. In this case, data availability reaches 99%. The coastal wave buoy (CB) is a directional wave buoy that includes a temperature sensor. The data availability for this instrument during the study period is 96%.

The HF radar provides hourly measurements of the current velocities in the top meter of the water column with a horizontal resolution of 3 km and a cut-off filter of 100 cm/s. The resulting HF radar validation area after rejecting the points with less than 50% data availavility (see Section 2.4 in Chapter II) is shown in Figure 3.1b. The figure also shows the location of the tide gauge and the buoys, as well as the points used for validation and analysis of the model results. The comparison between HF radar and sub-surface water currents measured in DB shows good agreement for both along- and cross-shelf components. Some statistical values are presented in Table 3.1. The RMSD and r values are 7.52–6.48 and 0.76–0.82, respectively, which are within the ranges found by Lorente et al. (2015).

Table 3.1: Along- (u) and cross-shelf (v) current components statistics from the comparison between the available HF radar data and the available buoy data (DB) for the study period.

	bias (cm/s)	RMSD (cm/s)	r	d
Along-shelf component	1.18	7.52	0.76	0.86
Cross-shelf component	0.02	6.48	0.82	0.90

2.3 Numerical Model Analysis Methods

The first way of showing the results is by means of figures and their visual interpretation. Then, some aspects are analyzed in more detail. In this section the methods used to analyze the model output are presented.

The buoyancy or Brunt-Väisälä frequency (N) is used to study the vertical structure of the water column.

$$N = \sqrt{-\frac{g}{\rho_0}\frac{\partial \rho(z)}{\partial z}} \tag{3.1}$$

where ρ_0 is the reference density and g is the gravitational acceleration.

When studying the surface mixed layer (SML) depth, Lentz (1992) established that it is proportional to wind stress, inversely proportional to vertical temperature gradient and independent of surface heat flux. The author also showed that the SML depth can be characterized by means of the parametrization (Pollard et al., 1972; Weatherly and Martin, 1978)

$$\delta = Au^* \frac{1}{\sqrt{Nf}} \tag{3.2}$$

where $u^* = \sqrt{\tau_s/\rho_0}$ is the shear velocity, τ_s is the wind-stress magnitude, N is the buoyancy frequency just below the SML, f is the Coriolis frequency and A is a proportionality constant. In this manuscript, this parametrization is used with the aim of evaluating the stratification and wind stress effect on the SML depth.

The "international one-atmosphere equation of state of seawater" (Millero and Poisson, 1981) is used to study the contribution of temperature and salinity to the density of the water column. The equation is of the form:

$$\rho = \rho_w + AS + BS^{1.5} + CS^2 \tag{3.3}$$

where S is the water salinity, ρ_w is the water density

$$\begin{aligned}\rho_w &= 999.842594 + 6.793952\times10^{-2}t - 9.095290\times10^{-3}t^2 + 1.001685\times10^{-4}t^3 \\ &\quad -1.120083\times10^{-6}t^4 + 6.536336\times10^{-9}t^5 \end{aligned} \tag{3.4}$$

and

$$\begin{aligned}A &= 8.24493\times10^{-1} - 4.0899\times10^{-3}t + 7.6438\times10^{-5}t^2 - 8.2467\times10^{-7}t^3 \\ &\quad +5.3875\times10^{-9}t^4 \\ B &= -5.72466\times10^{-3} + 1.0227\times10^{-4}t - 1.6546\times10^{-6}t^2 \\ C &= 4.8314e-4\end{aligned}$$

where t is the water temperature.

Several authors have used the momentum balance analysis to investigate the circulation over the continental shelf (Lee et al., 1984; Lentz et al., 1999; Liu and Weisberg, 2005; Fewings and Lentz, 2010; Grifoll et al., 2016b). In the present study, in order to analyze the mechanism that governs the circulation, an estimation of the size of the momentum balance terms is carried out. To do so, the cross-shelf (y-axis) depth-integrated shallow-water equation is used:

$$\underbrace{\frac{\partial\overline{v}}{\partial t}}_{\text{acceleration}} + \underbrace{\frac{\partial\overline{uv}}{\partial x} + \frac{\partial\overline{v}^2}{\partial y}}_{\text{advection}} + \underbrace{f\overline{u}}_{\text{coriolis}} = - \underbrace{\frac{1}{\rho_0}\frac{\partial\overline{p}}{\partial y}}_{\text{pressure gradient}} + \underbrace{\frac{\tau_s^y}{H\rho_0}}_{\text{wind stress}} - \underbrace{\frac{\tau_b^y}{H\rho_0}}_{\text{bottom stress}} \tag{3.5}$$

where $H = \zeta + h$ is the total depth, ζ is the sea surface elevation, τ_s is the wind stress, τ_b is the bottom stress and the overbar denotes a depth averaging:

$$(\overline{k}) = \frac{1}{H}\int_{-h}^{\zeta} k dz \tag{3.6}$$

where k is an arbitrary variable. The pressure gradient term includes the barotropic term (contribution of the sea level slope) and the baroclinic term (density contribution to the depth-averaged pressure gradient):

$$-\frac{1}{\rho_0}\frac{\partial\overline{p}}{\partial y} = -g\frac{\partial\zeta}{\partial y} - \frac{g}{H\rho_0}\int_{-h}^{\zeta}\int_{z'}^{\zeta}\frac{\partial\rho}{\partial y}dz'dz \tag{3.7}$$

3 Results

3.1 Wind Forcing and Wind-Jet Episodes Description

First, a comparison between the wind field from the WRF model and the observational data from DB for the cross-shelf component is presented in Figure 3.2a. The numerical time series agree with the observed ones with a bias of -0.36 m/s, an RMSD of 2.62 m/s, an r of 0.77 and a d of 0.87 for the cross-shelf component. For the along-shelf wind component (not shown), similar values are obtained for the above mentioned metrics: 0.32 m/s, 2.26 m/s, 0.78 and 0.88, respectively.

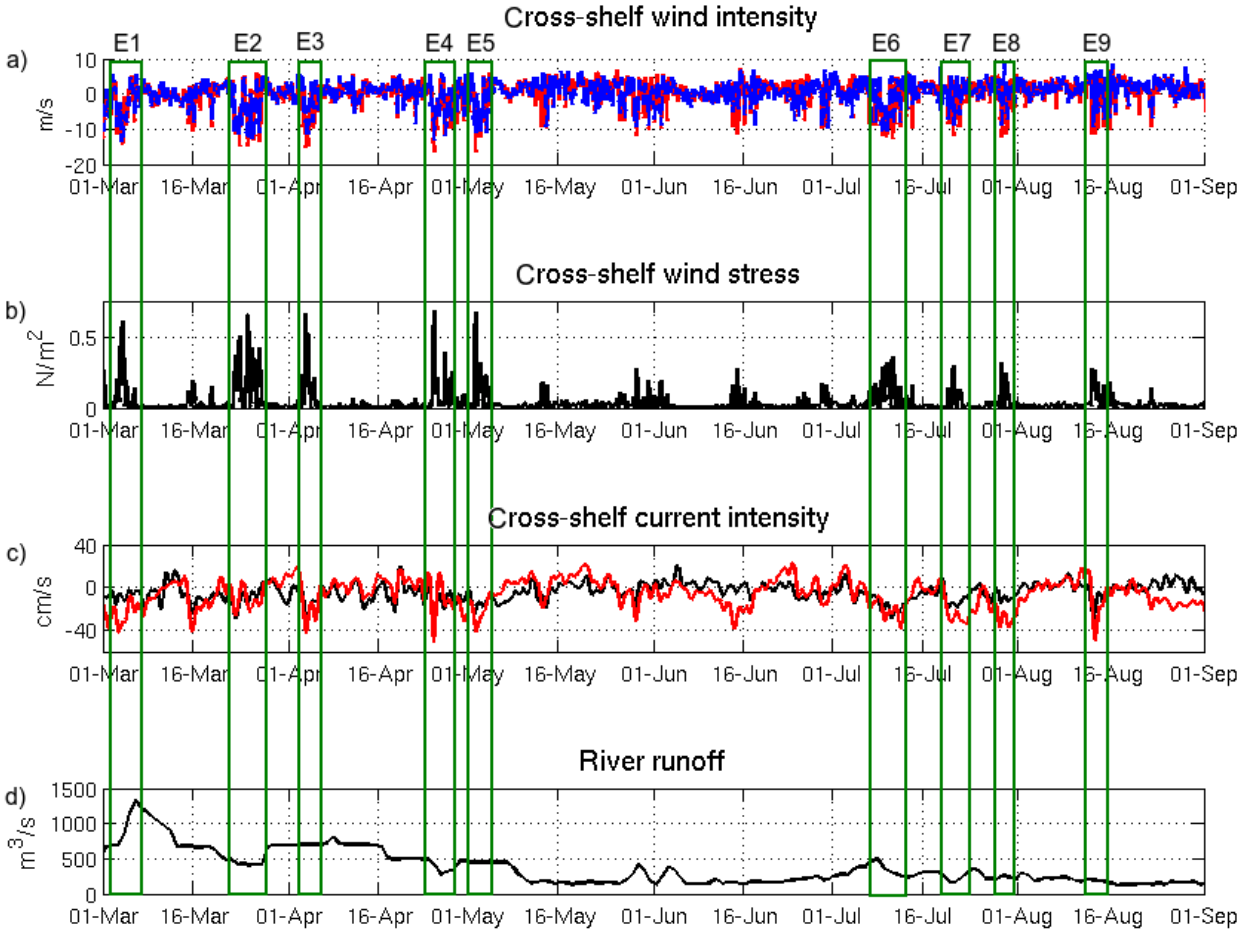

Figure 3.2: (a) Cross-shelf wind intensity comparison. In blue, data from buoy DB and, in red, data from the WRF model. (b) Numerical model cross-shelf wind stress at V3. (c) Filtered cross-shelf current intensity comparison. In black, data from the HF radar and, in red, the numerical model output. (d) Ebro River runoff. The green boxes represent the selected NW wind-jet events. The positive/negative values are according to the axis presented in Figure 3.1.

Wind data show a larger percentage of NW winds from March to May and, uncommonly, also in July. The monthly maximum wind intensities are found in NW winds. The wind-jet events (intense wind from the NW) that exhibit a wind intensity of more than 10 m/s during at least 6 h are marked with green boxes in Figure 3.2. In total, nine episodes are selected (from E1 to

E9). Table 3.2 shows the main characteristics of the selected events at V3, which is approximately located in the wind-jet axis, and some statistics comparing the WRF model data with buoy DB. Mean and maximum values show that during the warmer months, the intensities are lower than during the colder months, which is consistent with previous investigations (Grifoll et al., 2016a). The statistics show that the WRF model is able to capture the wind intensity during the wind jet episodes fairly well, with biases that usually do not reach 1 m/s and RMSD values around 2 m/s. However, it should be noted that this point validation is done at DB, which is out of the wind-jet axis. Most of the events have a duration between 1 and 2 days. It is important to point out that E2 is much longer than the other events because it is an event with three wind peaks. In contrast, event E7 is very short and it has been selected because the hours of wind over 10 m/s are exactly the minimum imposed for the selection. And event E8, although it shows a duration of 1.3 days, is an event of two wind peaks and the sum of both peaks reaches the minimum established hours to be selected.

Table 3.2: Main characteristics of the wind-jet events at point V3 (according to WRF model results) and results of bias and RMSD between the WRF model and DB wind intensity. A negative (positive) bias means that the WRF model underestimates (overestimates).

	Period (dd/mm/14)		Duration	Maximum	Mean	bias	RMSD
	Start day	End day	(∼days)	intensity (m/s)	intensity (m/s)	(m/s)	(m/s)
E1	03/03	05/03	2.0	17.11	10.81	0.24	2.66
E2	22/03	27/03	4.5	16.70	9.43	-0.67	2.45
E3	03/04	04/04	1.5	16.62	11.27	1.89	2.82
E4	25/04	26/04	1.0	17.03	11.69	0.62	1.60
E5	02/05	03/05	1.5	16.62	10.87	-0.29	1.97
E6	09/07	11/07	2.5	13.98	10.07	-0.62	2.17
E7	20/07	21/07	0.75	11.94	8.59	1.60	2.14
E8	29/07	30/07	1.3	11.88	8.33	-0.02	2.54
E9	13/08	14/08	1.25	11.68	9.42	1.55	2.68

3.2 Skill Assessment of the Numerical Model

The comparison between sea level observations at TG and numerical model results reveals an RMSD of 4.48 cm, an r of up to 0.86 and a d of 0.92. The model is able to reproduce the sea-level variations but does not improve the results of IBI-MFC (imposed as boundary conditions), whose error metrics are 4.40 cm, 0.86 and 0.93, for RMSD, r and d respectively. A statistical comparison of the surface temperature between the numerical model results and the observations of the buoys DB and CB is presented in Table 3.3, yielding reasonable agreement between the time series.

Table 3.3: Values of bias (° C), RMSD (° C), r and d for the surface temperature at DB and CB.

	bias	RMSD	r	d
Model vs DB	0.30	1.83	0.93	0.96
Model vs CB	2.26	2.79	0.95	0.91

Some point error metrics of the modeled currents compared with the HF radar data are summarized in Table 3.4. In general, reasonably good agreement is found at points from V1 to V4, with values of RMSD, r and d of 12.51–19.70 cm/s, 0.49–0.68 and 0.65–0.76, respectively. The RMSD present relatively high values because the numerical model currents have higher intensities than the HF radar measured currents. These skill metrics are in accordance with values found in previous works when comparing HF radar measurements with numerical models (Port et al., 2011; O'Donncha et al., 2015; Lorente et al., 2016a). In contrast, at V5, the model does not seem to reproduce the surface water circulation properly.

Table 3.4: Values of bias (cm/s), RMSD (cm/s), r and d for the along- and cross-shelf surface current time series at points V1, V2, V3, V4 and V5 comparing the model results with the HF radar data. All the r values are significant at p-value < 0.01.

	Along-shelf current component				Cross-shelf current component			
	bias	RMSD	r	d	bias	RMSD	r	d
V1	9.13	17.06	0.68	0.76	0.55	12.51	0.50	0.71
V2	0.43	13.88	0.61	0.75	0.24	14.19	0.61	0.75
V3	-0.94	18.18	0.49	0.69	2.20	17.61	0.54	0.70
V4	1.89	19.70	0.50	0.65	3.81	17.42	0.59	0.71
V5	-0.01	20.62	0.23	0.49	7.77	22.89	0.35	0.53

In Figure 3.2c the time series of the filtered surface cross-shelf current intensity from the HF radar and the numerical model are compared. The filtered currents have been calculated using a tenth order Butterworth filter with a cut-off period of 30 h. In general, the model is able to capture the current variability during the wind jets. However the modeled intensities are higher than the measured ones, especially during E1, E7 and E8. A visual comparison of the water circulation observed by the HF radar and that obtained by the model during event E4 is presented in Figures 3.5b and 3.5c. The numerical model is able to reproduce the current pattern measured by the HF radar, but the results show higher current intensities than the measured ones.

A complete visualization of the surface current error metrics in the HF radar domain is presented in Figure 3.3. After computing the RMSD, r and d of the numerical model, a heterogeneous

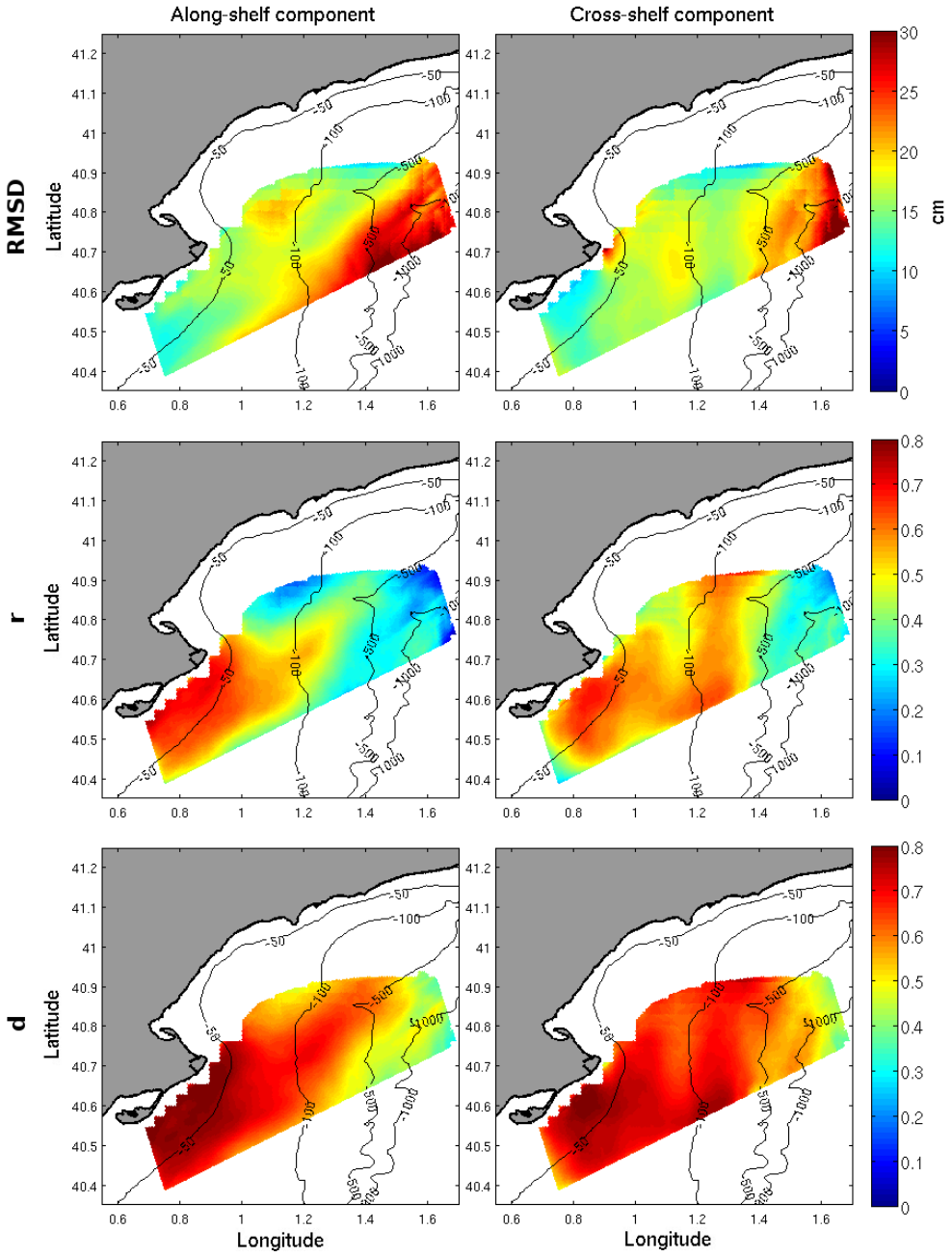

Figure 3.3: Statistical comparison between the numerically modeled currents and the HF radar data. Spatial variability of the RMSD (top), r (middle) and d (bottom) for the along-shelf (left) and cross-shelf (right) surface currents.

pattern is observed. The error metrics revealed good results at the continental shelf but show some discrepancies at the SE corner of the domain, where the depth is more than 1000 m. Two plausible explanations are provided for this abnormal behavior. First, the numerical model is configured with 20 sigma levels, being the vertical representation of this area relatively poor. For instance, at V3 (located at the continental shelf) the maximum distance between vertical layers is 8 m and, in contrast, at V5 (located at the SE corner of the domain, at the continental slope) there are layers that are separated up to 60 m. Second, it coincides with the region where IBI-MFC presents a major discrepancy with the HF radar data (Lorente et al., 2016b); thus, the model results might

be strongly influenced by the quality of the imposed open-boundary conditions. Nonetheless, the aim of this section is to verify the numerical model in shallow regions in order to study the wind-jet response at the continental shelf. For this reason, we exclude the lower right corner of the domain, which is outside of the continental shelf and where the results are not reliable. Finally it is worth noting that the HF radar estimations have an inherent uncertainty (see Table 3.1). For instance, considering the HF radar data as real for reference, the comparison between the HF data and our model provides a mean RMSD of around 15 cm/s, values of r between 0.4 and 0.7 and a mean d above 0.65, which reaches 0.8 at some points. The cross-shelf component shows better agreement with the HF radar data than the along-shelf component.

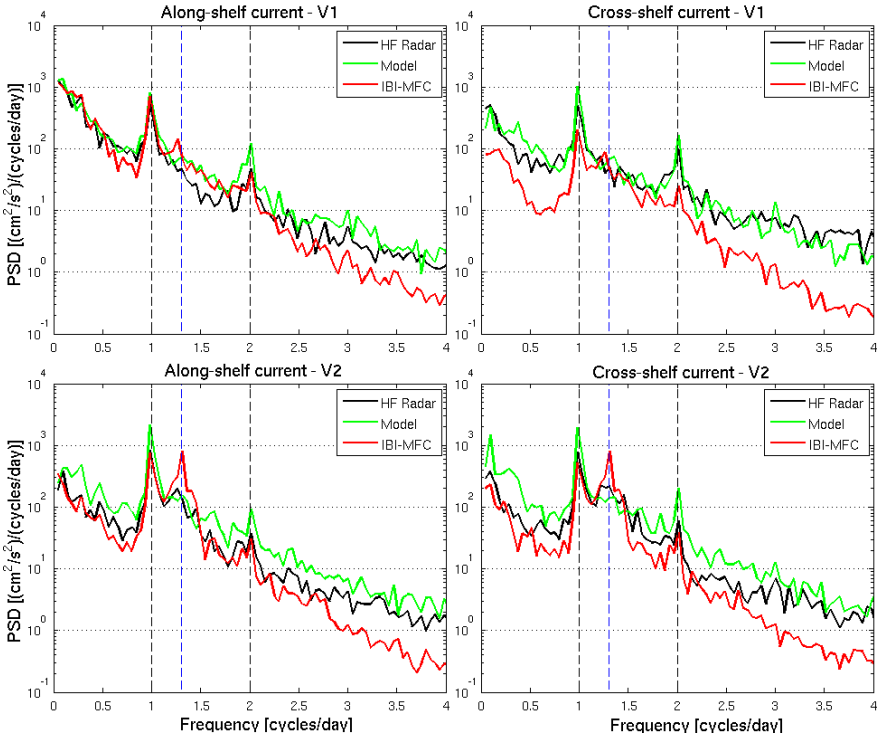

Figure 3.4: Power spectral densities of the along-shelf (left) and cross-shelf (right) surface current components at points V1 and V2. The HF radar data (black) is compared to the model results (green) and the IBI-MFC data (red). The dashed, vertical lines correspond to the inertial frequency (blue) and the diurnal and semi-diurnal frequencies (black).

The energy spectra of the along- and cross-shelf surface current components (Figure 3.4) show that the dominant modes of temporal variability are within the diurnal and inertial frequencies. There is also a nonnegligible peak at semidiurnal frequencies and an energetic band at low frequencies, while after 2 cycles per day (cpd) there is a sequentially drop of energy. Figure 3.4 shows that at V1 the model and the HF radar have a nonsignificant peak at the inertial frequency but IBI-MFC seems to indicate a small peak on the along-shelf component. Then, at V2, the inertial frequency increases in all cases. This behavior is expected, since at V1, which is at 13.3 m water depth, the frictional terms are expected to prevail and, at V2, at 62.2 m water depth, the frictional terms are less important. Another characteristic of the spectra is that the inertial frequency peak is higher at

the points located at the center of the domain (not shown), revealing the prevalent clockwise motion in the area. In general, the IBI-MFC regional model tends to overestimate the inertial frequency in comparison to the HF radar data, while our coastal numerical model better reproduces the energy of this frequency. Also, at high frequencies, the model energy agrees better than IBI-MFC with the HF radar estimations. In contrast, the numerical model tends to overestimate the diurnal and semidiurnal peaks in comparison to the HF radar.

3.3 Wind-Jet Events Analysis

The E4 event is the one that presents a more homogeneous wind field and a clear rise and fall of wind intensity. For this reason it has been selected as a representation episode to show a detailed analysis of the evolution of the dynamics caused by the wind jet. The wind jet starts on April 25 at 02:00 (UTC) and peaks at 06:00, with velocities up to 17 m/s. The sequence is shown in Figure 3.5, where the columns correspond to four instants of the wind-jet evolution: before the wind jet starts, during the wind-jet increase, the wind-jet peak and the wind-jet decay. Throughout the wind-jet intensification, the surface currents (Figure 3.5c) intensify according to the increase of the wind intensity (Figure 3.5a) and the flow direction is consistent with the wind. When the wind stress decreases, the surface circulation turns parallel to the coastline, i.e., southwestward, perpendicular to the wind stress. The modeled sea level also presents a consistent sequence with the wind-jet evolution. Figure 3.5d shows the sea level obtained with the numerical model. During the wind-jet peak, a sea level set-down occurs near the coastline as a response to the wind stress.

Figure 3.6 shows the along- and cross-shelf wind stress components and subinertial water current at points A1 (11.3 m water depth) and V3 (76.1 m water depth) throughout the wind jet. The subinertial currents have been calculated using the filter mentioned in Section 3.2. Near the coast (A1), before and after the wind jet, the along-shelf circulation prevails and a northeastward flow is observed. During the wind jet, the along-shelf component becomes less important. In contrast, in deeper regions (V3), the along-shelf flow during the wind jet is intensified and exhibits a southwestwardly flow. The cross-shelf circulation show a well-defined two-layer structure in both shallow and deep waters. This two-layer structure is characterized by a surface circulation that flows offshore and an onshore flowing circulation just below it. In deeper regions (V3), the two-layer structure has a return flow below the surface with much smaller intensities than that at the surface. Note that after the wind jet, when an inertial circulation emerges, the two-layer structure gradually disappears but, in deeper regions, the along-shelf subinertial surface circulation keeps flowing southwestward.

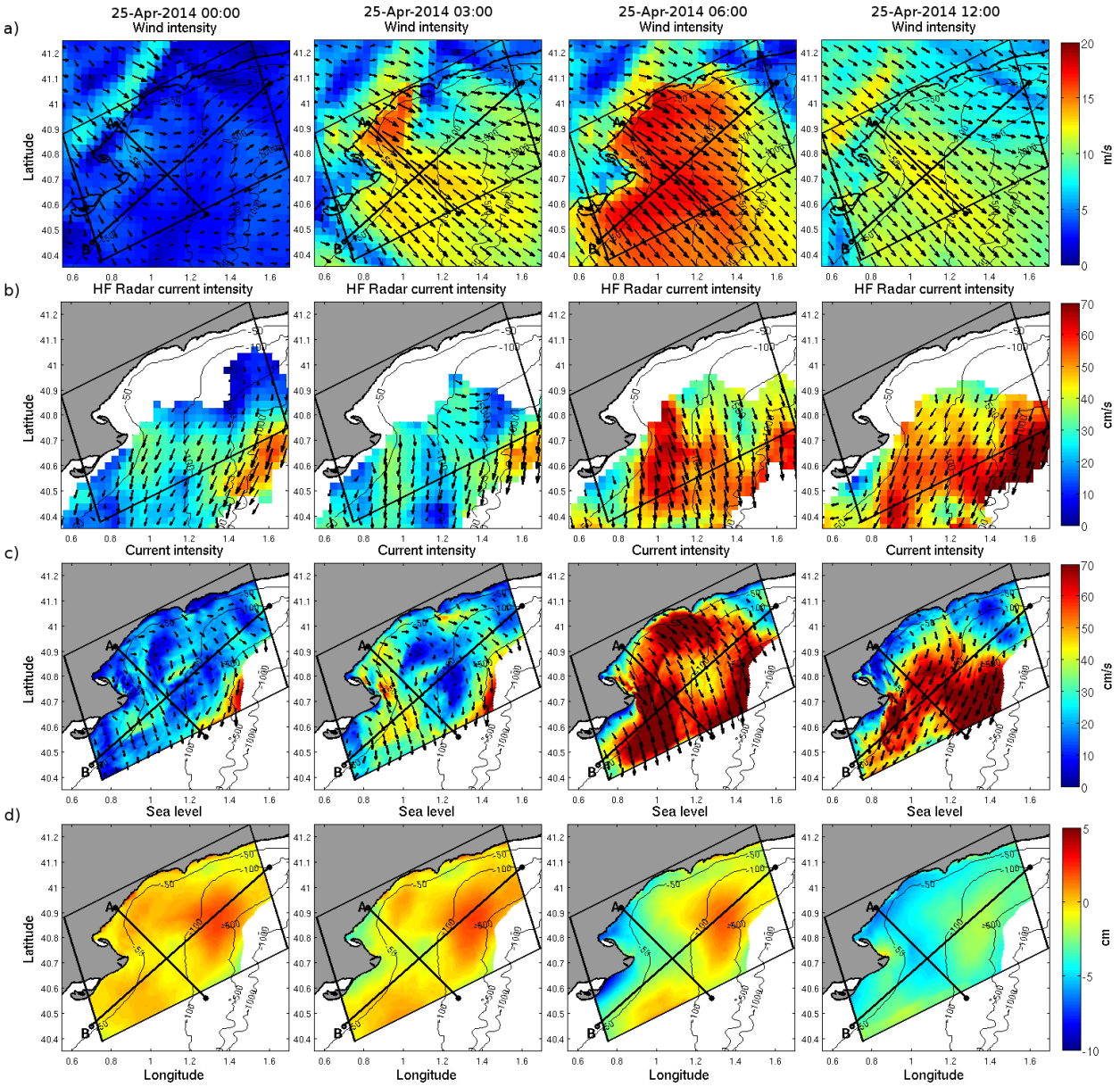

Figure 3.5: Results for the wind-jet event E4. (a) Wind intensity; (b) HF radar current intensity; (c) modeled current intensity; (d) modeled nontidal sea level. For clarity the results are shown up to the mid-slope (i.e., 600 m depth).

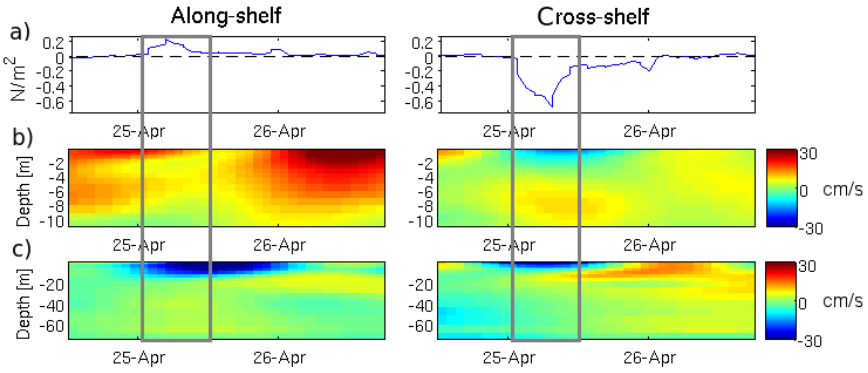

Figure 3.6: Along-shelf (left) and cross-shelf (right) components of (a) wind stress, (b) subinertial water velocity at A1 and (c) subinertial water velocity at V3.

Figure 3.7 presents the evolution of the density anomaly obtained with the numerical model at the same instants as Figure 3.5. The results present an increase of the surface density (Figure 3.7a), which is displaced southwestward, likely due to the advection. In order to analyze the vertical structure, two vertical sections of the density anomaly are used: one following the axis of the wind jet (section A, Figure 3.7b) and one perpendicular to the wind jet (section B, Figure 3.7c). These vertical profiles show that before the wind jet starts, the water column is stratified and that during the wind jet the stratification decreases and the water column tends to homogenize. This stratification breakdown is more pronounced in the axis of the wind jet. However, from visual inspection, it is not possible to clearly discern if the homogenization process is due to upwelling/downwelling or a mixing process that cools the water surface.

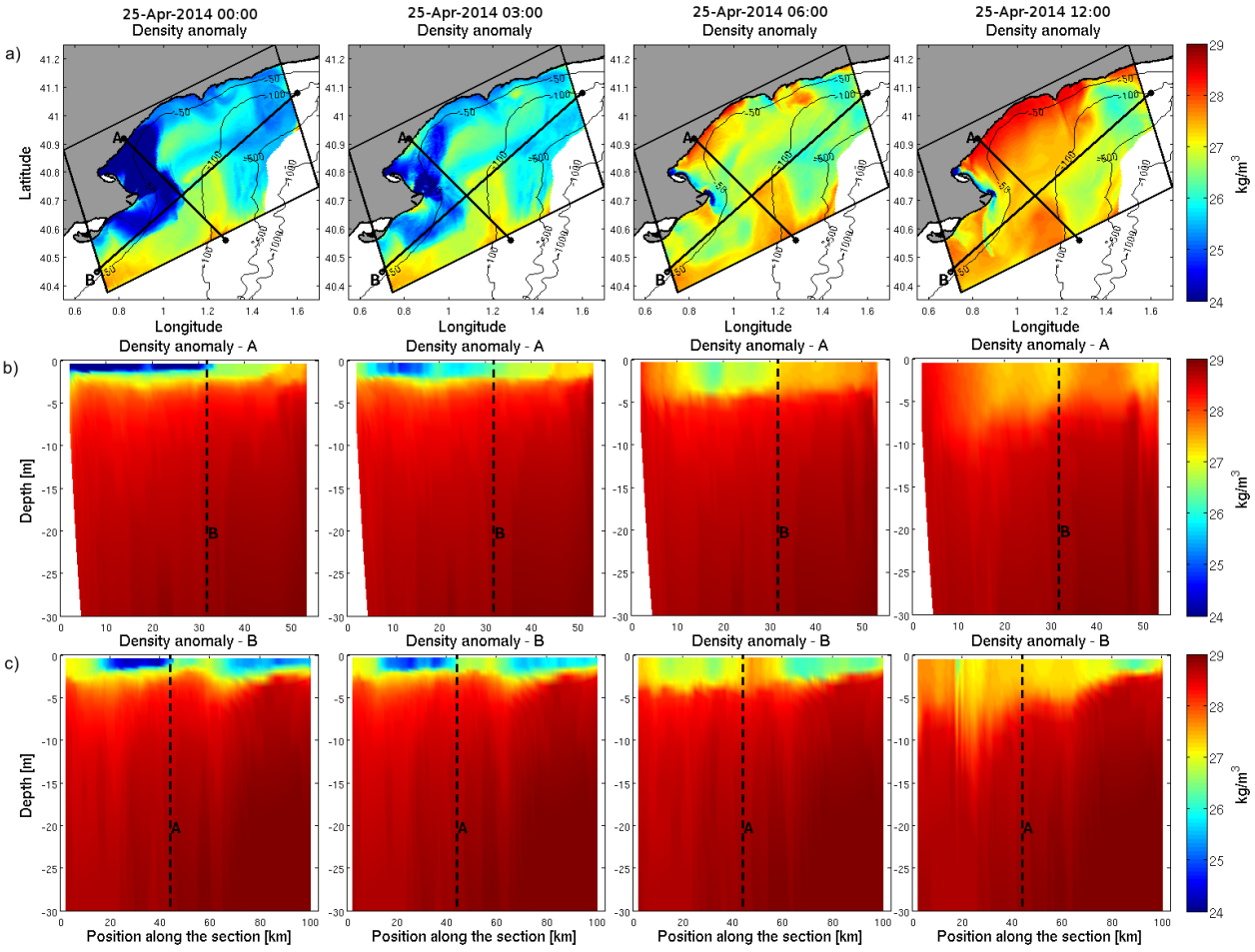

Figure 3.7: Model results of density anomaly during the wind-jet event E4. (a) Results at the surface, (b) a vertical profile of section A and (c) a vertical profile of section B. For clarity, the results are shown up to the mid-slope (i.e., 600 m) in Figure 3.7a, and up to -30 m in Figures 3.7b and 3.7c.

Looking at the temperature and salinity distributions and the vertical velocity profiles at the vertical section B (not shown), it is observed that during the wind jet the water at the surface becomes cooler due to a mixing process and, when the wind jet intensity diminishes, there appears a downwelling region at the west of the wind-jet axis, associated with a downward movement of

the lighter and warmer surface waters. In contrast, at section A there is a clear upwelling region near the coast until approximately 45 m depth (4 km from the coastline), where the surface water temperature becomes equal to the bottom water temperature. Then, moving offshoreward, the water column likely starts to mix. Besides, it is important to note that there is an advection of the surface temperature that also contributes to the changes in the temperature field.

In order to extend the wind-jet response pattern in the vertical column during other episodes, the evolution of the buoyancy or Brunt-Väisälä frequency (N) is investigated. Figure 3.8 shows the Brunt-Väisälä frequency evolution (before and after the wind jet) for the episodes selected in Section 3.1. The selected point is V4, which is far enough to avoid the river plume interference and, therefore, allows a clearer visualization of the results. Different patterns are observed according to the evolution of N. During colder episodes (i.e., E1, E2, E3, which occurred during March and early April), the water column becomes homogenized after the wind jet. In these cases, the wind stress momentum transfer is able to reduce the stratification, resulting in a well-mixed water column, i.e., there are weak vertical gradients. In contrast, during warmer episodes, where the water column is more stratified, the wind-induced mixing is not able to homogenize the whole water column and only a deepening of the pycnocline is observed after the wind jet. In Figure 3.8 it is also observed a reduction of the wind-induced mixing when moving toward warmer months (e.g., E9, which corresponds to August): the resulting SML depth (i.e., the distance between the surface and the top of the pycnocline) becomes thinner after the wind jet. In events E1 and E2, the whole water column becomes mixed, in E3 the SML depth is around 24 m, in E4 is 12 m, in E5 11 m, in E6 is 10 m and from E7 to E9 the SML depth is less than 10 m. These results can be explained looking equation (3.2), where the SML depth increase linearly with u^* and decrease exponentially with N. Thus, the smaller the N is (less stratified), the higher the SML depth becomes.

In order to determine which is the main contributor to water column stratification, the temperature and salinity vertical profiles have been calculated using equation (3.3). The temperature (salinity) contribution to density is calculated assuming constant salinity (temperature). The comparison of these profiles with the density profile (not shown) for all events shows a clear change of the density profile due to a change in temperature (the salinity contribution is almost invariant) except in E1, where salinity plays an important role due to high river runoff, which reaches values of 1300 m^3/s (see Figure 3.2). The fact of having a change in density due to a change in temperature and an unaltered salinity, indicates that the water column in this point is under a mixing process.

The numerical results show a similar flow structure in all selected events, where a two-layer flow is always originated. Figure 3.9 presents the wind intensity and the current vertical profile along section A for two events: E4 (less stratified and higher wind intensity) and E9 (more stratified

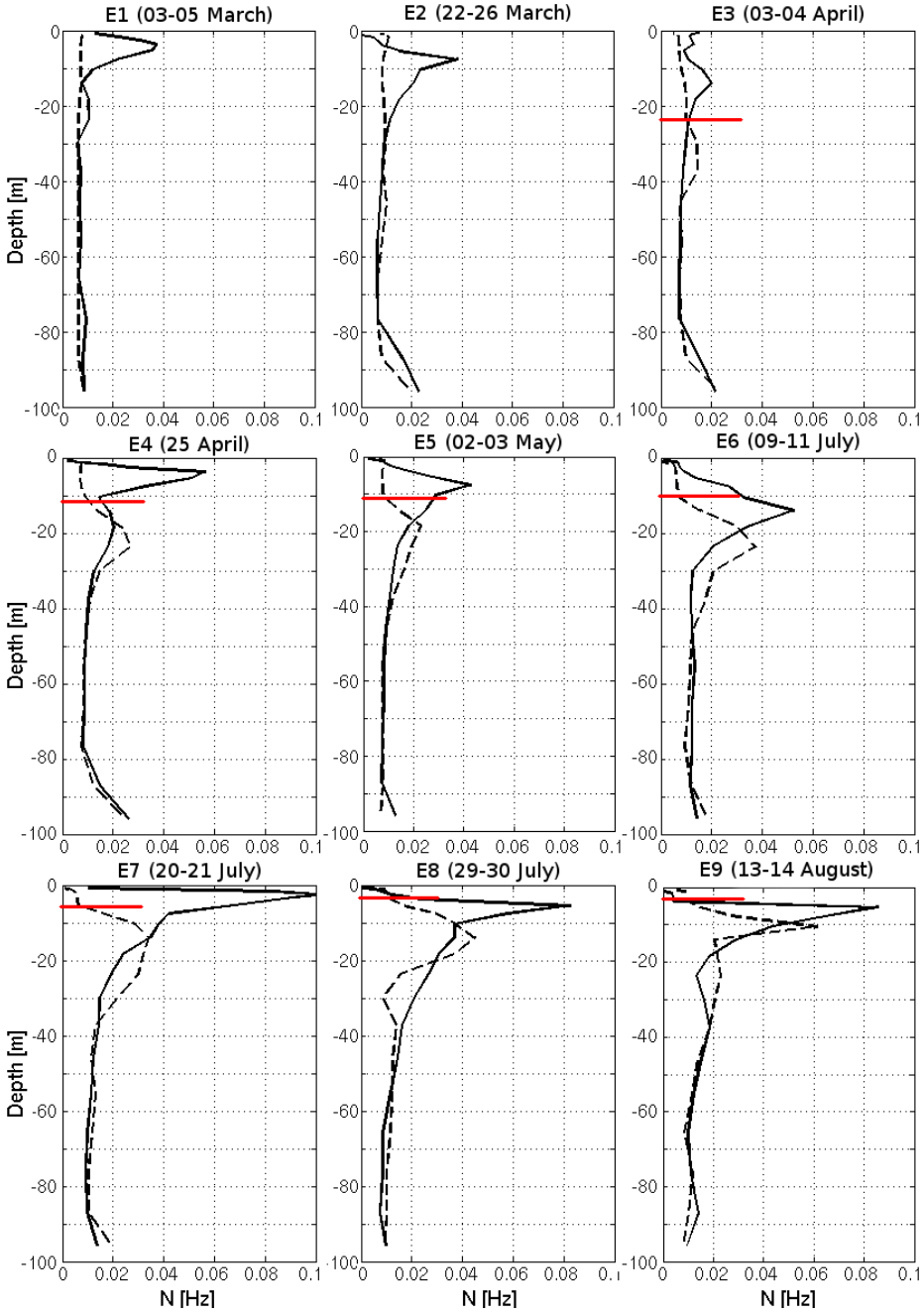

Figure 3.8: Evolution of the Brunt-Väisälä frequency at the start of the wind jet (solid line) and at the end of it (dashed line) at point V4 for all wind-jet episodes (E1–E9). The red lines are the SML depths.

and weaker wind intensity). During E4, the two-layer structure occupies the whole water column (the onshore return flow reaches the bottom). In contrast, in event E9, the two-layer cross-shelf circulation is clearly confined to the SBL (below that, where the return flow ends, the circulation is almost nonexistent). This indicates that the transition from inner to mid-shelf occurs in shallower waters. During less stratified events (e.g., E4), the SBL intersects the bottom in almost the whole domain (most of the section is at the inner shelf), while in more stratified events (e.g., E9) the SBL is thinner, and thus, the intersection with the bottom is reduced, i.e., the inner shelf is narrower, and most of the transverse section is in the mid-shelf.

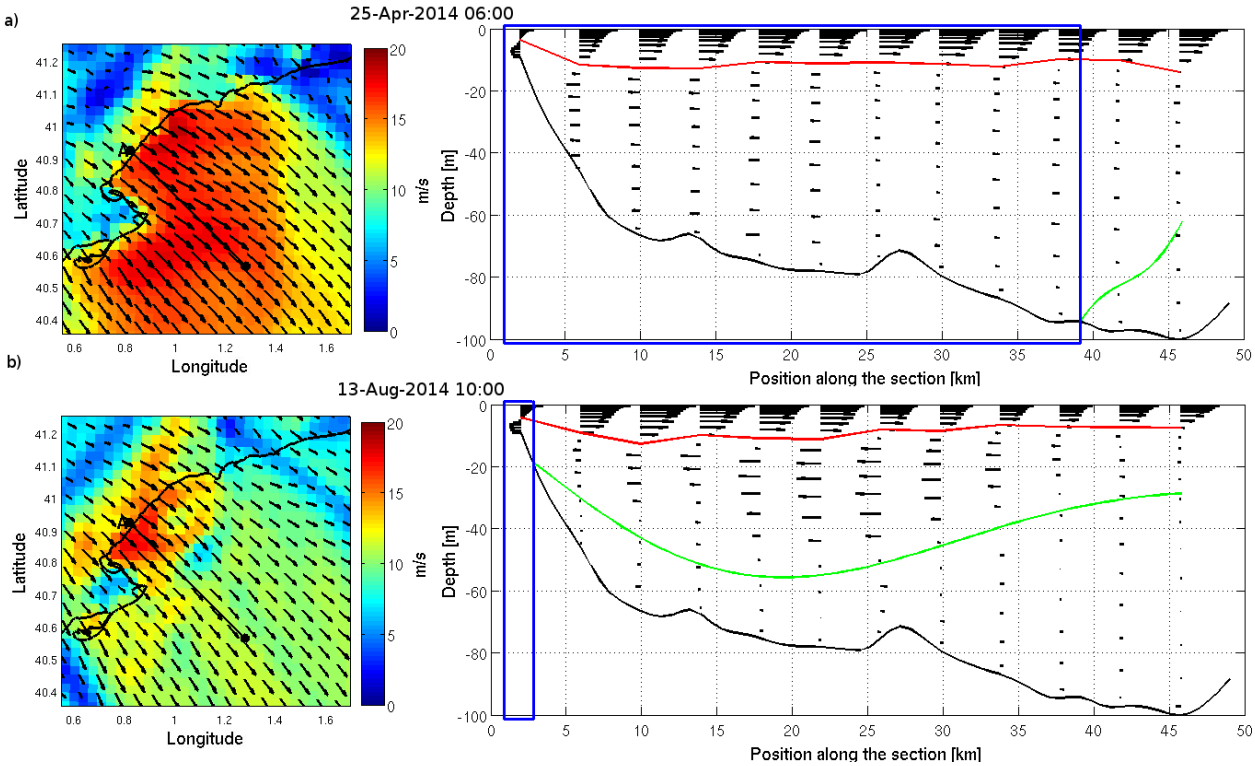

Figure 3.9: Wind intensity (left) and water velocity profile (right) during E4 (top) and E9 (bottom). The vectors of the vertical profile are plotted every six points. The red line is the first zero-crossing (related to the SML depth), the green line is the SBL depth and the blue box delimits the inner shelf region.

Figure 3.9 shows also the influence of the spatially varying wind stress. During E4, when a relatively homogeneous wind field occurred, the first zero-crossing depth (from offshore to onshore flow) is almost uniform along the transect. However, during E9, where the wind along section A is not homogeneous, this first-zero crossing depth is not constant. In this case, when the wind intensity decreases, the upper part of the SBL (where the flow is offshore-ward) is reduced and the SBL becomes smaller.

The results of the cross-shelf momentum balance are presented in Table 3.5. In order to evaluate the relevance of each term, the mean and the standard deviation computed over a period of 12 h are provided. The results are presented at four different points, A1, A2, V3 and V4 (from shallower to deeper waters), and for two different periods: throughout the calm before E4 and during the wind-jet event E4. During the calm period, the flow tends to be geostrophic in the cross-shelf component, with a momentum balance between the Coriolis force and the pressure gradient terms. In some cases, the non-linear terms are also important. This is because during a calm period the along-shelf circulation may become important and, at shallow regions, the bathymetric features can also play an important role. In the course of the wind jet, the relative importance of the dominant terms in the momentum balance is modified. From A2 to V4 the momentum balance shows a balance between the wind stress, the pressure gradient and the Coriolis force term (associated

with the wind-driven along-shelf transport). However, the relative importance of the pressure gradient term tends to diminish moving offshore (to deeper waters). This seems to indicate that there is a transition zone towards a balance between the wind stress and the Coriolis force terms, characterizing a transition to the mid-shelf. Then, in shallower waters (A1 and A2), there is an increase of the relative importance of the non-linear terms and, in A1, the bottom stress term also increases. Nevertheless, at A1 the main momentum terms are the pressure gradient and the wind stress. This is due to the sea-level set-down observed in our results, and consistent with the results presented in Fewings and Lentz (2010) and Lentz and Fewings (2012), since an offshore-ward wind stress balances the cross-shelf pressure gradient with a sea level set-down.

Table 3.5: Estimated mean and standard deviation of the cross-shelf momentum balance terms during a period of 12 h (units are m/s^2 $\times$ 10^{-6}) in A1 ($\sim$11 m depth), A2 ($\sim$47 m depth), V3 ($\sim$76 m depth) and V4 ($\sim$99 m depth) for the wind jet event E4 and before it.

Cross-shelf		$\frac{\partial \overline{v}}{\partial t}$	$+\frac{\partial \overline{uv}}{\partial x}$	$+\frac{\partial \overline{v}^2}{\partial y}$	$+f\overline{u}$	$=$	$-\frac{1}{\rho_0}\frac{\partial \overline{p}}{\partial y}$	$+\frac{\tau_s^y}{H\rho_0}$	$-\frac{\tau_b^y}{H\rho_0}$
A1	Before E4	-0.26	1.48	-2.42	2.86		1.56	0.22	-0.12
		±1.16	±0.60	±0.74	±1.22		±1.09	±0.99	±0.84
	E4	-1.00	0.40	-8.03	5.17		30.31	-28.80	-4.97
		±1.61	±2.91	±2.56	±3.52		±14.98	±18.60	±3.34
A2	Before E4	0.35	-0.10	-1.03	6.64		5.97	0.08	-0.20
		±0.39	±0.95	±0.73	±0.33		±0.64	±0.31	±0.16
	E4	-1.49	-0.18	-3.53	2.58		5.73	-8.06	-0.29
		±0.71	±0.99	±4.47	±2.62		±4.06	±5.52	±0.19
V3	Before E4	-0.56	-1.30	2.70	-2.69		-2.48	0.04	0.59
		±1.00	±0.37	±0.76	±0.85		±1.38	±0.04	±0.16
	E4	0.30	0.29	-0.07	-1.37		3.15	-4.21	0.22
		±1.37	±0.55	±1.62	±1.36		±3.33	±2.71	±0.19
V4	Before E4	-0.22	-0.14	0.53	-2.18		-2.14	0.03	0.09
		±0.43	±0.25	±0.23	±0.79		±0.59	±0.05	±0.05
	E4	-0.79	-0.21	-0.18	-1.47		-0.08	-2.65	0.08
		±1.15	±0.47	±0.78	±0.58		±1.96	±1.88	±0.06

In order to inspect the momentum balance of all the wind-jet events, a ternary plot of the surface stress, pressure gradient and Coriolis terms is shown in Figure 3.10. This ternary plot has been done adding the three terms and calculating the proportion of each one for every wind-jet event at three different locations: A1, V4 and A7. At the shallowest point in the wind-jet axis (A1), all the events present a balance between the pressure gradient and the surface stress terms, with

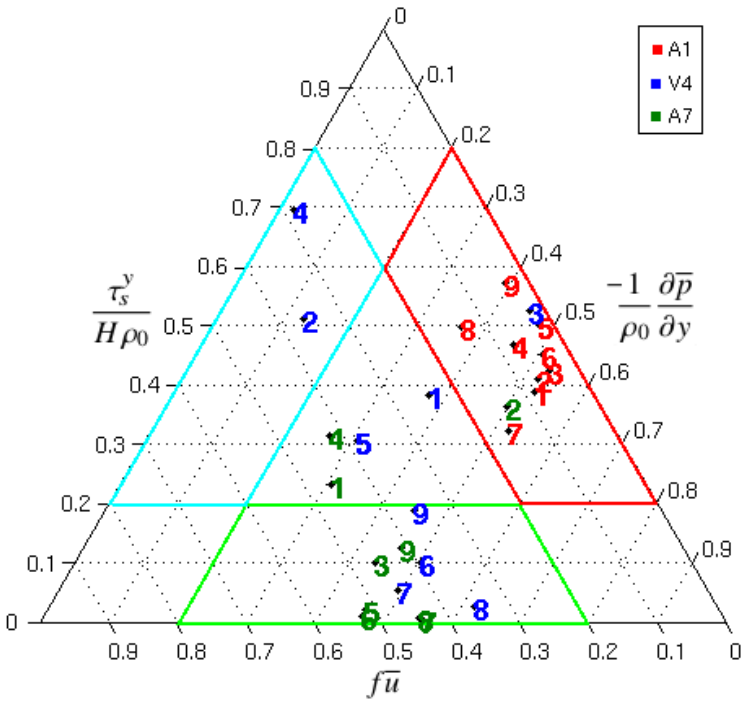

Figure 3.10: Ternary plot between the surface stress, pressure gradient and Coriolis terms for each wind-jet event and at three different locations: A1 (red), V4 (blue) and A7 (green). The color boxes are the regions where the balance is mainly due to two of the three terms. The red box corresponds to a balance between the pressure gradient and the surface stress terms; the green box corresponds to a balance between the pressure gradient and the Coriolis terms; and the blue box corresponds to a balance between the surface stress and the Coriolis terms.

a very small contribution of the Coriolis term. Thus, A1 is in the inner shelf for all the events. Going to deeper waters (V4), different behaviors are observed depending on the different events. For event E3, point V4 is still in the inner shelf. For events E1 and E5, point V4 is in a transition zone. For events E2 and E4, the balance is mainly due to the surface stress and the Coriolis terms, thus the point is located at the mid-shelf. Finally, events E6, E7, E8 and E9 show a geostrophic balance, indicating that the region is barely affected by the wind jet and that V4 is located in the outer-shelf. It should be noted that these events are the ones with less wind intensity. Now, looking for the behavior at a point out of the primary wind-jet axis, it is observed that at A7 most of the events present a geostrophic balance (the point is not affected by the wind jet). However, for events E1, E2 and E4, point A7 is affected by the wind jet. This is due to the wider wind field of these wind-jet episodes.

4 Discussion

The theoretical shelf response to cross-shelf winds has been analyzed in previous research. Pond and Pickard (1983) explained that when the wind remains constant in direction but varies in speed, the Ekman transport perpendicular to the wind varies and the upper-layer waters are forced toward or away from each other, generating convergence or divergence. Then, for continuity, the convergence (divergence) is accompanied by a downward (upward) motion, namely downwelling (upwelling). Focusing at the Ebro Shelf, a theoretical shelf response was investigated by Jordà (2005) using numerical modeling under simplified conditions. The author found that during a stationary NW wind-jet episode, the water velocities perpendicular to the wind jet are larger in the axis of the wind jet than at the edges, resulting in a divergence zone in the east (associated with a decrease of surface elevation and an upwelling of denser waters) and a convergence zone in the west (associated with an increase of the surface elevation and a downwelling of lighter waters). The realistic simulations presented in this manuscript have allowed the authors to identify some of the characteristics mentioned above. The sea-surface elevation (see Figure 3.5d) exhibits a clear sea-level set-down throughout the wind jet. Additionally, when the flow is perpendicular to the wind-jet axis, the sea level presents a decrease east of the wind-jet core and an increase to its west. Besides, a downwelling region is observed at the west of the wind-jet axis when the wind-jet intensity diminishes. During the wind jet, the along-shelf current velocity in deeper regions present a structure similar to the model suggested by Pond and Pickard (1983), with a divergence zone east of the wind-jet axis and convergence to its west. However, the transitory nature of the forcing mechanisms and the non-uniform bathymetry lead to complex behavior in the along-shelf direction dominated by along-shelf gradients. This probably explains the increase of the along-shelf flow shown after the wind-jet (Figure 3.6) related to the transient set-down near the coast. In this sense, Csanady (1980) showed that strong cross-shore wind can generate substantial along-shelf flow due to the presence of a trapped pressure field on the inner shelf.

The small upwelling region near the coastline found in our results is consistent with the theoretical study of Pond and Pickard (1983). In this case, when the wind causes the surface layer to move away from the coast but there is no supply of surface water (due to the coast), water from below the surface must rise to replace it. Additionally, this behavior is linked with the two-layer flow structure observed in our numerical results, where water from deeper layers must upwell near the coast to replace the water flowing offshore at the surface. The two-layer flow structure has been previously observed in the Ebro Shelf by Grifoll et al. (2015, 2016a) and is consistent with results of other investigations (Tilburg, 2003; Fewings et al., 2008; Grifoll et al., 2013; Horwitz and Lentz, 2014), where a two-layer flow structure due to cross-shelf winds has been found at the inner shelf. This

two-layer behavior was first investigated by Ekman (1905), who analytically found the existence of an upper current in the direction of the wind and a compensating, comparatively weak current running in the opposite direction below.

Grifoll et al. (2015) used ADCP observations at the Ebro Shelf and observed that during stratified seasons, the intense cross-shelf winds resulted in a well-defined two-layer flow and were more effective at driving offshore transport than during unstratified conditions, when a one-layer structure appeared. Nevertheless, Lentz and Fewings (2012) noted that the flow structure is similar for stratified and unstratified conditions. Previous studies about the influence of the stratification in the cross-shelf transport also exhibit differences. On the one hand, Fewings et al. (2008) noted that stratification suppresses vertical mixing and, therefore, the SBL is reduced, producing a stronger cross-shelf circulation and an onshore displacement of the boundary between the inner shelf and the mid-shelf. Also, Dzwonkowski et al. (2011) found that as stratification increases, the boundary layer extent is reduced and the transport fraction is enhanced. On the other hand, Tilburg (2003) posited that strong stratification or weak winds lead to shallower surface boundary layers and that strong stratification results in smaller upwelling/downwelling zones and a reduction of the cross-shelf transport.

Our numerical results have provided evidence of a complex response to a wind jet, where all events present a two-layer flow structure. In the episodes where the water is more stratified, there is a reduction of vertical mixing and thus, the SML is thinner (similar to Fewings et al., 2008). It has also been observed that when the water column is more stratified or the wind is less intense, the SBL is reduced, agreeing with previous investigations (Fewings et al., 2008; Dzwonkowski et al., 2011; Tilburg, 2003). This indicates that the transition from the inner shelf to the mid-shelf occurs in shallower waters, i.e., the inner shelf region is reduced, which is consistent with results from previous studies (Fewings et al., 2008; Lentz and Fewings, 2012). In order to discern if the differences are due to the different stratification conditions or due to the different wind intensities, a simple test is done. Using equation 3.2 the SML depth along section A is calculated for each event. Then, the effect of wind (stratification) is estimated considering the N (u^*) parameter constant (using as constant value the mean along the section). Finally, the regression slopes when comparing the "real" SML depth with both the SML depths calculated with constant u^* and with constant N have been calculated for each wind-jet event. The results show that for events E1 to E4, the regression slopes for the stratification effect have values ranging from 0.59 to 0.84, while the wind effect has values from 0.13 to 0.38. In contrast, the SML depth for events E5 to E9 show regression slopes from 0.10 to 0.45 for the stratification effect and values from 0.54 to 0.85 for the wind effect. A plausible explanation for these results is that for more stratified events, where the SML depth is smaller, the wind plays a more important role because the layer of water where it affects is smaller.

And for the events less stratified, where the SML depth is higher, the wind effect is smaller because the water column where it affects is bigger and thus the stratification plays a more important role.

Regarding the cross-shelf momentum balance, Lentz et al. (1999) distinguished among regions with different dominant momentum balance terms on the North Carolina Shelf. At the inner shelf, the pressure gradient tended to be balanced by the frictional terms (wind and bottom stresses) and, at the mid-shelf, there was generally a geostrophic balance (i.e., a balance between the Coriolis force and the pressure gradient terms). However, the dynamics during a cross-shelf wind is different. In this sense, Lentz and Fewings (2012) distinguished between the inner and mid-shelf responses to a cross-shelf wind stress. They revealed that, at the inner shelf, the bottom stress reduces the along-shelf transport and a pressure gradient develops to partially balance the wind stress. In contrast, at the mid-shelf, the wind stress is balanced by the Coriolis force and there is no pressure gradient. In the present study, it has been found that, during a calm period the flow is geostrophic, as expected according to other research (e.g. Lentz et al., 1999; Liu and Weisberg, 2005; Fewings and Lentz, 2010). During the wind-jet events, a balance between the pressure gradient and the surface stress terms is observed at shallow waters, which is the typical behavior at the inner shelf. Then, moving to deeper regions, there is an increase of the relative importance of the Coriolis force term. In some events, the Coriolis force term balances with the surface stress term (i.e. the region is located at the mid-shelf), other events present a balance between the three terms (i.e. are in a transition zone) and other events are in geostrophic balance (i.e. not affected by the wind jet). Overall, the momentum balance observed in the results present similar patterns as the reported by Lentz et al. (1999, during the calm period) and Lentz and Fewings (2012, during the wind jet).

5 Conclusions

A numerical model at the north Ebro Shelf has been implemented, run for 6 months and validated, presenting good agreement with observational data. Within the studied period, nine wind-jet events have been selected to investigate the shelf response in terms of water circulation. According to the numerical results, the water circulation response to a wind jet in the NES presents noticeable spatial and temporal variability.

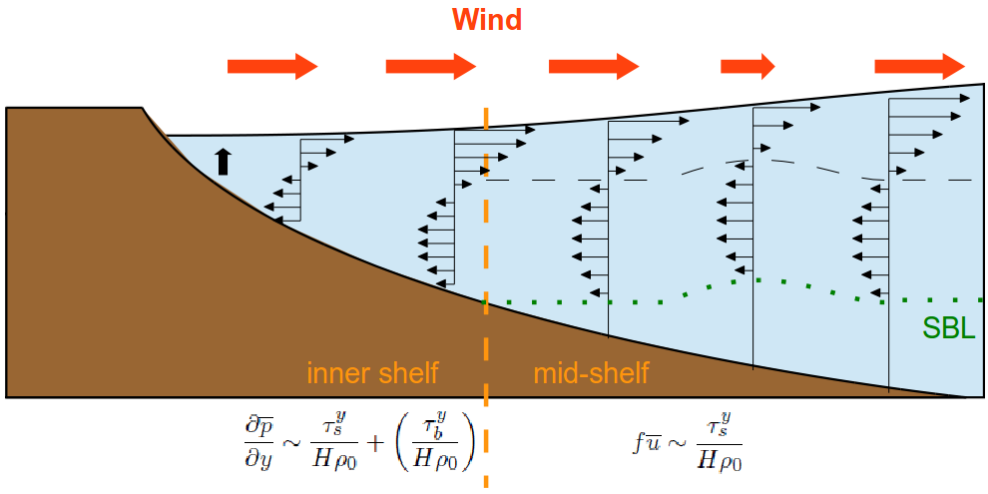

Figure 3.11: Schematic diagram of the cross-shelf response to a non-homogeneous wind jet. The green dots represent the depth of the SBL and the orange dashed line is the transition from the inner shelf (where the SBL intersects the bottom) to the mid-shelf. This transition is displaced onshore when the stratification is higher. The SBL depths vary with the wind intensity. The vertical structure presents a two-layer flow with an upwelling region near the coast (black arrow). A sea level set-down occurs near the coastline. The cross-shelf dynamical balance at the inner shelf is between the pressure gradient and the wind stress term. At very shallow waters the bottom stress term is also relevant. In contrast, at the mid-shelf, the balance is between the Coriolis and the wind stress terms.

A schematic diagram of the main results is presented in Figure 3.11. During the wind-jet events, the cross-shelf circulation at the wind-jet axis presents a well-defined two-layer structure (offshore flow at near-surface and onshore flow in deeper layers), which is accompanied by a decreasing of the sea level near the coast and the occurrence of upwelling near the coastline. The vertical structure of the water column highly depends on the wind stress and the water stratification. Numerical results show that increasing the stratification reduces the SML and the SBL, thus the inner shelf region is narrower. The buoyancy frequency analysis has revealed that, during colder episodes, the wind momentum transfer penetrates unto deeper layers and the whole water column becomes mixed after the wind jet. During the warmer episodes, the water column presents a stratification reduction but, due to its initially higher stratification, it remains stratified after the wind jet. Finally, the cross-shelf momentum balance results have allowed to discern between the different continental

shelf regions. At the wind-jet axis, all the events exhibit a balance between the pressure gradient and the surface stress terms at shallow waters (indicating that the point is located at the inner shelf). At deeper waters, one event remains at the inner shelf, some events present a balance between the Coriolis force and the surface stress terms (indicating that the point is located at the mid-shelf), other events present a combined balance between the Coriolis, the surface stress and the pressure gradient terms (indicating that the region is in a transition zone) and others are not affected by the wind jet and show a geostrophic balance. The momentum balance at a point out of the wind-jet axis shows that most of the events are in geostrophic balance but some events are affected by the wind jet, due to a wider wind field that reaches the evaluation point.

Chapter IV

Wave dynamics induced by a wind jet

"The breaking of a wave cannot explain the whole sea."

Vladimir Nabokov

The content of this chapter has been published in:

Ràfols, L., Pallares, E., Espino, M., Grifoll, M., Sánchez-Arcilla, A., Bravo, M., and Sairouní, A. (2017). Wind-wave characterization in a wind-jet region: the Ebro Delta case. *Journal of Marine Science and Engineering*, 5(1), 12, doi: 10.3390/jmse5010012.

1 Introduction

In spite of its limited fetch, the NW Mediterranean Sea is able to generate harmful storms. The prediction of such storms near the coast is a difficult challenge for operational oceanography and risk management due to wind interaction with local topography, sharply varying fields, the resulting sea-swell interaction and the influence of the land–sea border (Bolaños et al., 2009). These difficulties are especially true during coastal wind-jet episodes.

In this sense, coastal wind-jet regions are areas with highly complex dynamics due to the occurrence of strong gradients in the wind field and the interaction with local (sea) and remote (swell) wave conditions. The investigation of wave evolution in wind-jet areas is relatively scarce. For instance, Shimada and Kawamura (2006) investigated the fetch-limited wind-wave development under alternating coastal wind-jets and wakes in the Pacific coast of northern Japan. The study in Ralston et al. (2013) investigated the wind-waves in the Red Sea, where different mountain gap wind jets occur and induce an enhancement of wave heights.

The knowledge of wave directional characteristics and energy distribution is of high importance due to its application to marine structure design, coastal engineering, coastal vulnerability assessment and coastal protection (e.g., implementation of an early warning system). In this sense, Wyatt (1994) studied the effect of fetch on the directional spectrum of the Celtic Sea storm waves using measurements from a high-frequency radar. The work in Laface et al. (2015) investigated the variability of wave directions during sea storms and found that it is large for lower sea states (storm tail) and is reduced for storm peaks. Wave modeling is a very useful tool to analyze the spatial evolution of the wave directional response. In this regard, Zhou et al. (2008) used the WAVEWATCH-III wave model to analyze the sea-surface directional wave spectrum under typhoon wind forcing in the South China Sea. And Aijaz et al. (2016) used the Simulating WAves Nearshore (SWAN) wave model to study the wave spectral response to sudden changes in wind direction in finite-depth waters. They found that in a 180° wind turn, the young wind-sea decouples from the old waves, and a bimodal spectrum is observed. In contrast, in a 90° wind turn, the spectrum is rotated smoothly to the new direction and remains unimodal.

The Ebro Delta (NW Mediterranean Sea) is a region where wind jets develop from topographic conditions. The works in Alomar et al. (2014) and Grifoll et al. (2016a) highlighted the strong gradients in wind and wave fields in this region. There are many studies focused on this area, which characterize the wave climate (Sánchez-Arcilla et al., 2008; Bolaños et al., 2009), analyze the wave growth (Alomar et al., 2014; Pallares et al., 2014) and evaluate the wind-wave response during energetic events (Bolaños-Sanchez et al., 2007; Grifoll et al., 2016a). However, there is

not an exhaustive investigation of the wind-wave directional response and its temporal and spatial evolution during a wind jet. For this reason, the purpose of this study is to analyze the directional wave properties in order to characterize the fetch-limited wind-wave development during intense wind jets at the Ebro Delta. With this aim, a state-of-the-art numerical wave model has been implemented and run for two months (from March 15–May 15 2014). This period was selected due to observational data availability and the occurrence of several wind-jet events. A skill assessment of the model is carried out with the available data set, and the usefulness of the wave data from an HF radar deployed at the region is evaluated.

2 Methodology

2.1 Numerical Model

The SWAN numerical model is used in this study. This model has been previously used in the Catalan coast (Bolaños-Sanchez et al., 2007; Alomar et al., 2014; Pallares et al., 2014); thus, it has already been calibrated and validated, providing accurate results. In this study, the SWAN Model v40.91A is configured using the parametrization and coefficients established in the calibration undertaken by Pallares et al. (2014). Non-stationary conditions, spherical coordinates and nautical convention have been selected. The wind growth is computed with a sum of a linear term and an exponential term. For the linear growth, the expression from Cavaleri and Malanotte-Rizzoli (1981) is used, and for the exponential growth, the expression and coefficients of Komen et al. (1984) are used. The nonlinear quadruplet wave interactions are integrated by a fully-explicit computation of the nonlinear transfer with the Discrete Interaction Approximation (DIA; proposed by Hasselmann et al., 1985) per sweep (using default coefficients). For the whitecapping, the Komen et al. (1984) formulation is used with $C_{ds} = 2.36 \cdot 10^{-5}$, $\delta = 1$ and $p = 4$. Finally, the JONSWAP (Hasselmann et al., 1973) bottom friction formulation is added with the default coefficients.

The spectrum is discretized with a constant relative frequency resolution of $\Delta f = 1.1$ (logarithmic distribution) and a constant directional resolution of $\Delta\theta = 10°$. The discrete frequencies are defined between 0.01 HZ and 1 Hz. Above the high-frequency cutoff, a diagnostic tail f^{-4} is added. However, since buoys measure the integral parameters in a limited frequency range, the integral parameters Hs, Tp and wave direction have been calculated within the frequency range 0.03–0.6 Hz, in order to ensure that the modeled and measured quantities can be compared (Pallares et al., 2014).

In order to generate the boundary conditions for the numerical model, a downscaling technique has been used. The entire system consists of three nested domains (see Figure 4.1). The largest one covers the western Mediterranean Sea with a spatial resolution of 15 km and provides boundary conditions to a second-level domain, which covers the Catalan Sea. This one has a spatial resolution of 3 km and provides boundary conditions to the local domain, which has a horizontal resolution of 350 m. This study is focused on this last domain. The initial conditions have been obtained running the model in stationary mode. The bathymetry introduced in the model has a grid resolution of 0.0083° and was obtained from GEBCO (General Bathymetric Chart of the Oceans, www.gebco.net). Finally, for the wind forcing, outputs from the Weather Research and Forecasting (WRF; Skamarock et al., 2008) model run operationally at high resolution (3 km) at the Catalan Service of Meteorology (SMC) are used.

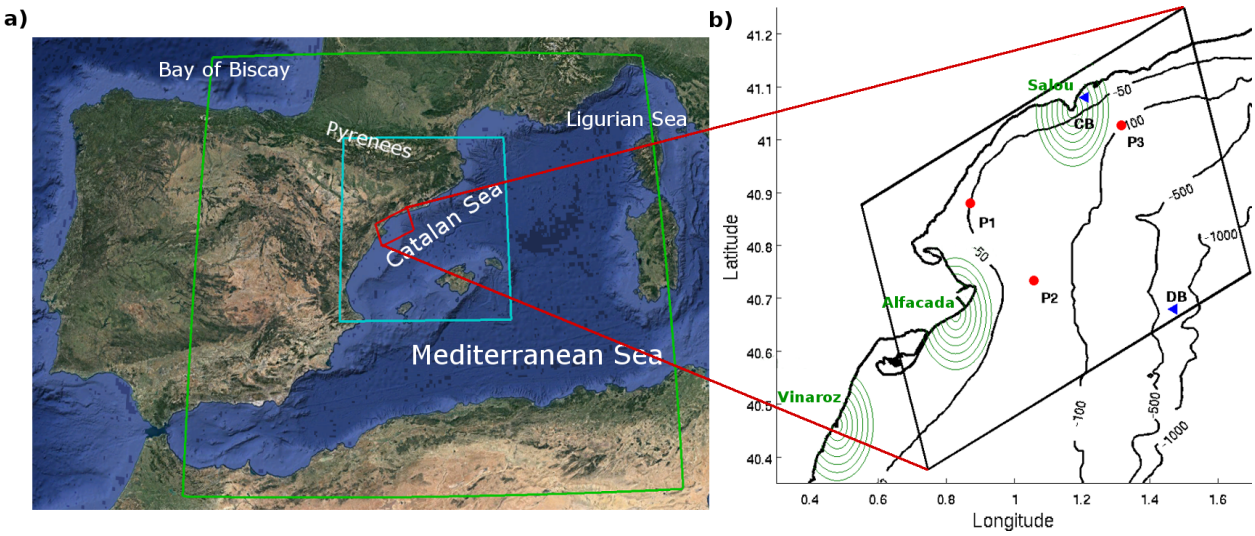

Figure 4.1: a) Geographical location of the Ebro Delta in the NW Mediterranean Sea. Green, blue and red boxes show the three nested numerical domains used in this study. b) Local domain at the Ebro Delta with the HF radar range arcs (in green), the buoy locations (blue triangles) and the location of three points used for analysis (in red: P1, P2 and P3).

2.2 Observations

For validation purposes, data from the Tarragona Coast buoy (CB), the Tarragona deep buoy (DB) and the HF radar are used (see Sections 2.3 and 2.4 in Chapter II). The locations are shown in Figure 4.1b, jointly with the bathymetry and the coastal numerical domain.

Both buoys provide significant wave height, peak period, nautical direction and directional spectra, among other data (the technical characteristics of both buoys are available at www.puertos.es). Additionally, the DB also provides wind intensity and direction data. The spectrum of each buoy is calculated in a different way. DB provides the energy spectrum divided in 14 bands and each band has a fixed fraction of energy. This way, it does not measure in a fixed frequency range because it depends on the amount of energy measured. In contrast, CB calculates a scalar spectrum doing an average of 128 points with a sampling frequency of 1.28 Hz, which corresponds to a Δf of 0.01 Hz. The measured frequency range goes from 0.03 Hz to 0.66 Hz.

In contrast to HF radar current measurements, which are obtained from the first-order peaks in the radar echo spectrum, the HF radar wave data is derived from the second-order radar spectrum (Lipa and Nyden, 2005). The method used to derive the data are based on a least-squares fitting of the radar spectrum with the Pierson–Moskowitz model for the ocean wave spectrum. It assumes that the ocean wave spectrum is homogeneous over the range cell. For this reason, the smaller close-in radar range cells are used for wave analysis (Lipa and Nyden, 2005). It is important to note that measured waves are limited to those felt by the Bragg waves, so the shortest wave period

included in the HF radar data is 5 s (Kohut et al., 2008).

In order to evaluate the HF radar performance, two scatter plots comparing the HF radar data and the measurements at CB are presented in Figure 4.2. The first one (Figure 4.2a) was undertaken with the entire available data period (7 months) and the second one (2 months) with the data corresponding to the study period of this study, which has been selected due to the presence of four NW wind-jet events. The HF radar data used in these comparisons belongs to the data measured at the third arc of the Salou antenna, which is the closest to CB (see Figure 4.1). In order to avoid isolated data points and inconsistent values, the HF radar data has been filtered (see Section 3.2). Both scatter plots present good agreement between the HF radar data and the CB measurements. However, the HF radar tends to overestimate the wave height by up to 0.5 m. It is also important to note the low number of HF radar data points. The HF radar data time series show just 35% data availability.

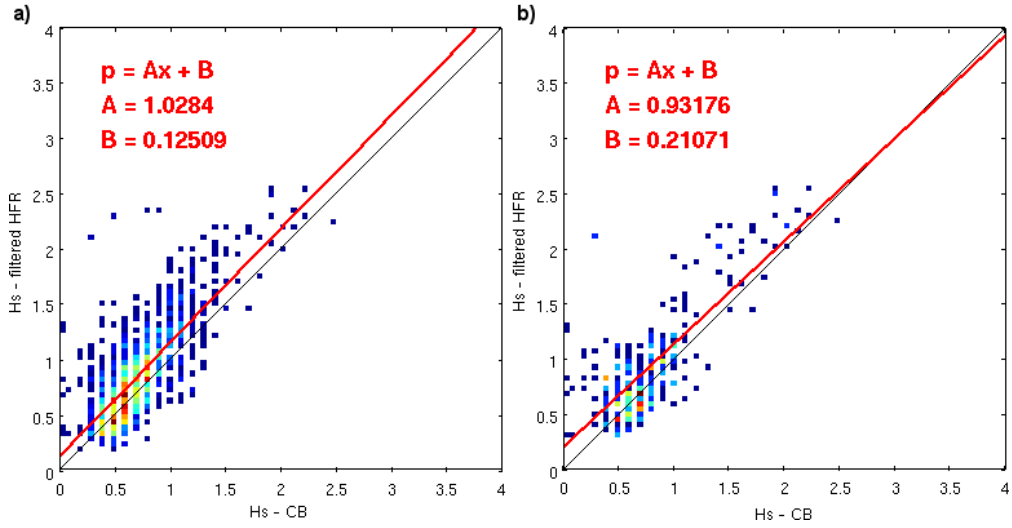

Figure 4.2: Scatter plots comparing the filtered HF radar data versus CB for two data periods. a)The entire available data period (March–September 2014). b) The study period (from 15 March until 15 May 2014)

2.3 Wind-Waves Spectral Description

The irregular nature of wind causes irregular wind-waves with different heights, periods and directions. For this reason, wind-waves are usually described using spectral techniques, where the random motion of the sea surface is treated as a summation of harmonic wave components. Specifically, the variance density spectrum $E(f, \theta)$ is used.

The normalized distribution of wave energy density over directions at one frequency is given by the directional distribution of the spectrum:

$$D(\theta, f) = \frac{E(f, \theta)}{E(f)} \tag{4.1}$$

From that, the directional spreading (DSPR) of the waves can be defined as the one-sided directional width of the spectrum:

$$DSPR^2 = \sigma_\theta^2(f) = \left(\frac{180}{\pi}\right)^2 \int_0^{2\pi} \left(2\sin\left(\frac{\theta - \overline{\theta}}{2}\right)\right)^2 D(\theta, f) d\theta \tag{4.2}$$

The SWAN model computes this quantity as conventionally for pitch-and-roll buoy data (Kuik et al., 1988):

$$DSPR^2 = \left(\frac{180}{\pi}\right)^2 2\left(1 - \sqrt{\left(\frac{\int \sin\theta E(\sigma, \theta) d\sigma d\theta}{\int E(\sigma, \theta) d\sigma d\theta}\right)^2 + \left(\frac{\int \cos\theta E(\sigma, \theta) d\sigma d\theta}{\int E(\sigma, \theta) d\sigma d\theta}\right)^2}\right) \tag{4.3}$$

Local wind-waves (sea system) show a broadband spectrum with a high variety of frequencies associated to irregular sea states. In contrast, waves generated far away (swell system) present a narrowband spectrum with a frequency range with little associated energy. It is well known that sometimes, different wave systems coexist, resulting in a mixed sea (Sánchez-Arcilla et al., 2008). Then, when the sea and swell components exist at the same time, a bimodal spectra occurs.

3 Results

3.1 The wind field

In this sub-section, the quality of the wind input is analyzed (i.e., model versus measured wind data comparison) due to the high sensitivity of the modeled waves to the wind field (Cavaleri and Bretotti, 2004; Ponce de León and Guedes Soares, 2008; Sánchez-Arcilla et al., 2008). Figure 4.3 shows a comparison between the wind magnitude used to force the wave model and the wind measured by DB at 10 m above the sea surface.

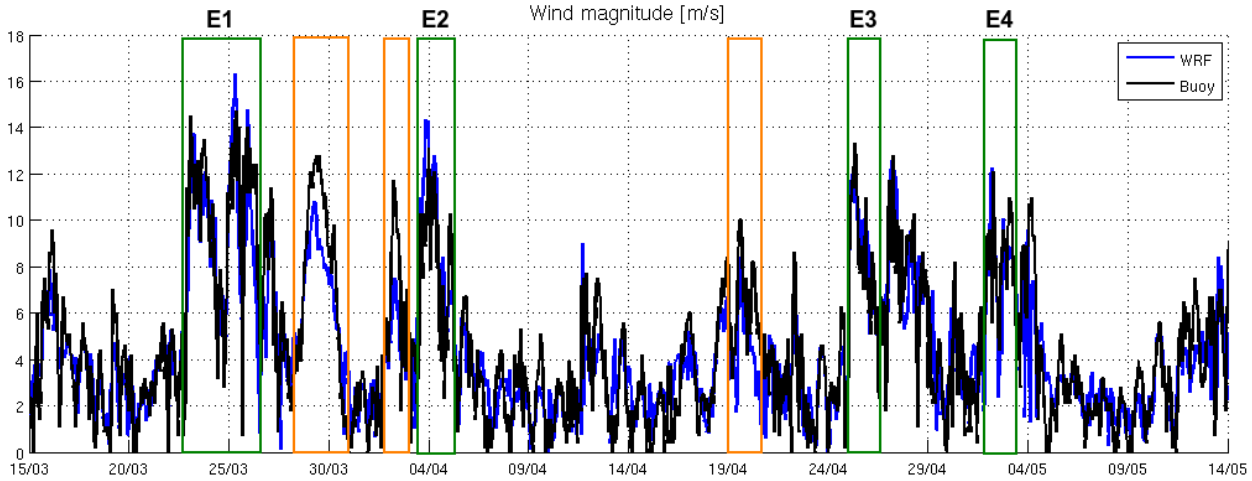

Figure 4.3: Wind magnitude measured at DB (black) compared with WRF model data (blue). The green boxes are the selected NW wind-jet events, and the orange boxes are the most underestimated wind events, which match easterly wind events. Time series data are for 2014.

In general, good agreement is observed between both time series with a bias of -0.13 m/s, an RMSD of 1.82 m/s, an r of 0.83 and a d of 0.91. However, the orange boxes highlight three events where the wind magnitude is clearly underestimated, with biases greater than -1.7 m/s and RMSDs greater than 2 m/s. These events correspond to events with easterly winds. A plausible explanation for this underestimation of the easterly wind events is that the friction velocity parametrization of the operational atmospheric model run at the SMC was adjusted to work properly over the Catalan land area. Thus, when the wind comes from land (e.g., NW wind-jet events), it is properly modeled, but when the wind comes from the sea (e.g., easterly wind events), the friction velocity is too high, and therefore, the wind is too much decelerated. However, the easterly wind events are not the focus of this study. Thus, when ignoring these easterly wind events, the wind field shows good agreement with the buoy data. The selected wind-jet events are marked with green boxes in Figure 4.3, and their main characteristics are shown in Table 4.1. The table includes wind intensity calculated at P2, which is approximately located in the wind-jet axis, and some statistics comparing the WRF model data with DB. Note that DB is not located at the axis of the wind jet.

The table shows that all of the events reaches maximum wind intensities above 16 m/s and have mean intensities above 9 m/s. E1 is the larger event and has less mean intensity because it is a two-peak storm, while the other events are single-peak storms. The statistics present an RMSD around 2 m/s, coinciding with the values usually obtained with the WRF operational model at the SMC, and the biases show good agreement, except for E2, where the model clearly overestimates the wind intensity compared with the buoy measurements.

Table 4.1: Main characteristics of the NW wind-jet events at point P2 according to WRF model results. Error metrics comparing DB data and WRF results are shown in terms of RMSD and bias.

Event	Period(dd/mm/yy)		Duration	Maximum wind	Mean wind	bias	RMSD
	Start day	End day	(∼ Days)	intensity (m/s)	intensity (m/s)	(m/s)	(m/s)
E1	22/03/14	27/03/14	4.5	16.70	9.43	-0.37	2.24
E2	03/04/14	04/04/14	1.5	16.62	11.27	1.65	2.31
E3	25/04/14	26/04/14	1	17.03	11.69	0.35	1.37
E4	02/05/14	03/05/14	1.5	16.62	10.87	-0.29	1.97

3.2 Numerical model skill assessment

In order to validate the numerical model results, the modeled significant wave height (Hs), peak period (Tp) and nautical wave direction are compared with DB and CB observational data in Figures 4.4 and 4.5, respectively. It is important to note that the numerical model has been configured to measure these parameters within a similar frequency range as the buoys in order to be able to perform a reliable comparison. Nevertheless, it is worth noting that the Hs can be somewhat higher than in these time series, since the model and the buoys estimate Hs over a determined frequency range rather than over the entire frequency domain, as happens in nature. Figure 4.4 shows that, at the DB location, the SWAN model is able to capture the NW storm peaks fairly accurately during the four selected events. In all cases, the modeled Hs shows good agreement with the measurements. However, during E2, Hs shows faster decay, probably due to the sudden direction change measured by the buoy, which the model is not able to reproduce. In contrast, Hs is underestimated during the easterly storms, which is consistent with the aforementioned wind underestimation. The Hs during these events show a relative error around 50%.

At CB (Figure 4.5), the three parameters (Hs, Tp and wave direction) show good agreement with the buoy data. In this case, the underestimation during the easterly storms is also present. However, in this case, the NW energetic events selected before do not have a relevant significant wave height. This is because the CB is located near the coast and out of the wind-jet axis, and thus, it is poorly affected by the NW storm. Figure 4.5 also includes the measurements from the HF radar. The

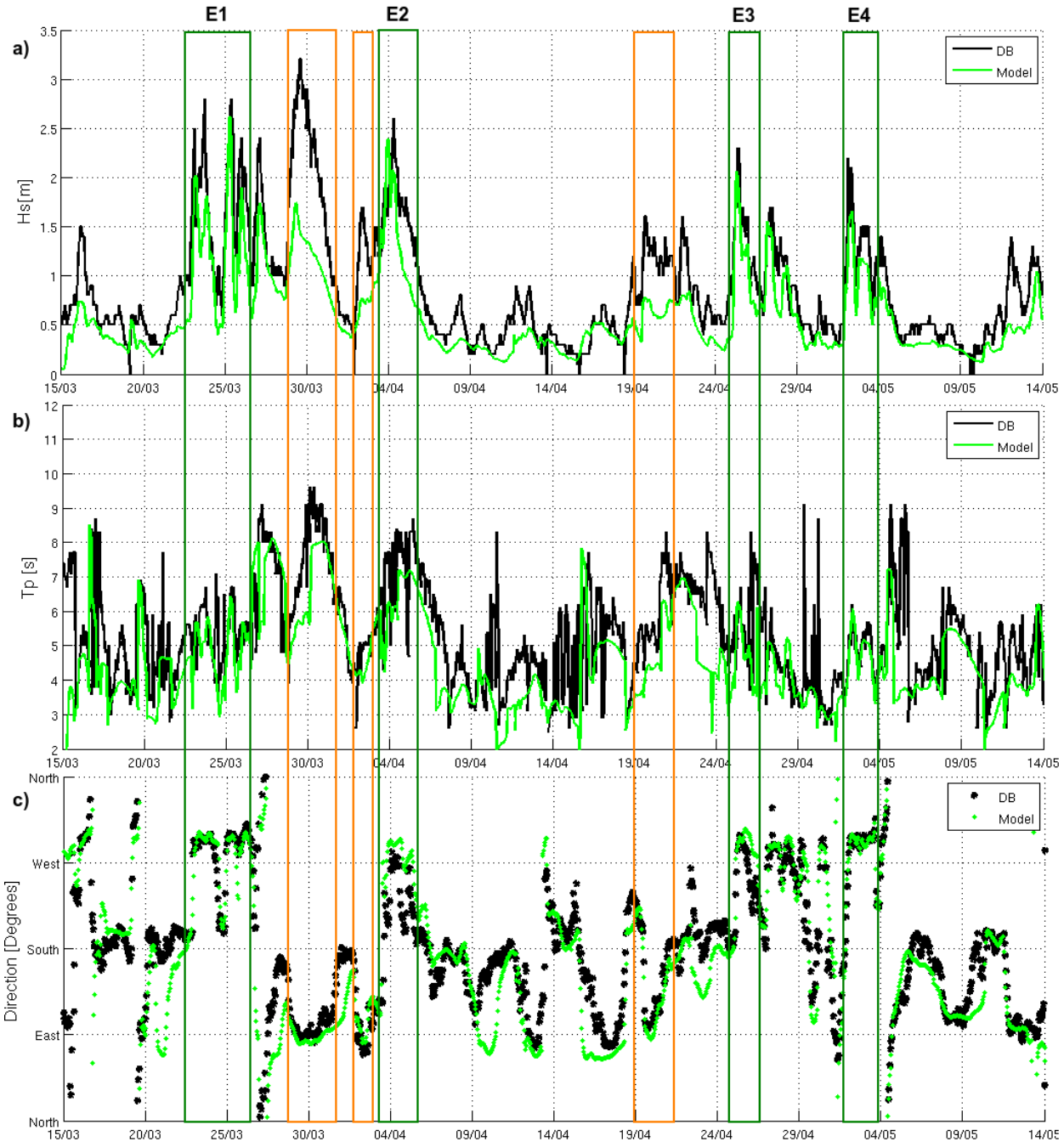

Figure 4.4: Comparison between model results (green) versus observed data at DB (black): a) significant wave height, b) peak period and c) nautical direction. The green boxes are the selected wind-jet events, and the orange boxes are the most underestimated events, which match easterly wind events. Time series data are for 2014.

third arc of the Salou antenna filtered HF radar data has been used in the comparison. Similarly to Long et al. (2011), the filter consists of removing the isolated data points, applying a median filter and eliminating the points where the change in wave height is over a threshold of 0.5 m. Even though the HF radar is able to capture the main pattern of significant wave height measured by the buoy, especially the storm peaks, it is important to note the low number of data points. In addition, as explained in Section 2.4, it can be observed that the shortest wave period included in the HF radar data is five seconds. Concerning the nautical direction, the HF radar data do not fit

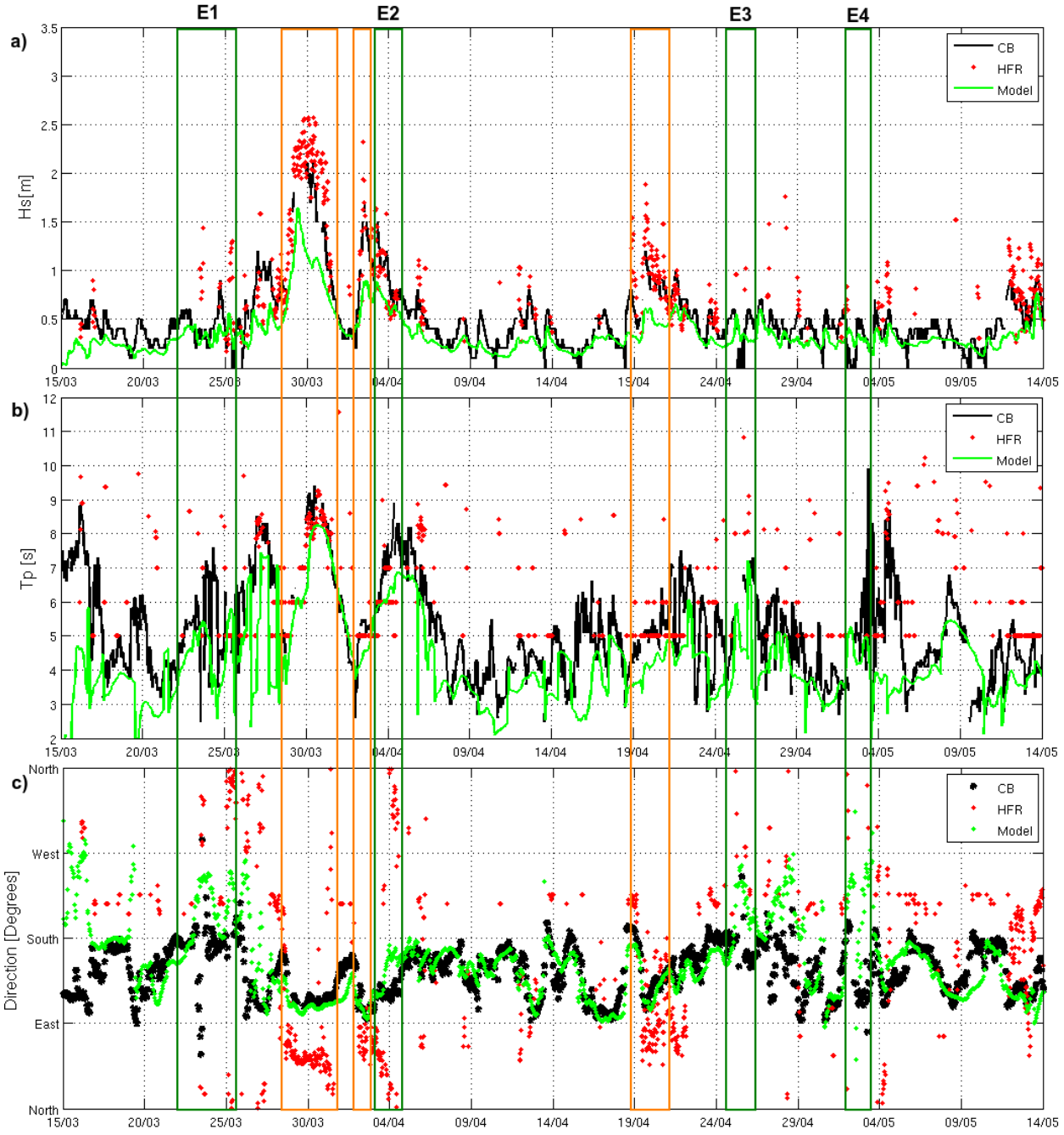

Figure 4.5: Model results (green) versus CB data (black) and HF radar data (red) comparison. a) Significant wave height. b) Peak period. c) Nautical direction. The green boxes are the selected wind-jet events, and the orange boxes are the most underestimated events, which match easterly wind events. Time series data are for 2014.

well with the buoy observations. This is reasonable since the buoy provides a point measurement, while the HF radar assumes that the ocean wave spectrum is homogeneous throughout the range cell. Overall, the HF radar data are useful for a visual validation of the results of Hs and Tp, especially during a storm peak, but due to the scarcity of data, it is not possible to conduct a more thorough validation including a statistical analysis. The usefulness of the Ebro Delta HF radar wave data is further analyzed in Section 3.4.

The statistical analysis results comparing the model results with the measured data at the two

buoys are shown in Table 4.2. The significant wave height shows biases around 0.2 m at the buoy sites and shows a better r and d at the DB location. The peak period present similar biases and RMSDs at both locations, but also presents a better agreement at the DB point. Finally, the mean wave direction exhibits a major variability and much higher agreement at DB than at CB. This is due to a larger variability of wave directions in an offshore position compared to a coastal position, where the directions tend to be more uniform due to the refraction phenomena in coastal areas (note that the CB is moored at a 15-m water depth, while the DB is moored at a 688-m water depth). However, at the same time, this causes higher errors at CB than at DB intrinsically.

Table 4.2: Statistical comparison between the model results and DB and CB data of significant height (Hs), peak period (Tp) and mean direction (Dir), including bias, RMSD, r and d.

	Model versus DB			Model versus CB		
	$Hs(m)$	$Tp(s)$	$Dir(^\circ)$	$Hs(m)$	$Tp(s)$	$Dir(^\circ)$
bias	-0.27	-0.76	-10.00	-0.17	-1.02	4.59
RMSD	0.39	1.46	37.66	0.24	1.66	28.83
r	0.89	0.62	0.81	0.86	0.49	0.48
d	0.86	0.75	–	0.77	0.65	–

Additional validation is carried out in terms of wave spectra because part of the investigation is based on the modeled spectrum. It is important to keep in mind that the SWAN model has been configured as a third-generation model, so it has no a priori restrictions on the evolution of the spectrum (Booij et al., 1999), i.e., the wave spectra are calculated integrating the energy balance equation. In Figure 4.6, the modeled spectrum (calculated between 0.01 and 1 Hz) is compared with the spectra measured at DB (which does not have a fixed frequency range) and CB (which measures between 0.03 and 0.66 Hz) in two time instants: 25 April 2014 at 06:00 UTC (during event E3; Figure 4.6a,b) and 3 May at 04:00 (during event E4; Figure 4.6c,d). Note the different frequency range of the two buoys and the different y scale. The spectrum at CB has much less energy than the spectrum at DB. This difference is also evident in Figures 4.4 and 4.5, where the wave height at CB for those events is around 0.5 m, while at DB, it exceeds 2 m. A first visual inspection shows that the modeled and measured spectra have a similar shape (unfortunately, the tail of the spectrum was not measured). At CB during E3 (Figure 4.6a), the modeled spectrum seems to be more bimodal than the measured spectrum, with more energy at higher frequencies. However, the amount of energy at this point is less than 0.04 m^2/Hz, which makes this difference not relevant, since it is a very coastal point. At the remaining spectra comparisons, the modeled and measured energy are similar except for a few frequency bands, which the numerical model underestimates. The spectra energy differences are consistent with the underestimation of the

waves' parameters (e.g., see the negative biases for E3 in Table 4.2). Nevertheless, it is worth noting that buoy measurements are not error free and that buoys have problems measuring waves with short periods. Overall, the spectra obtained with the SWAN model are considered acceptable to be used as a tool to investigate the evolution of the wave response to a wind-jet.

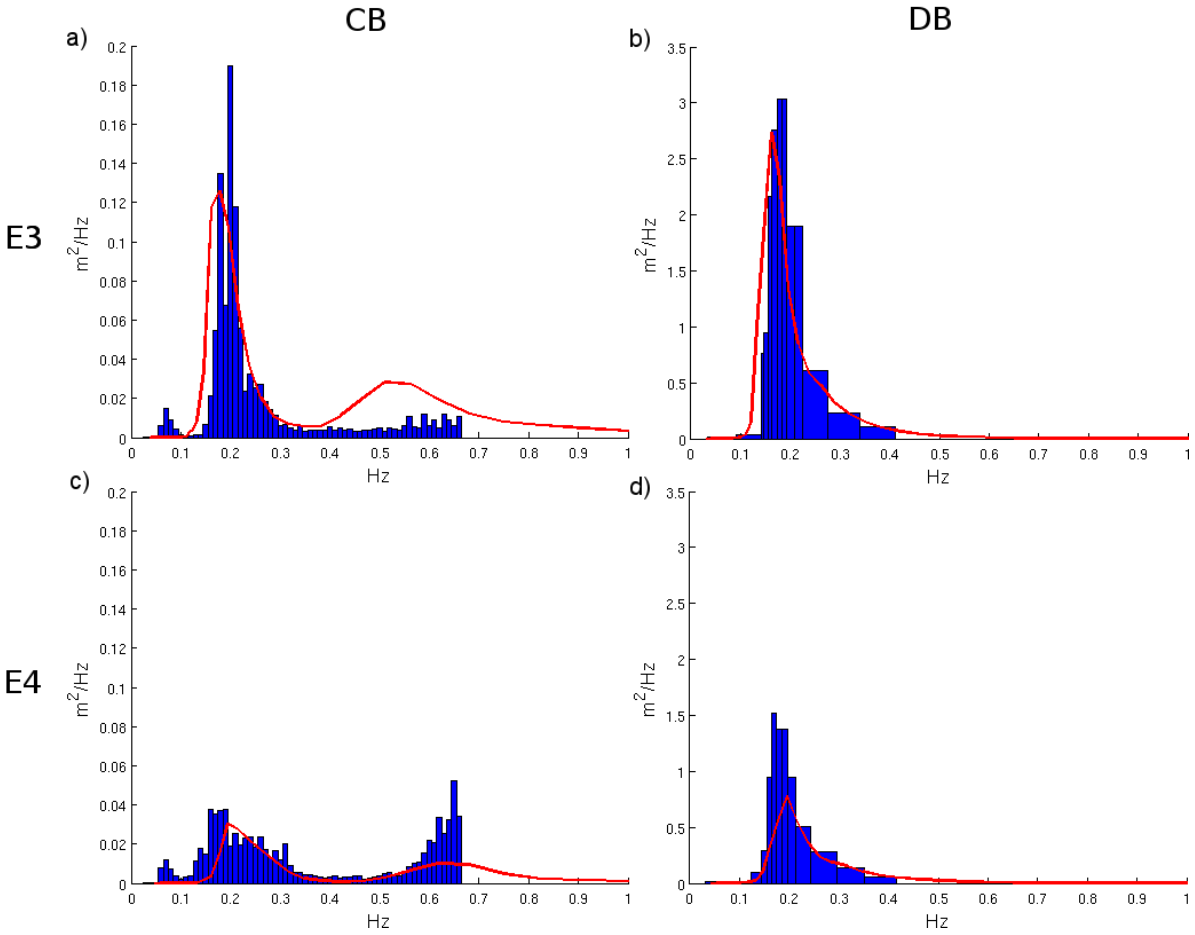

Figure 4.6: 1D wave spectra comparison between the model results (red line) and the spectra measured at DB and CB (blue histogram) at two time instants. a) At CB within E3, b) at DB within E4, c) at CB within E4 and d) at DB within E4. Note the different y scale for the two locations.

3.3 Wave response to a NW wind-jet event

From now on, in order to analyze the wind-jet evolution in time and in space, the numerical model results are used. The wave response during a wind-jet sequence is investigated in terms of the numerical wave spectra evolution. To do so, the event E3 has been selected. This wind-jet starts on 25 April at 02:00 and reaches its maximum intensity at 06:00. It is formed very quickly and fades gradually. Figure 4.7 shows the two-dimensional frequency-direction spectra evolution at the wind-jet axis (points P1 and P2) and out of it (point P3).

Before the wind-jet starts (Figure 4.7a), the wind intensity is small, and all three points show a mostly unimodal spectrum with the spectrum peak located in the south. When the wind-jet starts

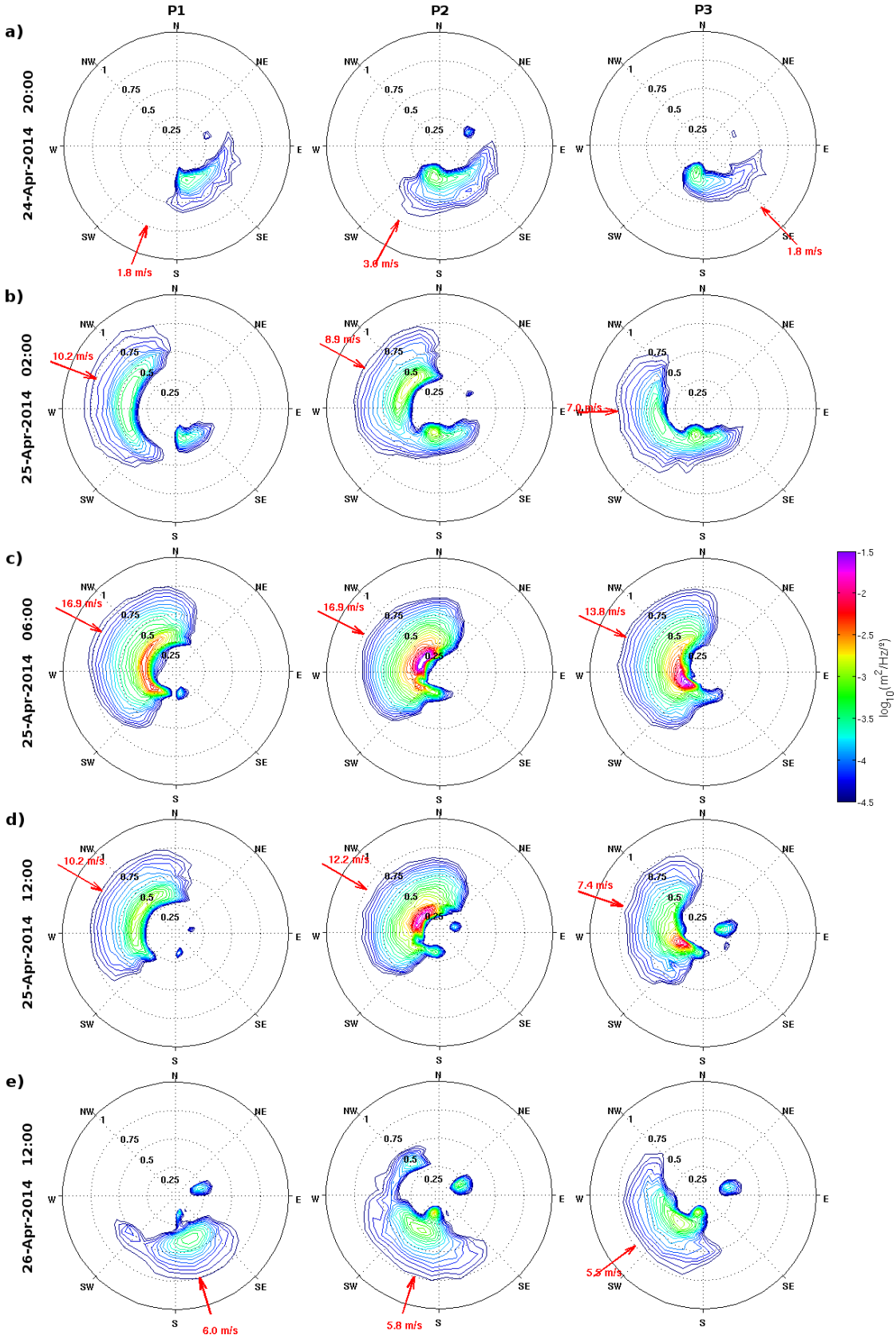

Figure 4.7: Evolution of the 2D variance density spectra during the wind-jet event E3 at P1 (first column), P2 (second column) and P3 (third column). Note that, in order to be able to compare the different spectra, the figure shows the logarithm of the variance density. The red arrows indicate the wind direction and intensity. Panels (a)–(e) show the time evolution.

(Figure 4.7b), the wave field is adapted to the new wind in less than one hour, and two different patterns are observed. At the wind-jet axis, P1 and P2 exhibit bimodal spectra, with a new peak in the wind direction (wind sea system). This peak reaches higher frequencies and is wider than the "old" one, indicating the irregularity of the waves. In contrast, at P3, the spectrum remains mostly unimodal, but it has been expanded to the W, as a result of the wind-jet influence. Then, when the wind-jet is intensified (Figure 4.7c), the spectral energy is also increased. In addition, since the wind-jet becomes wider, the spectrum at P3 is more affected by it and, thus, exhibits a non-negligible energy increase. After the maximum wind intensity (Figure 4.7d), the spectral energy decreases. The remaining energy of the "old" peak is almost irrelevant, and a new peak is observed at the east, corresponding to a swell system. Finally, after 24 hours (Figure 4.7e), a new sea system around the southern direction occurs jointly with the presence of the swell peak in the east and the remaining energy due to the wind-jet in the NW (at point P2).

Comparing the spectrum results in the analysis points (see Figure 4.1), more spectral energy is observed in P2 (offshore) in comparison to P1 (nearshore) due to a larger fetch. In addition, the energy peak in P2 is narrower than in P1 and P3, denoting a lower spreading. This leads one to consider the temporal evolution of the 2D maps in terms of wind intensity, significant wave height and directional spreading, as well as the evolution of these three variables along a section perpendicular to the wind jet (see Figure 4.8). At the start of the wind jet, the wave height and the directional spreading exhibit the clear influence of the wind: an increase of the wave height and a decrease of the spreading is observed at the wind-jet axis. Then, during the maximum intensity peak, the wind jet covers almost the entire domain. The wave height is much higher and the spreading is much less than before, also occupying roughly the entire domain. The inverse effect is observed when the wind jet is diminishing. Finally, at the end of the wind jet, the shape of the wind field distribution can be observed in the Hs and DSPR maps, which show the wind-jet axis clearly defined. In general, the evolution along the section presents a clear positive correlation between the wind intensity and the wave height and a negative correlation between the wind and the directional spreading. Thus, the directional spreading declines offshore-ward along the wind-jet axis and increases on either side of it.

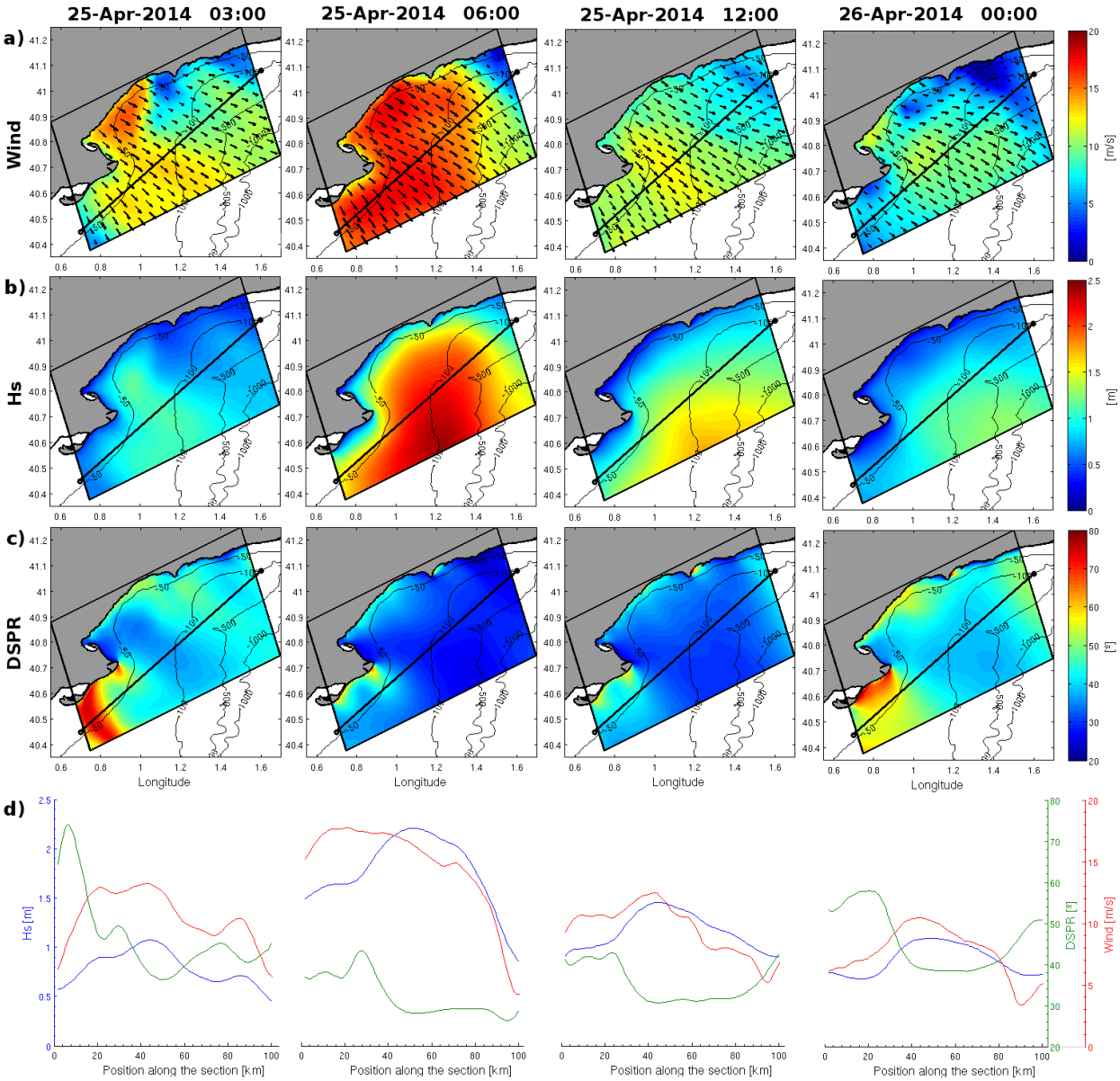

Figure 4.8: Model results for the wind-jet event E3. The figure shows the evolution of a) the wind intensity, b) the significant wave height, c) the DSPR (directional spreading) and d) the profile of the previous variables along the black line plotted in Panels a), b) and c).

So far, just the E3 event has been analyzed. In order to examine if the other three events develop in a similar way to E3, Figure 4.9 is analyzed. It presents the spectra at the start and the end of the wind jet and the evolution of the wind intensity, significant wave height and directional spreading along a section at an instant within the events (analogously to Figure 4.7 and Figure 4.8 for E3). In all cases, multi-modal spectra occur at the beginning of the wind jet. At the end of it, a swell component at the east direction appears due to the northerly winds developed at the northern part of the coast. The behavior observed along the sections is the same as shown above for E3. The wave height follows the wind pattern, and the directional spreading is negatively correlated with the wind intensity.

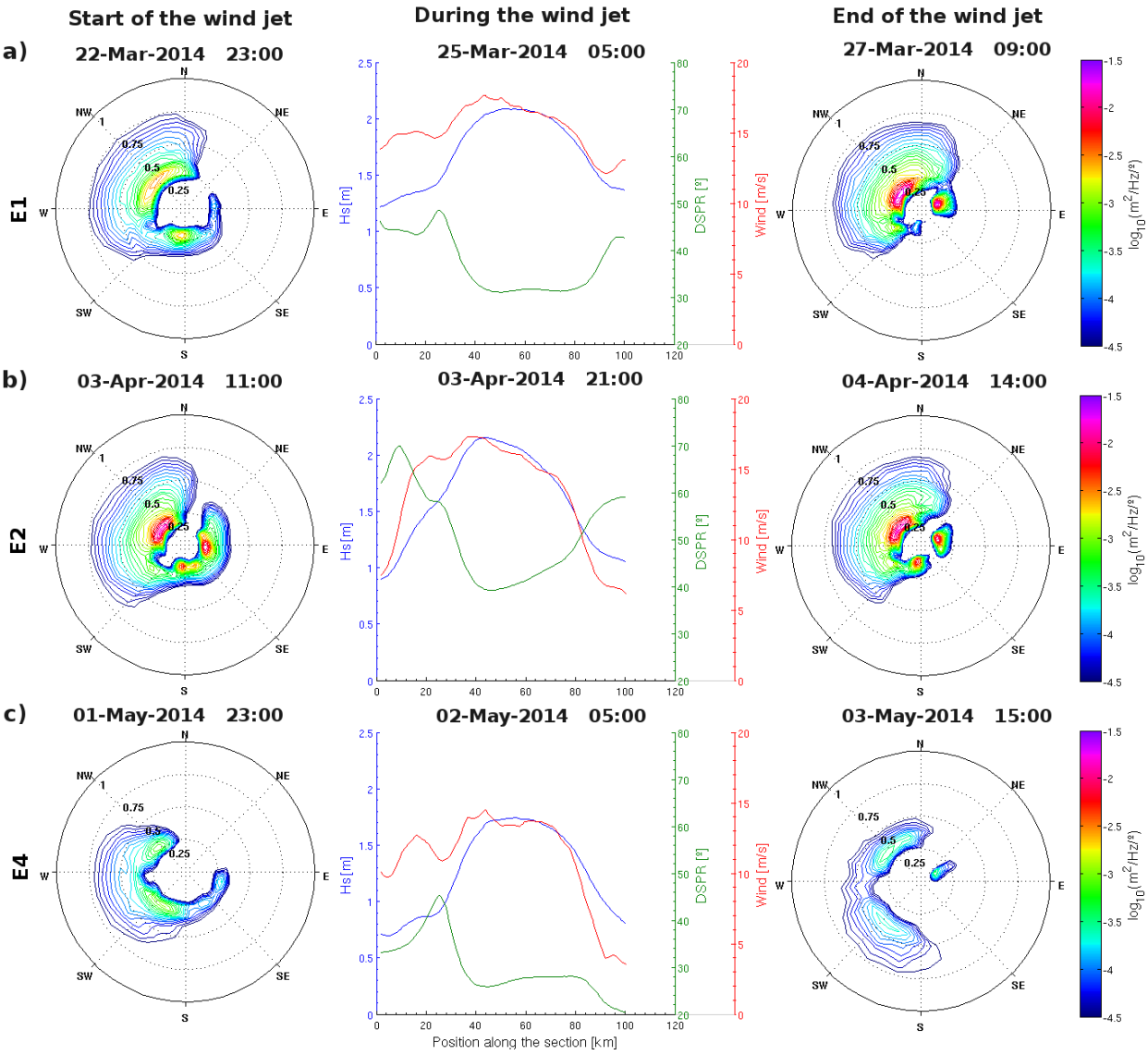

Figure 4.9: Wind-jet response for the remaining events. The spectrum at P2 at the start and the end of the wind jet is presented, as well as a section of the behavior during the wind jet. a) Event E1. b) Event E2. c) Event E4.

3.4 Reliability of the Ebro Delta HF radar wave data

In order to investigate the reliability of the HF radar data, first its raw data are examined. In Figure 4.10, the HF radar raw data are compared with the measured data by CB. There is a relevant data dispersion, many isolated data points and points with unrealistic measurements that reach values up to 16 m. For these reasons, HF radar data must be cautiously post-processed in order to be able to use it properly.

In Section 3.2, the HF radar data of the Salou antenna have been compared with the CB measurements and the model results. As explained earlier, the comparison was carried out by applying a median filter and considering a threshold in a similar way as Long et al. (2011). In their study, Long et al. (2011) performed direct comparisons between median-filtered wave height and period

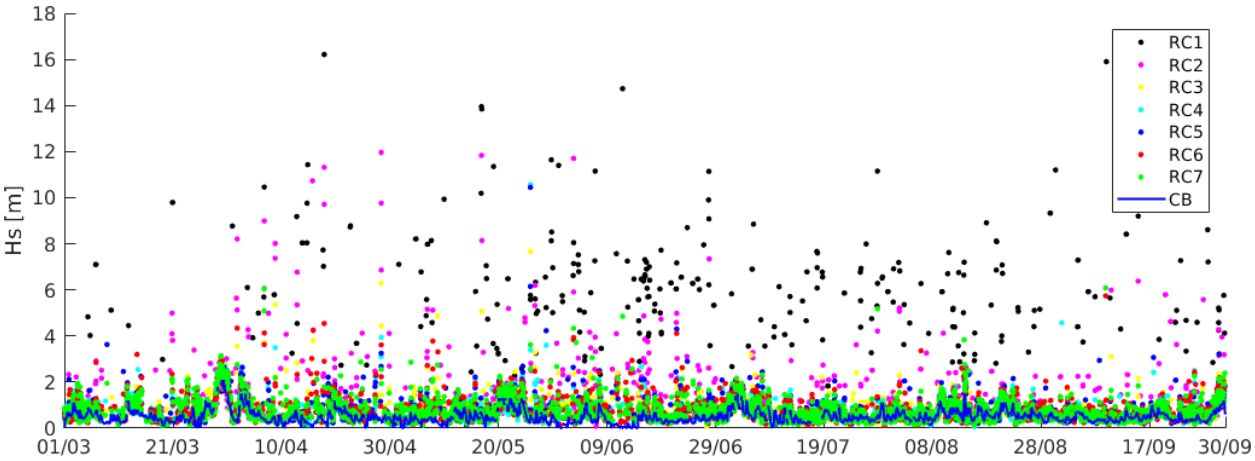

Figure 4.10: HF radar data of the Salou antenna for all of the Range Cells (RCs) compared with the CB measured data. Time series data are for 2014.

data from SeaSonde sites and the closest in situ wave buoy. They removed the SeaSonde points where the data were not available and the points exceeding a 1-m threshold change in less than an hour. In a more recent study, Atan et al. (2016) implemented a selection methodology to identify the proper HF radar range cells to be compared with a Waverider buoy. In order to use CODAR data to perform wave characteristic studies, Atan et al. (2016) selected the useful data considering the percentage of captured data and the percentage of existing outliers. The work in Atan et al. (2016) found that the dispersion of measured data across the selected Range Cells (RCs) was small, which permitted CODAR-buoy comparison by means of average values of useful data from all of the selected RCs.

In order to evaluate the reliability of the Ebro Delta HF radar, the method followed by Atan et al. (2016) is implemented. The Salou antenna is first considered. To start, the differences in Hs between the RCs are calculated. The results show that the differences in RC1 and RC2 are significant in comparison with the other RCs. Then, the outliers presented in Atan et al. (2016) are applied to the HF radar data comparing it with the CB data. Figure 4.11 shows the overview of useful data for each RC based on: (a) 25% outliers, (b) 50% outliers and (c) 75% outliers. It can be seen that 75% outliers presents more useful data, followed by 50% outliers and, finally, 25% outliers. In addition, the calculation of r for each RC (excluding RC1 and RC2) gives values in the range of 0.87–0.96, 0.89–0.91 and 0.95–0.96 for 75%, 50% and 25% outliers, respectively.

Considering all of these results, RCs from 3–7, and 50% outliers have been selected as the most appropriate to be applied, since 75% outliers, although containing more useful data, presents lower values of correlation (similar to Atan et al. (2016)). Now, taking a mean of the RCs from 3–7, the results presented in Figure 4.12 are obtained. The figure compares the mean of the selected HF radar data RCs with the measurements of CB. The results show a good agreement between the

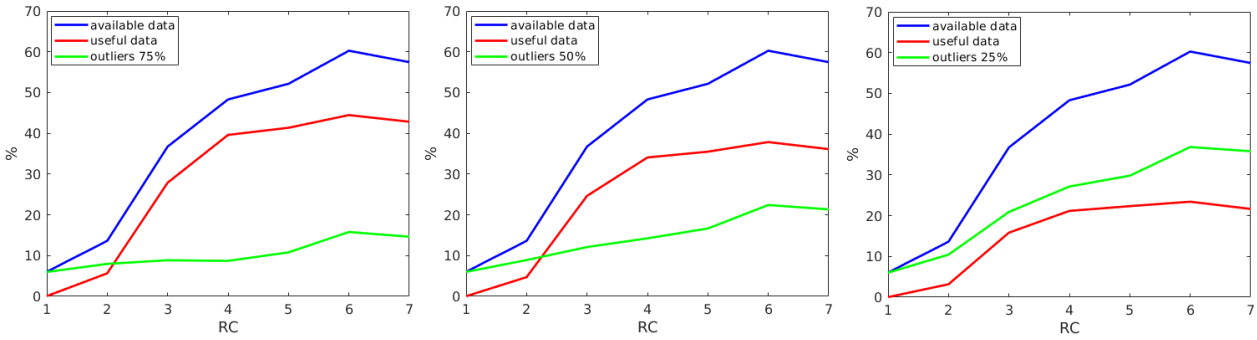

Figure 4.11: Percentage of available data (blue), outliers (green) and resulting useful data (red) for each range cell. a) Applying 25% outliers. b) Applying 50% outliers. c) Applying 75% outliers.

two datasets, with a bias of 0.06 m, RMSD of 0.11 m, an r of 0.92 and a d of 0.95. Therefore, it can be said that the HF radar is able to follow the same tendency as the measured data. However, as in Section 3.2, it is worth noting the scarcity of HF radar data points (only around 30%–40% is useful data). Since the HF radar does not measure waves with periods lower than 5 s, a plausible explanation for the scarcity of data is that most periods at the Catalan coast are between 2 s and 4 s (Bolaños et al., 2009). This, added to the intrinsic loss of measured data of the HF radar, could be the cause for such few data points.

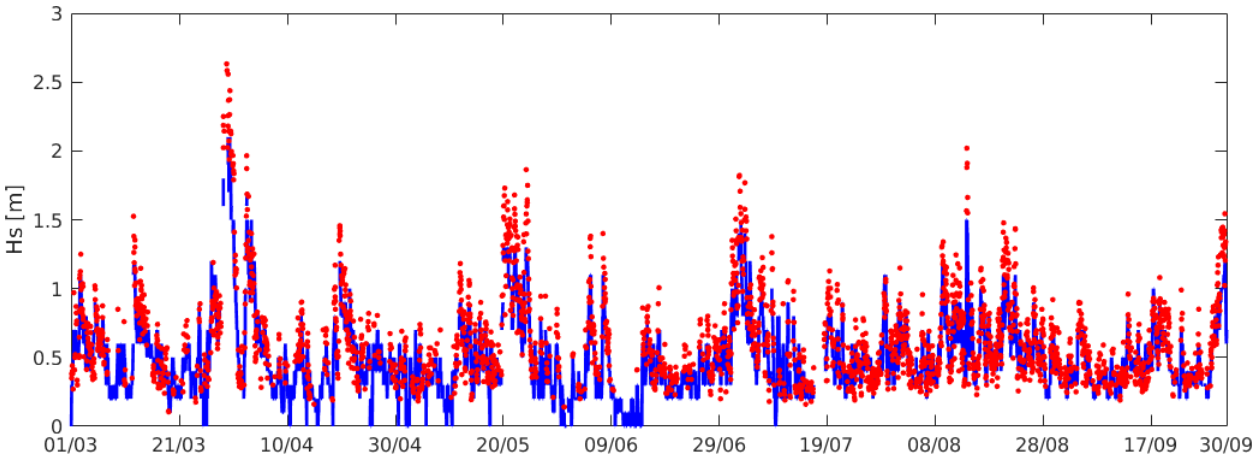

Figure 4.12: Time series comparison between the measured data at CB (blue) and the averaged HF radar data at range cells from 3–7 selected by applying 50% outliers. Time series data are for 2014.

When implementing the same method in the Alfacada antenna, a substantial problem appears: there is no alternative measurement to apply outliers. As Atan et al. (2016) pointed out, a simultaneous set of data from an alternative source (e.g., a buoy) is needed to apply their radar noise filter. For this reason, the authors attempted a method using concepts from both Long et al. (2011) and Atan et al. (2016). First, the Hs differences between the RCs were computed, and as with the Salou antenna, RCs 3–7 were selected. Then, similar to Section 3.2, a median filter and a 0.5-m threshold filter were applied. In this case, the resulting percentage of useful data (see Figure 4.13) is higher than before, since there is also more available data than in the Salou antenna.

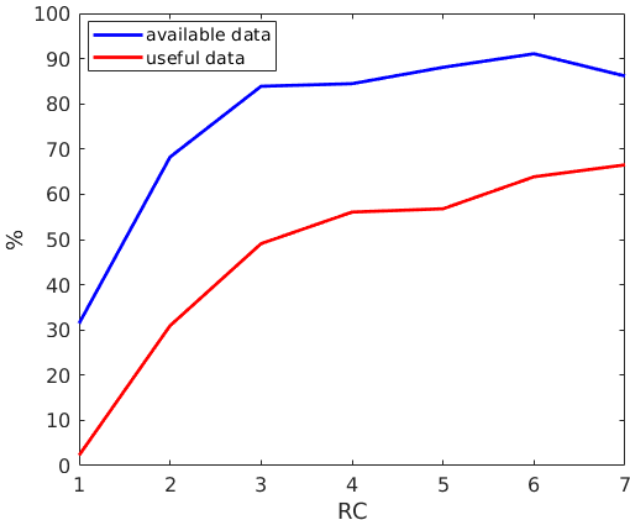

Figure 4.13: Percentage of HF radar data availability (blue) and useful data after applying the filter (red) for each RC.

Lastly, the mean of the resulting filtered data for RCs 3–7 was taken. The final processed HF radar data are presented in Figure 4.14. There are still some isolated unrealistic points, but the data are sufficiently treated to be useful to see the wave height tendency. However, although there are more data points than at the Salou antenna, the scarcity of data remains visible.

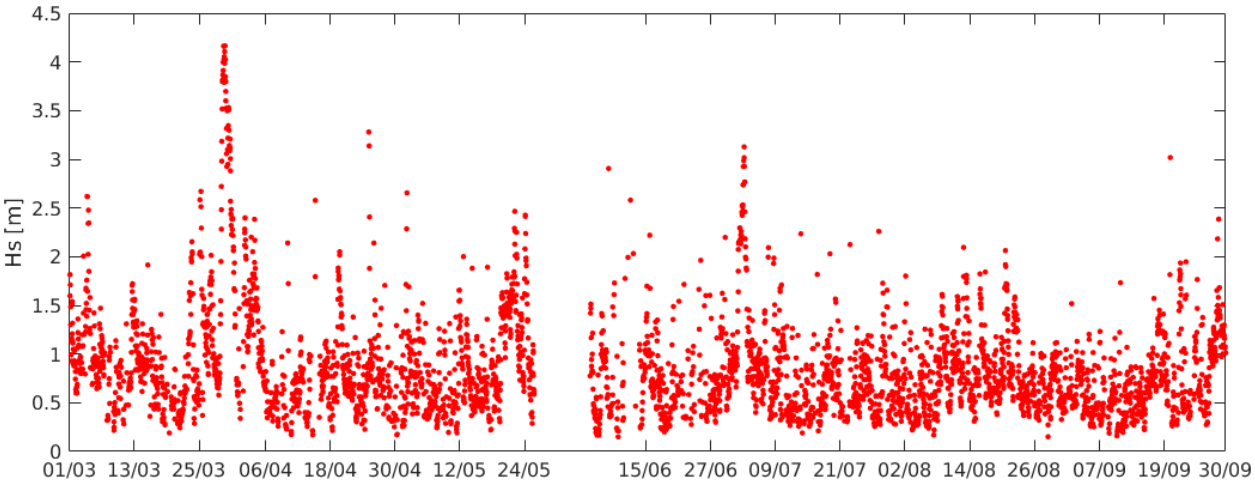

Figure 4.14: Treated HF radar data of the Alfacada antenna. Time series data are for dd/mm/2014.

4 Discussion

The synoptic situation that causes the NW wind jets at the Ebro Delta is analyzed. During the NW wind-jet event E3, a high-pressure system over the Iberian Peninsula and a low-pressure system situated in front of the Catalan coast occurred (see Figure 4.15). The synoptic situation during E1 is similar to E3, but with a wider low-pressure area with higher gradients, covering the entire NW Mediterranean. For event E2, the circumstances are almost the same as in E3, and during E4, the synoptic situation presents a high-pressure system at the Bay of Biscay and a low-pressure system centered at the Ligurian Sea. These results are consistent with previous studies. For instance, Riosalido et al. (1986) described the synoptical patterns of the mistral. They noted that when the Iberian Peninsula is affected by the southeast flank of an anticyclone, with the isobars entering through the Pyrenees from the NE, a pressure gradient is established in the Ebro Valley from NW to SE, generating a mistral wind. In addition, Riosalido et al. (1986) affirmed that it becomes stronger when cyclogenesis develops in the western Mediterranean (Gulf of Lion) or when a low persists in that area.

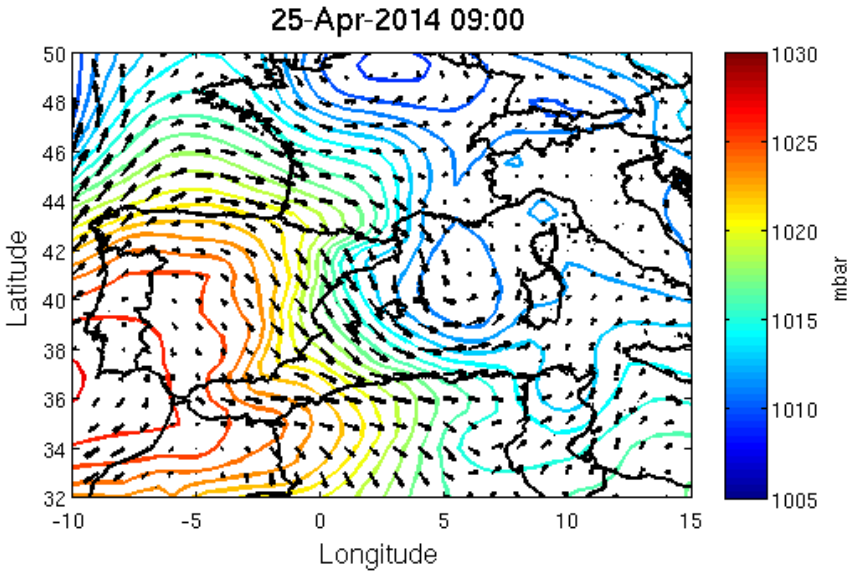

Figure 4.15: Synoptic situation on 25 April at 09:00 (i.e., during E3). This figure was created with data from the ECMWF reanalysis (`http://www.ecmwf.int`). The black arrows are the wind field at 10 m above the sea surface, and the contour plot corresponds to the sea level pressure.

All of these synoptic situations develop northerly winds at the north of the Catalan coast together with NW winds at the Ebro Delta region. The wind and wave pattern results from the second-level domain during E3 are presented in Figure 4.16. The coexistence of N and NW winds is observed, which induces a bimodal spectrum at the Ebro Delta (observed before in Figure 4.7d). Apart from the NW wind at the Ebro Delta, associated with the wind-sea system, there is an intense northerly

wind at the northern part of the coast that generates waves propagating to the south, but due to the diffraction phenomena, these waves are likely rotated to the east and can be observed at the Ebro Delta as a swell system.

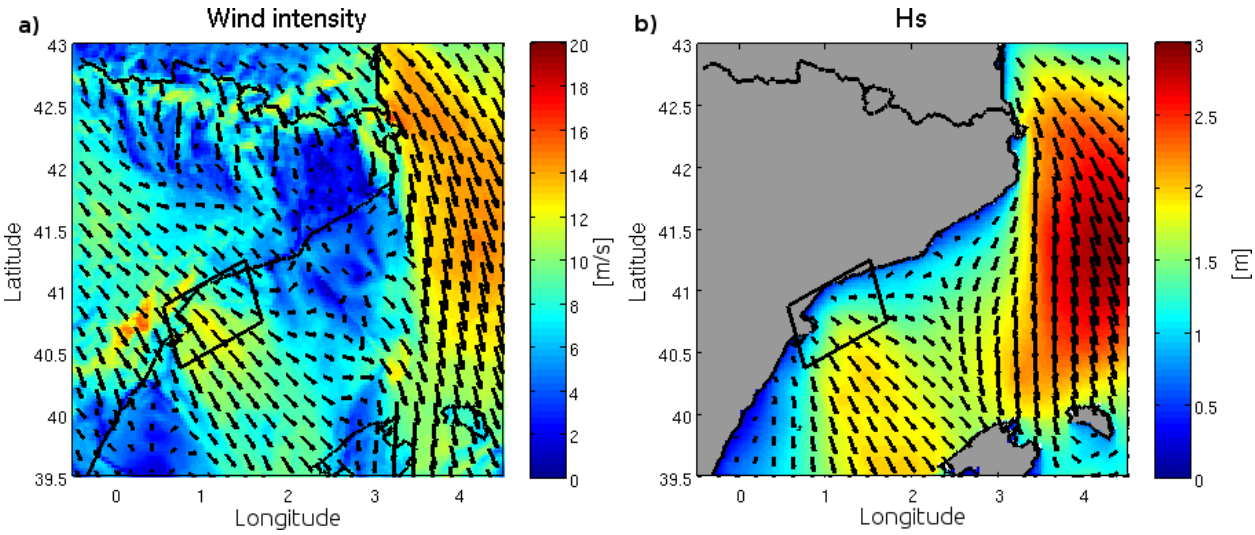

Figure 4.16: Results of the second-level domain on 25 April at 12:00. a) Wind intensity. b) Significant wave height and wave direction. The black rectangle corresponds to the local domain.

Overall, the four NW wind-jet events reported in the study period were created in similar synoptic situations and one can state that it is a frequent occurrence. For this reason, it is important to have numerical models able to forecast these events at the Ebro Delta, where a bimodal situation occurs due to the coexistence of N and NW winds.

The results described here show that a bimodal spectrum occurs at the start and the end of a wind jet and that the energy peak has more energy offshore than nearshore. Similar results were obtained by Shimada and Kawamura (2006), who found that, in wind-jet regions, the spectra show one primary peak whose direction coincides with the local wind direction and that with increasing offshore distance, the peak energy increases and the peak frequency downshifts. The work in Shimada and Kawamura (2006) also found that the overall directional spreading corresponds to the wind intensity distribution. They said that it is negatively correlated with wind energy and is small in wind-jet regions ($<40°$) and large at wake regions ($>40°$). In the present study, similar values are observed. At the wind-jet axis, the directional spreading is less than 40°, and it is higher when the measurement point is located out of the wind-jet axis and when the measurement is taken before the wind jet starts. The section evolution plots in Figures 4.8 and 4.9 show that the wave height is positively correlated with the wind intensity, but considering the y scale difference between the two magnitudes, it is observed that the wind intensity increases more than the wave height. This is consistent with Shimada and Kawamura (2006), who stated that the significant wave height fluctuations coincided with wind energy variations, but whose intensities were much smaller than those of wind energy.

Regarding the wave response to the wind turn, the results obtained at the Ebro Delta show a clear bimodal spectrum for a wind turn of the order of 90°. For instance, in Figure 4.7a–b, it can be observed that a wind turn from SSW to WNW is able to develop a bimodal spectrum. This behavior is similar to the one observed by Young et al. (1987), who performed several numerical experiments with third-generation wave models and found that for wind shifts of 90° and greater, the coupling between the old sea and the newly-generated wind waves became sufficiently weak that the wave-wave interactions were unable to suppress the development of a new high-frequency wind-sea peak in the new wind direction. Thus, a second, independent wind-sea spectrum was generated in the new wind direction, while the old wind-sea gradually decayed as swell. In contrast, Aijaz et al. (2016) found that a 180° wind turn developed a bimodal spectrum, but for a 90° wind turn, the spectrum remained unimodal and only changed to a new direction.

The analysis of the HF radar data reliability performed in Section 3.4 shows that, due to its scarcity of data, the HF radar data can be useful for undertaking climatology, where the wave height tendency could be enough, but it is not useful for studying a specific event. For instance, in Figure 4.17, the comparison between the resulting processed HF radar data at the Alfacada site and the modeled wave height at different locations within the Alfacada antenna range during the event E3 is presented. The authors note that the HF radar data are not useful for validating a short specific event. In addition, it is worth noting the differences between the modeled time series. These differences cannot be seen by the HF radar, because HF radar data represent averaged measurements over RCs of some kilometers in size and, thus, cannot measure individual waves or differentiate different behavior along an RC. In this sense, it is important to note that Long et al. (2011) found good agreement between the two datasets, but also stated that, in their study area, the wave height is only minimally variable from 3–45 km off the coast.

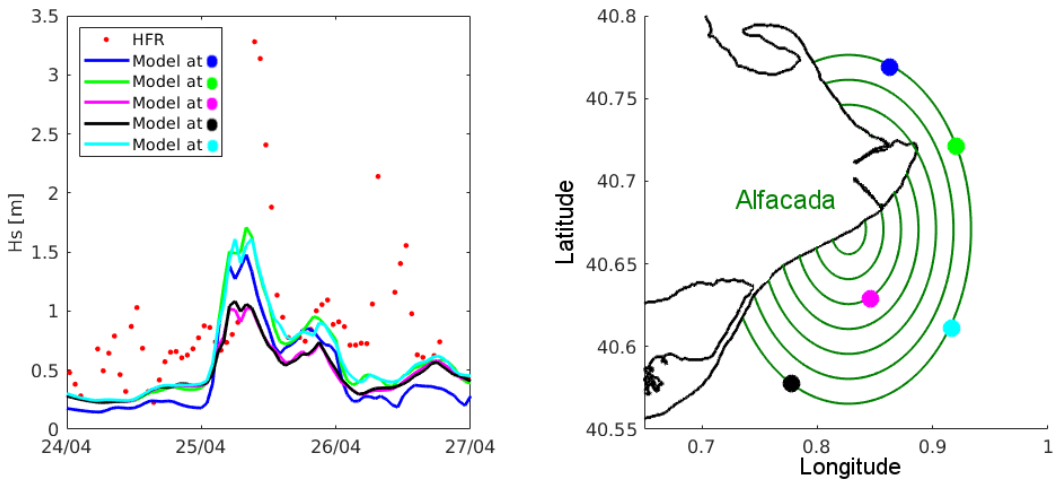

Figure 4.17: Treated HF radar data of the Alfacada antenna compared with different modeled time series from points located within the antenna range. Time series data are for 2014.

Since for young wind sea, most of the stress in the boundary layer is determined by momentum transfer from wind to waves (Janssen, 1991), an important future work to be considered could be the wave and atmosphere model coupling in order to parametrize the sea-surface roughness properly. As a matter of fact, Jorda et al. (2007) stated that the modification of the wind drag coefficient by waves appeared to be the most crucial element, especially in regions where the wind-induced dynamics have a predominant role. Another thing to consider is the implementation of sea-swell partitioning, which is now available in an updated SWAN release (end of July 2016). In this new version, the model includes wave spectral partitioning based on the watershed algorithm of Hanson and Phillips (2001). The first partition is due to wind sea, and the remaining partitions are the swell. Finally, working with the new Sentinels data could be a good way to overcome the scarcity of measured wave data in the region.

5 Conclusions

The SWAN numerical model has been implemented at the Ebro Delta, presenting good agreement with observational data. Within the study period (two months), four wind-jet events were selected to investigate the wind-wave response in terms of wave spectra, significant wave height and directional spreading. According to the model results, the wave field exhibits a noteworthy spatial and temporal variability. The significant wave height presents a positive correlation with the wind intensity and shows a spatial distribution in accordance with the wind field. In contrast, the wave directional spreading presents a negative correlation with the wind intensity, resulting in a lower wave dispersion at the wind-jet axis. There are also differences of wave directional spreading along the wind-jet axis, being higher in the nearshore zone. The model results of wave spectra show a bimodal spectrum at the start and the end of the wind jet, when a wind-sea system and a swell system coexist, and a unimodal spectrum (due to a wind-sea system) during the wind jet, with the wave direction matching with the wind direction. Bimodal spectra are very common in the region due to the synoptic conditions that induce the NW wind jets. These are usually accompanied by northerly winds at the north of the Catalan coast, which produce the swell system at the Ebro Delta.

It is worth noting that this is the first time that the spectral evolution at the Ebro Delta has been analyzed in time and space, and thus, future research including more measured data (e.g., the new Sentinels) should be considered.

Finally, the reliability of the Ebro Delta HF radar data has been also investigated. HF radar raw data cannot be used directly; they must be post-processed. In this study, different methods have been used to filter the HF raw data, and the results show that the quality of the treated HF radar data is rather good. Thus, it is a data source that must be considered in future studies. However, the HF radar time series are full of gaps and are not useful for studying the evolution of a short-duration specific event. Additionally, when using HF radar wave data, it is important to remember that HF radar samples are homogeneous along a range cell, and thus, they give an average of the wave parameters over areas of the size of the range cell range, but cannot see individual waves. Therefore, it is important to consider the wave variability of the region. If it is quite homogeneous, the HF radar data could be more representative of real conditions, but, if the region presents big wave gradients, the HF radar data could be measuring something very different than the typical buoy data to which the authors are accustomed.

Chapter V

Wave–current interactions under wind-jet conditions

"The ocean is a mighty harmonist."

William Wordsworth

The content of this chapter has been submitted in a jorunal and is currently under review:

Ràfols, L., Grifoll, M., Espino, M. (2018). Wave–Current Interactions in a Wind-jet Region.

1 Introduction

During the last decade, several water circulation models have been developed including the wind-waves induced currents. There are two different formulations to include the so-called wave effects on currents (WEC) in the three-dimensional primitive equations: by means of the radiation stress gradient (Mellor, 2011) and with the vortex force (VF) formalism (Uchiyama et al., 2010; Kumar et al., 2012). The VF formalism separates the conservative and non-conservative contributions in the momentum balance equations, which allows one to evaluate flow fields within both inner shelf and surf zone environments (Kumar et al., 2012).

From a modeling perspective, several circulation and wave models have been coupled in order to consider the wave–current interactions (WCIs). For instance, Xie et al. (2001) coupled the 3D ocean model POM with the WAM wave model and found that wind waves can significantly affect coastal ocean currents both at the surface and near the seabed. Osuna and Wolf (2005) implemented the coupling between the circulation Proudman Oceanographic Laboratory Coastal-Ocean Modeling System (POLCOMS) and the WAM model in the Irish Sea. This system was then modified by Bolaños et al. (2011), who included three-dimensional interactions following Mellor (2003, 2005) and applied the coupled model system to the Mediterranean Sea. Tang et al. (2007) implemented the WCI in a 3D ocean model (Princeton Ocean Model, POM) and a spectral wave model (WAVEWATCH III), based on Jenkins (1987) formulation, and evaluated the model by comparison with surface velocity data derived from surface drifters. McWilliams et al. (2004) developed a multi-scale asymptotic theory for the evolution and interaction of currents and surface gravity waves of finite depth, which was then implemented and extended for applications within the surf zone in the UCLA ROMS model by Uchiyama et al. (2010). Warner et al. (2008b) used the Model Coupling Toolkit (MCT) to couple the ocean circulation model Regional Ocean Model System (ROMS) and the surface wave model Simulating WAves Nearshore (SWAN) and included nearshore processes, such as radiation-stress terms based on Mellor (2003, 2005) and a surface roller model (Svendsen, 1984; Svendsen et al., 2002). This system was then further developed by Warner et al. (2010) to include one-way grid refinement in the oceanic and wave models, coupling to an atmospheric model in order to include effects of sea surface temperature and waves, and to provide interpolation mechanisms to allow the models to compute on different grids. The resulting system is known as the Coupled Ocean–Atmosphere–Wave–Sediment Transport (COAWST) modeling system. Then, Kumar et al. (2012) implemented the VF formalism into the COAWST modeling system, with some modifications to the method of Uchiyama et al. (2010).

The north Ebro Shelf (NW Mediterranean Sea) is a region characterized by northwestern (NW) winds that are channeled through the Ebro Valley and which result in cross-shelf wind jets when

they reach the sea. This region is very interesting from a meteo-oceanographic point of view because multiple processes take place, such as bimodal wave spectra and the development of a two-layer cross-shelf flow. Some authors have investigated the circulation patterns (Grifoll et al., 2015; Ràfols et al., 2017a) and the wave field (Bolaños-Sanchez et al., 2007; Grifoll et al., 2016a; Ràfols et al., 2017b) during these NW wind-jet events but less efforts have been made at investigating the WCI in the region. Due to the limited observational data, in order to study the wind-jet induced dynamics of the region, the use of numerical models is required. However, at the same time, this makes the investigation rather challenging and forces a rather qualitative analysis based on the modeled physical processes reliability. The purpose of this study is to validate the implemented coupled system and investigate the wave effects on the circulation and the current effects on the wave field at the continental shelf during a wind-jet event. With this aim, results from uncoupled models are compared with the outputs from a two-way coupled numerical model. The selected study period is from March 15 2014 to May 15 2014 because it contains four wind-jet episodes. Additionally, this period has been previously used to validate numerical models in the study region and the wind-wave characterization (Ràfols et al., 2017b), and water shelf circulation (Ràfols et al., 2017a) was investigated by combining numerical efforts and in situ observations.

This chapter is organized as follows. In Section 2 the methods used in this work are presented. The results are shown in Section 3, discerning between the effects of waves on currents and the effects of currents on waves. A discussion of the results can be found in Section 4, and the main conclusions of the work are highlighted in Section 5.

2 Methodology

2.1 Numerical Model

In this study, the COAWST modeling system is used to perform the uncoupled ROMS and SWAN model simulations and the two-ways coupling run.

Three different runs have been performed in this work (see Figure 5.1): one with the ROMS model uncoupled, one with the SWAN model uncoupled and, finally, one with the ROMS and SWAN models two-way coupled.

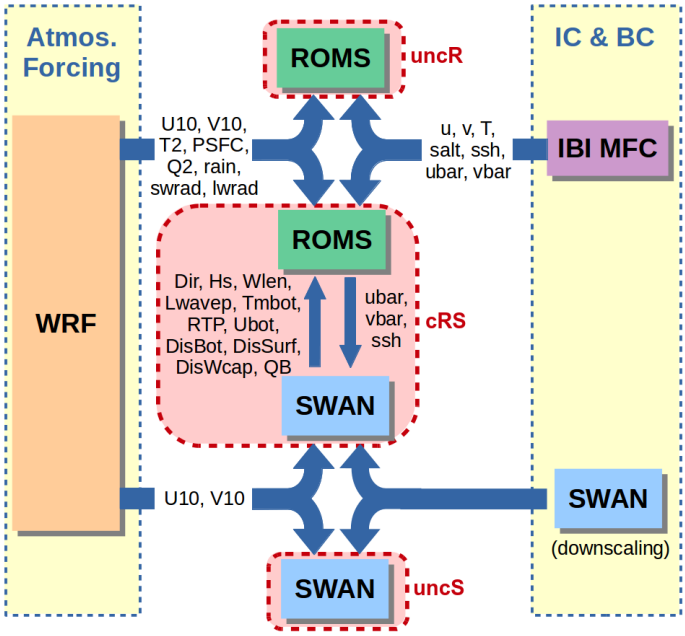

Figure 5.1: Configuration of setup run. In red, the name given to each configuration.

The numerical domain (see Figure 5.2) has a horizontal resolution of 350 m and, in the ROMS case, a vertical resolution of 20 sigma levels. The bathymetry introduced in the models has a grid resolution of 0.0083° and was obtained from General Bathymetric Chart of the Oceans (GEBCO; www.gebco.net). Both SWAN and ROMS models are forced with hourly atmospheric data from a previous WRF (Weather Research and Forecasting) model run provided by the SMC (Servei Meteorològic de Catalunya) that has a spatial resolution of 3 km.

In order to generate the boundary conditions for the SWAN model, a downscaling technique has been used. The entire system consists of three nested domains (see Figure 5.2a). The largest one covers the western Mediterranean Sea with a spatial resolution of 15 km and provides boundary conditions to a second-level domain. The latter covers the Balearic Sea with a spatial resolution of 3 km and provides boundary conditions to the smaller domain, which has a horizontal resolution of

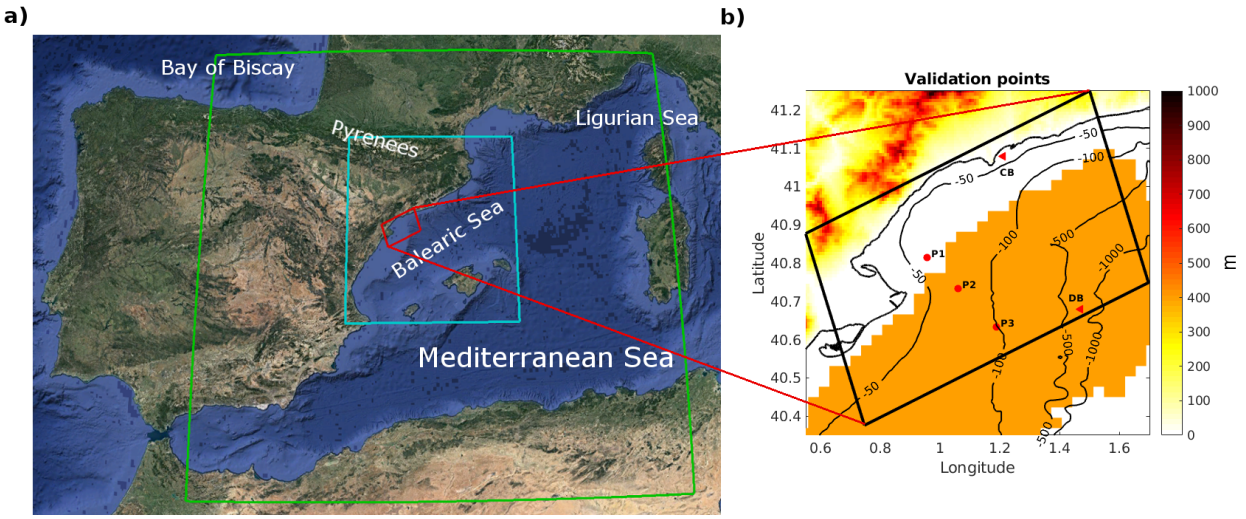

Figure 5.2: Study area. a) NW Mediterranean Sea and numerical domains: 15 km resolution domain for the SWAN model (green), 3 km resolution domain for the SWAN model (blue) and 350 m resolution coastal domain for the ROMS and SWAN models (red). b) Orography (in m), coastal domain, buoy locations (red triangles; CB and DB), points where the numerical results are examined in detail (red dots: P1, P2 and P3) and HF radar coverage area (in orange).

350 m. This study is focused on this last domain. The WRF model provided by the SMC provides the 10-m surface winds ($U10$, $V10$) forcing and the initial conditions have been obtained running the model in stationary mode.

In the SWAN model, non-stationary conditions, spherical coordinates and nautical convention have been selected. The wind growth is computed with a sum of a linear term and an exponential term. For the linear growth, the expression from Cavaleri and Malanotte-Rizzoli (1981) is used, and for the exponential growth, the expression and coefficients from Komen et al. (1984) are used. The nonlinear quadruplet wave interactions are integrated by a fully explicit computation of the nonlinear transfer with the Discrete Interaction Approximation (DIA; proposed by Hasselmann et al., 1985) per sweep (using default coefficients). For the whitecapping, the Komen et al. (1984) formulation is used with $C_{ds} = 2.36 \times 10^{-5}$, $\delta = 1$ and $p = 4$. Finally, the JONSWAP (Hasselmann et al., 1973) bottom friction formulation is added with the default coefficients. The spectrum is discretized with a constant relative frequency resolution of $\Delta f = 1.1$ (logarithmic distribution) and a constant directional resolution of $\Delta\theta = 10°$. The discrete frequencies are defined between 0.01 Hz and 1 Hz. Above the high-frequency cutoff, a diagnostic tail f^{-4} is added.

The initial and boundary conditions for the ROMS model are taken from the Iberian Biscay Irish – Monitoring and Forecasting Centre (IBI-MFC) product. This product (`http://marine.copernicus.eu/`) includes all main forcings (i.e. tidal forcing, high-frequency atmospheric forcing, fresh water river discharge, etc.) and is based on a (eddy-resolving) NEMO model application run at 1/36° horizontal resolution. The outputs provided by the IBI-MFC used in our numerical model

are 3D daily means of temperature (T), salinity ($salt$) zonal velocity (u), meridional velocity (v) and 2D (surface) hourly means of sea surface height (ssh) and barotropic currents ($ubar$, $vbar$). The WRF model provided by the SMC provides the atmospheric forcing fields for the ROMS model, which include 10 m surface winds ($U10$, $V10$), atmospheric pressure ($PSFC$), relative humidity ($Q2$), atmospheric surface temperature ($T2$), precipitation ($rain$) and shortwave ($swrad$) and longwave ($lwrad$) net heat fluxes to the ocean model. The model uses these parameters in the COARE algorithm (Fairall et al., 1996) to compute ocean surface stresses and ocean surface net heat fluxes.

The ROMS model implementation includes a generic length-scale turbulent vertical mixing scheme with the $k-\epsilon$ parametrization, a logarithmic profile for the bottom boundary layer with a bottom roughness of 0.005 m and horizontal mixing terms in geopotential surfaces. The Ebro River discharge is characterized with data from the Automatic Hydrologic Information System of the Ebro River basin (owned by the Confederación Hidrográfica del Ebro, www.chebro.es). The data used to force the numerical model consist of daily measurements of river runoff and temperature.

In the two-way coupled run, the WEC are implemented using a coupling time step of 20 min. The wave model provides wave direction (Dir), significant wave height (Hs), wave length ($Wlen$), peak wave length ($Lwavep$), surface and bottom periods (RTP, $Tmbot$), bottom orbital velocity ($Ubot$), wave energy dissipation ($DisBot$, $DisSurf$, $DisWcap$) and percent wave breaking (QB) to the ocean model. These parameters are used by the ocean model in four different mechanisms:

- To compute enhanced bottom stresses due to the effect of turbulence in the wave boundary layer by means of the SSW (Sherwood / Signell / Warner) implementation of Madsen (1994) bottom boundary layer formulation.
- To compute enhanced surface stresses (SStr) due to changes in the surface roughness z_0. In contrast to the COARE algorithm used in the uncoupled ROMS run, now the Taylor and Yelland (2001) sea surface roughness closure model, which is sea-state dependent, is used. Now the z_0 is derived from $\frac{z_0}{Hs} = 1200(Hs/Lp)^{4.5}$, where Lp is the peak wave length.
- To inject turbulent kinetic energy (TKE) at the surface due to breaking waves. It is introduced as a surface flux of turbulence kinetic energy in the generic length scale method (Warner et al., 2005).
- To include the wave forces using the VF formalism (Uchiyama et al., 2010; Kumar et al., 2012, see Section 2.3).

The wave model receives currents (u_s, v_s) and sea surface height (ssh) from the ocean model. The surface currents (u_s, v_s) were computed taking into account the vertical distribution of the current

profile using the formulation presented by Kirby and Chen (1989), which integrates the near-surface velocity over a depth controlled by the wave number. The presence of an ambient current may change the amplitude (due to a transfer of energy between the waves and currents), the frequency (due to the Doppler shift) and the direction (due to current-induced refraction) of the waves. The ocean currents also modify the wind speed forcing with $S = f(U_{wind} - u_s; V_{wind} - v_s)$ and the wave celerity using the modified group velocities $c_x = c_{gx} + u_s$, $c_y = c_{gy} + v_s$, which in turn affects the wave number.

2.2 Observations

For validation purposes, data from the Tarragona Coast buoy, the Tarragona deep-water buoy and the HF radar are used (see Sections 2.3 and 2.4 in Chapter II). The locations are shown in Figure 5.2, jointly with the bathymetry and the numerical domains.

The HF radar provides hourly measurements of the current velocities in the top meter of the water column with a horizontal resolution of 3 km and a cut-off filter of 100 cm/s. The coastal wave buoy (CB) is a Triaxys buoy that provides significant wave height, peak period, nautical direction and directional wave spectra, among other data. The deep-water buoy (DB), an ocean Seawatch buoy, measures water velocity and water temperature at the sub-surface (nominal depth of 3 m), wind vectors at 3 m above the sea surface, significant wave height, peak period, nautical direction and directional wave spectra, among other parameters. In order to be able to compare the measured wind data at 3 m height with the modeled data at 10 m height, the modeled data have been extrapolated from 10 m to 3 m using a logarithmic profile.

2.3 Momentum balance description

The cross-shelf momentum balance is used to analyze the wave effects on the circulation over the continental shelf. The simplified equations for the VF approach can be obtained after removing the curvilinear terms, body forces and horizontal and vertical mixing, and then using Cartesian coordinates (Kumar, 2013):

$$\underbrace{\frac{\partial D\overline{v}}{\partial t}}_{\text{ACC}} + \left[\underbrace{\overline{\frac{\partial}{\partial x}(uv) + \frac{\partial}{\partial y}(vv) + v\left(\frac{\partial u^{st}}{\partial x} + \frac{\partial v^{st}}{\partial y}\right)}}_{\text{HA}} - \underbrace{\overline{u^{st}\left(\frac{\partial v}{\partial x} - \frac{\partial u}{\partial y}\right)}}_{\text{HVF}} \right] + \tag{5.1}$$

$$\underbrace{fD\overline{u}}_{\text{COR}} + \underbrace{fD\overline{u^{st}}}_{\text{StCOR}} = \underbrace{-D\left.\frac{\partial \overline{\varphi^c}}{\partial y}\right|_z}_{\text{PG}} + \underbrace{D\overline{F^{wy}}}_{\text{WF}} + \underbrace{\tau_s^y}_{\text{SStr}} - \underbrace{\tau_b^y}_{\text{BStr}}$$

where D is the total water depth, f is the Coriolis parameter, the overbar indicates depth-averaged values, u and v are the three-dimensional Eulerian mean velocities, u^{st} and v^{st} are the three-dimensional Stokes velocities, $\overline{\varphi^c}$ is the vertically integrated geopotential function, τ_s^y and τ_b^y are the surface and bottom stress, respectively, and $\overline{F^{wy}}$ is the vertically integrated non-conservative wave forcing. Going from left to right, the terms in the equations are local acceleration (ACC), horizontal advection (HA), horizontal vortex force (HVF), Coriolis (COR), Stokes–Coriolis ($StCOR$), pressure gradient (PG), non-conservative wave forces (WF), surface stress ($SStr$) and bottom stress ($BStr$). The terms in blue are the wave-induced terms.

The pressure gradient term includes (Kumar et al., 2012) the Eulerian non-WEC contribution (P^c) and the WEC contribution (P^{WEC}), which can be decomposed in a quasi-static response (P^{qs}), a Bernoulli head (P^{bh}) and a surface pressure boundary correction (P^{pc}):

$$\nabla\varphi = P^c + P^{WEC} = P^c + P^{qs} + P^{bh} + P^{pc} \tag{5.2}$$

The non-conservative wave forcing term F^{wy} includes accelerations due to (Kumar et al., 2012): bottom streaming (B^{bf}), surface streaming (B^{sf}) and wave breaking (B^{wb}). The latter is further decomposed in whitecapping induced acceleration (B^{wcap}), bathymetry induced breaking and acceleration (B^b) and wave rollers and rollers acceleration (B^r):

$$F^{wy} = B^{bf} + B^{sf} + B^{wb} = B^{bf} + B^{sf} + B^{wcap} + B^b + B^r \tag{5.3}$$

3 Results

3.1 Numerical model skill assessment

The ROMS and SWAN models for the same study period and the same model configurations have been validated thoroughly in previous studies (Ràfols et al., 2017a,b). The aim of this section is to analyze the skill of the coupled run in comparison to the uncoupled runs.

The first step in the numerical skill assessment is to examine the quality of the wind field, which is used to force the numerical models. Table 5.1 shows the bias, RMSD, r and d obtained from the comparison between the DB measured data and the wind field provided by the SMC. And Figure 5.3 presents the time series for the modeled and measured wind intensity at DB. The comparison shows a slight underestimation of the wind intensity but the main underestimation does not correspond to the NW wind events, which are the focus of this study. During the study period, four NW wind-jet events have been selected (see the red boxes in Figure 5.3). These events were previously analyzed in Chapter IV, where statistical metrics for each episode were provided. To see the temporal evolution of a wind jet more clearly, in Figure 5.4a the time series during the wind-jet event E3 are presented, which is the event that spans more in space and thus can be observed in the DB location. Overall, the modeled wind during the wind-jet events is less underestimated and the wind-jet temporal evolutions are properly reproduced.

Table 5.1: Statistics comparing the wind and the modeled wave parameters with the DB data.

		bias	RMSD	r	d
Wind		-0.04 m/s	1.83 m/s	0.83	0.89
Hs	*uncS*	-0.25 m	0.38 m	0.89	0.86
	cRS	-0.28 m	0.40 m	0.90	0.85
Tm_{02}	*uncS*	-0.95 s	1.09 s	0.79	0.67
	cRS	-0.34 s	0.52 s	0.85	0.86
Dir	*uncS*	-9.39°	34.89°	0.84	–
	cRS	-10.34°	36.37°	0.84	–

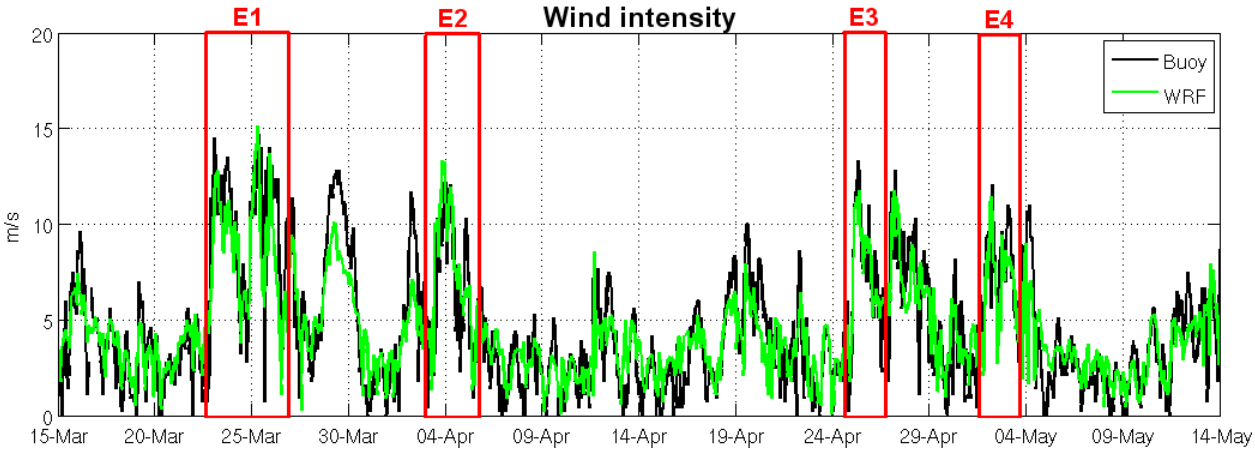

Figure 5.3: (a) Comparison between the wind measured by the DB buoy (black) and the one modeled by the WRF model and used as input for the SWAN and ROMS models (green). See statistics in Table 5.1. The red boxes are the four wind-jet events.

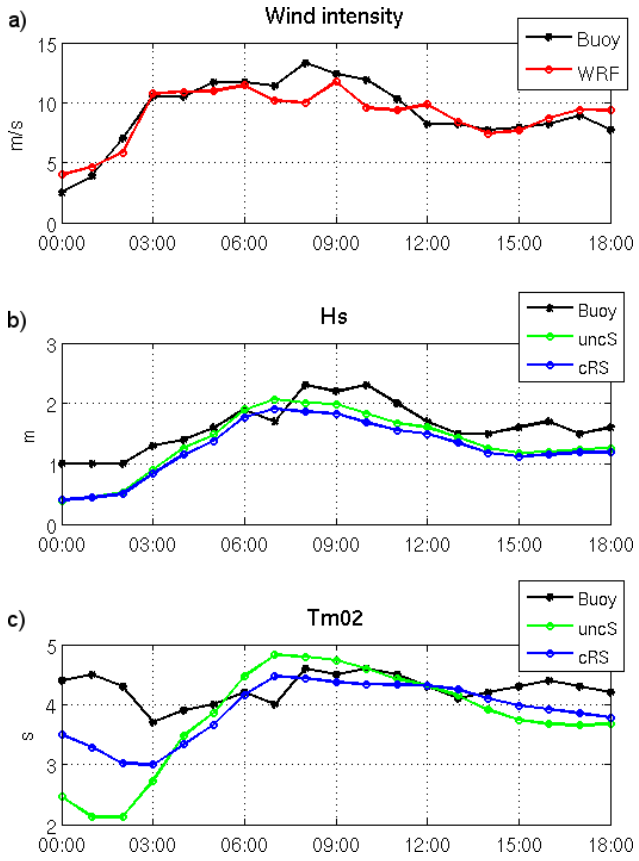

Figure 5.4: a) Wind intensity, b) Hs and c) Tm_{02} time series at DB during the wind-jet event E3 (25 April 2014). In black, the measured data, in red the WRF model data, in green the *uncS* run results and in blue the *cRS* run results.

Table 5.1 shows also the statistics obtained from the comparison of the measured wave parameters at DB and the modeled ones. The Hs and Tm_{02} time series at DB during the wind-jet event E3 are shown in Figures 5.4b and 5.4c, respectively. In general, the Hs does not show relevant differences between the *uncS* run and the *cRS* run results. It is important to note the negative bias, which

indicates that the Hs parameter is slightly underestimated. This is a clear consequence of the previously mentioned underestimation of the wind. In contrast, Tm_{02} shows a clear improvement when the models are coupled. The mean wave period Tm_{02} is defined as follows:

$$Tm_{02} = 2\pi \left(\frac{\int\int \omega^2 E(\omega,\theta) d\omega d\theta}{\int\int E(\omega,\theta) d\omega d\theta} \right)^{-1/2} \tag{5.4}$$

where $E(\omega,\theta)$ is the variance density and ω is the absolute radian frequency. The latter is determined by the Doppler shift phenomenon with $\omega = \sigma + \mathbf{k}\cdot\mathbf{U}$, where σ is the relative radian frequency (i.e. as observed in a frame of reference moving with the current velocity), $\mathbf{k}$ the wave number vector and $\mathbf{U}$ the current vector. In absence of currents, the relative radian frequency equals the absolute radian frequency. It is important to note that the buoy measures at a fixed location (i.e. in an absolute frame) and, for this reason, the comparison of the measured period with the modeled one is more realistic when the results from the *cRS* run are used (i.e. the absolute period) instead of the results from the *uncR* run (i.e. the relative period). Therefore, the differences found in the Tm_{02} parameter might be explained by the differences in frequency due to the Doppler shift phenomena that are included in the wave model when the models are coupled.

Table 5.2, where the modeled data are compared with measurements from CB, show similar results to Table 5.1. The most noticeable difference between the two tables is the *Dir* parameter, which shows better agreement in the DB case. The comparison at DB shows very good results with high correlations and no relevant differences between the *uncS* and *cRS* runs. In contrast, at CB location, the agreement with observations is lower but a clear improvement of the results is obtained when the currents are considered (i.e. with the *cRS* run).

Table 5.2: Statistics comparing the modeled wave parameters with the CB data.

		bias	RMSD	r	d
Hs	*uncS*	-0.14 m	0.23 m	0.87	0.79
	cRS	-0.17 m	0.24 m	0.89	0.79
Tm_{02}	*uncS*	-1.24 s	1.43 s	0.42	0.48
	cRS	-0.34 s	0.64 s	0.71	0.79
Dir	*uncS*	4.11°	33.06°	0.46	–
	cRS	-0.99°	25.97°	0.52	–

In Table 5.3, the modeled water currents are compared with the HF radar surface current measurements. The metrics presented in the table correspond to point P3 and show good agreement, with skill metrics that are in accordance with values found in previous work when comparing HF radar data with modeled data (Port et al., 2011; O'Donncha et al., 2015; Lorente et al., 2016b). Comparing the results from the *uncR* run with the results from the *cRS* run, some differences are observed (e.g. a decrease of the bias is obtained in the cross-shelf velocity component when the models are coupled), but the differences are not relevant enough to discern if one configuration agrees better than the other. A similar conclusion can be reached analyzing the scatter plots (not shown) comparing the HF radar data with the modeled data at P3. The differences between the *cRS* and *uncR* runs are not relevant, but the modeled cross-shelf components show a better fit with the measurements, with regression slopes of 1.01 for both runs, than the along-shelf components, with regression slopes of 0.64 and 0.68, respectively. In general, the modeled water currents show larger intensities than the measured ones.

Table 5.3: Statistics comparing the modeled water currents at P3 with data from the HF radar.

		bias	RMSD	r	d
u	*uncS*	-4.20 cm/s	14.02 cm/s	0.56	0.73
	cRS	-1.49 cm/s	13.71 cm/s	0.55	0.74
v	*uncS*	3.50 cm/s	14.18 cm/s	0.65	0.77
	cRS	2.88 cm/s	14.86 cm/s	0.66	0.77

3.2 Description of the wave effects on currents

In Figure 5.5, the HF radar water surface current time series during the wind-jet event E3 at P1 (73.7 m depth) and P3 (98.9 m depth) are compared with the *uncR* and the *cRS* run results. The figure also shows the wind intensity evolution at each point and the Hs comparison between the *uncS* and *cRS* run results. The wind-jet event E3 starts on 25 April at 02:00 (UTC), forms very quickly, reaches its maximum intensity at 06:00 and fades gradually. The water current time series show that during the wind jet peak, there is a negative increase of the cross-shelf current component (i.e., offshoreward) and a decrease of the along-shelf current. Then, after the wind-jet peak, the along-shelf component becomes more negative (i.e., southwestward). Comparing the results from the *uncR* and *cRS* runs, it is observed that higher differences occur at the shallowest point (P1), with differences up to 20 cm/s, while at P3 both runs present very similar results. No measured data are available for P1, thus it cannot be discerned which run best fits the observation. In

contrast, at P3, the modeled results can be compared with the HF radar data but it is difficult to state which simulation best reproduces the observations. The influence of waves at the cross-shelf circulation is limited and the surface circulation of both runs presents similar patterns.

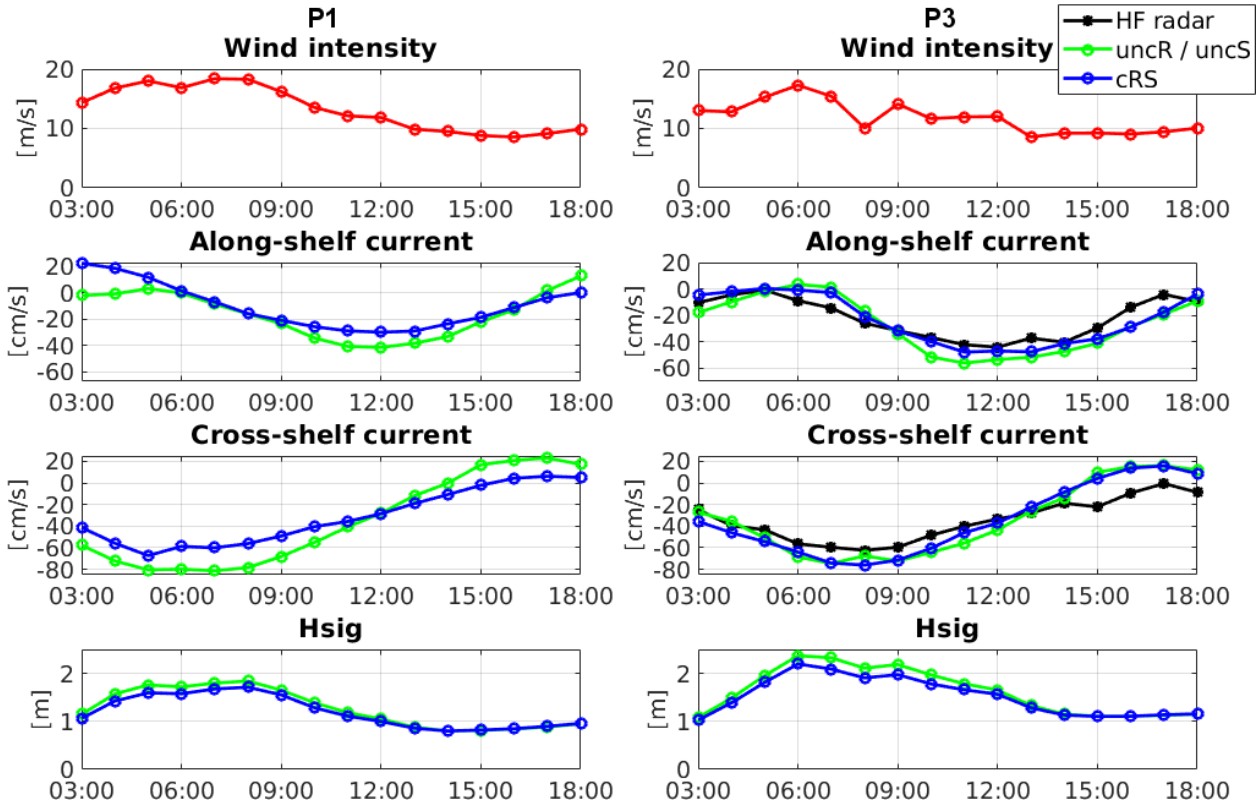

Figure 5.5: Wind intensity, along- and cross-shelf surface currents and Hs time series at P1 and P3 during the wind-jet event E3 (25 April 2014). Negative values mean offshore and southwestwards. In red, the modeled wind intensity, in black the HF radar data, in green the *uncR* and *uncS* runs results and in blue the *cRS* run results.

With the aim of visualizing the differences in the current patterns and the spatial variability between the different runs, in Figure 5.6 the measured HF radar currents are compared with the surface currents obtained with the *uncR* and *cRS* runs in four snapshots, which correspond to the evolution of the wind-jet event E3. For clarity, the figure presents the results up to the mid-slope. The modeled water currents are more intense than the water currents measured by the HF radar but the circulation patterns are consistent. There are slight differences between the *uncR* run results and the *cRS* run results. An increase of the current intensity is observed at the start of the wind jet when the waves are considered in the ROMS model (Figure 5.6c second column). In addition, the region affected by the wind jet seems to be expanded to the northeast, resulting in higher water currents in the *cRS* run. Nevertheless, the main current pattern obtained with both runs are very similar and coincide with the behavior presented in Chapter III.

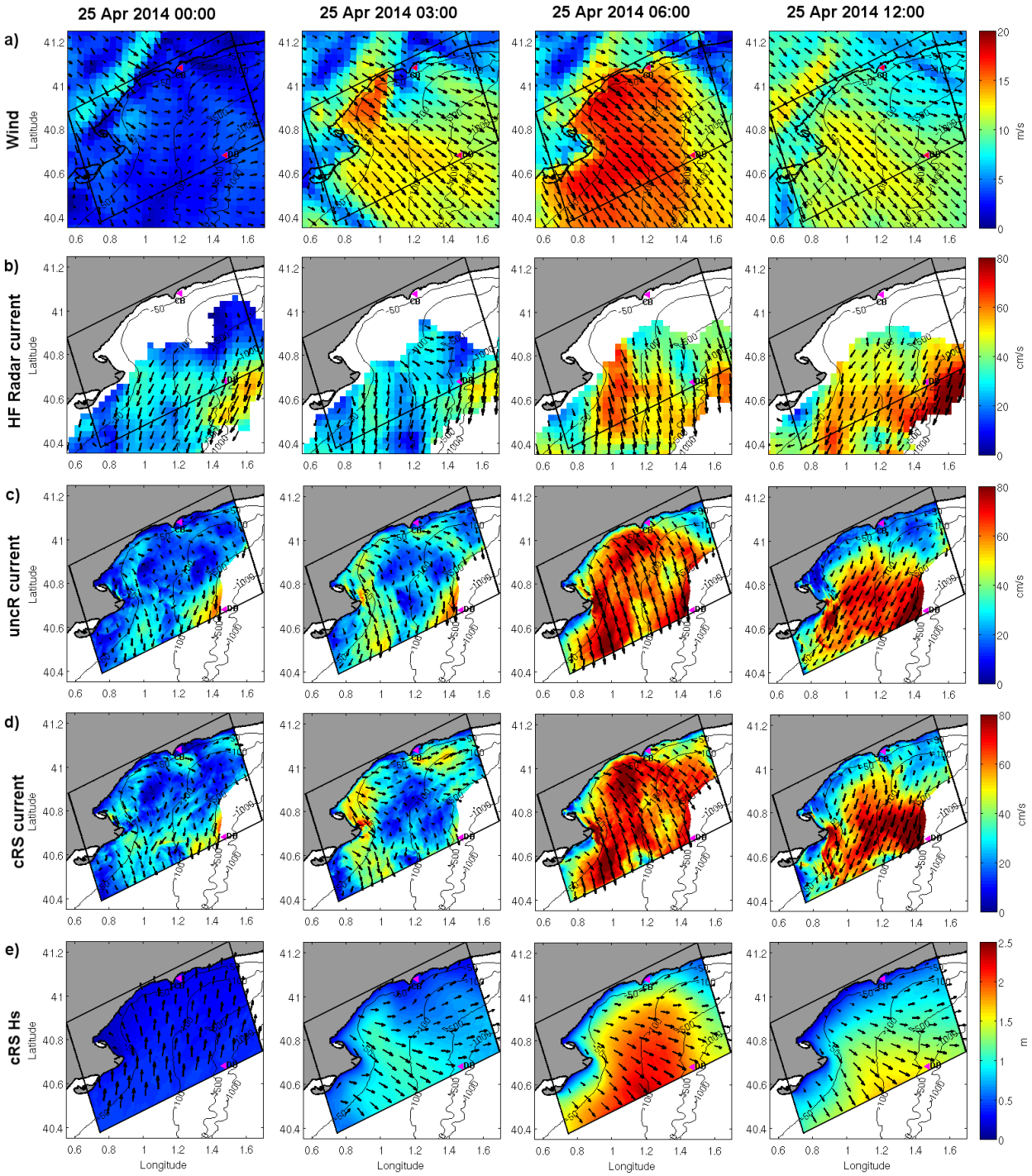

Figure 5.6: Results for the wind-jet event E3. (a) 10-m wind intensity; (b) HFR current intensity; (c) *uncR*-modeled current intensity; (d) *cRS*-modeled current intensity; (e) *cRS*-modeled Hs and mean wave direction. For clarity, the results are shown up to the mid-slope. The CB and DB locations are shown with pink triangles.

Figure 5.7 shows the Hs and water current mean differences considering: the whole study period, the whole study period except the wind-jet events and just the four wind-jet events. It is observed that the major differences are obtained during the wind-jet events. The mean differences obtained for the whole period are very similar to the mean differences under no wind-jet conditions, with differences lower than ±5 cm/s. During wind-jet conditions, a clear decrease of the water current intensity is observed at the wind-jet axis when the waves are considered, but the differences are

lower than 10 cm/s. In contrast, at shallow regions, the water current intensities are increased, showing differences up to 15 – 20 cm/s. An increase of the current intensity is also observed at the northeast corner of the domain but there the differences are just around 5 cm/s.

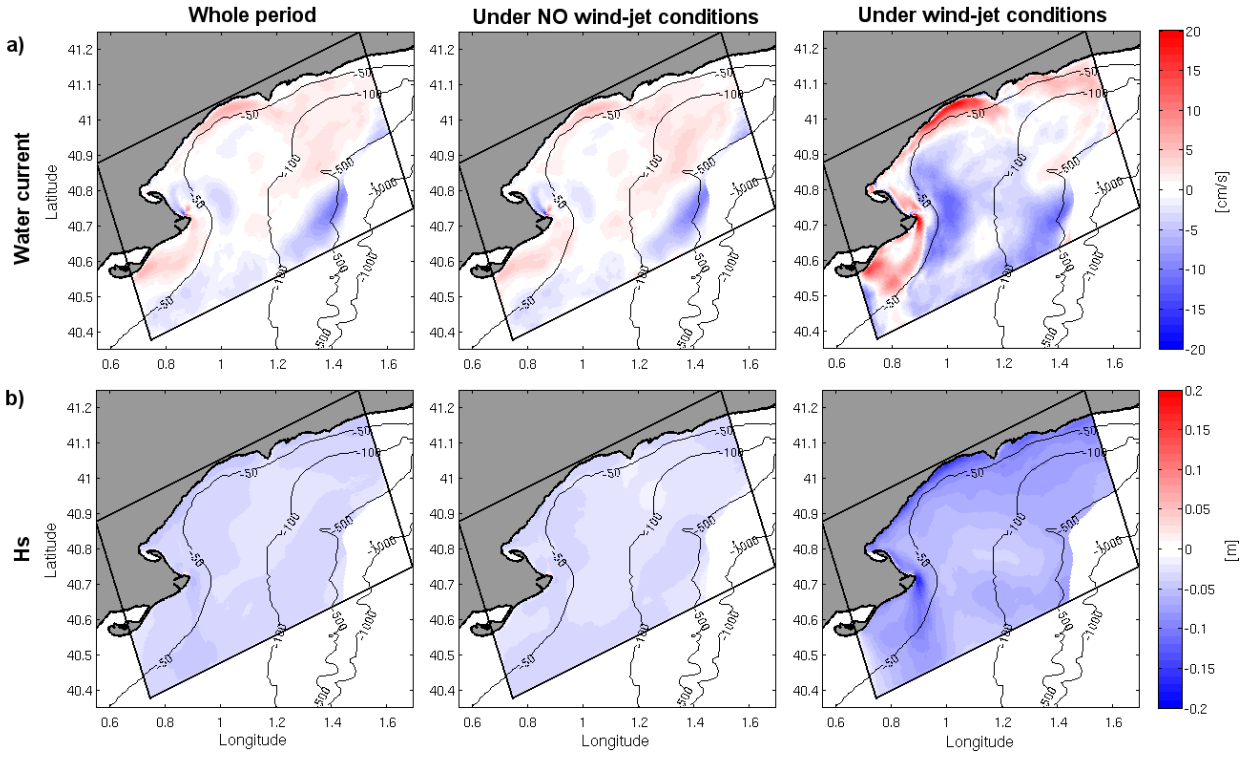

Figure 5.7: a) Water current and b) Hs mean differences between the $uncS/uncR$ run and the cRS run considering the whole period (left), the whole period except the wind-jet events (centre) and during the four wind-jet events (right).

The evolution of the buoyancy or Brunt–Väisälä frequency ($N = \sqrt{-\frac{g}{\rho_0}\frac{\partial \rho(z)}{\partial z}}$, where ρ_0 is the reference density and g is the gravitational acceleration) is investigated in order to analyze the differences between the $uncR$ and the cRS run results in the water column structure. Figure 5.8 shows the Brunt–Väisälä frequency evolution (before and after the wind jet) at P3 during the four wind-jet events for both $uncR$ and cRS runs. It is observed that the vertical structure of the water column is significantly different when the waves are taken into account. The cRS run always presents a less stratified water column, both before and after the wind jet. When a wind jet occurs, the expected behavior is that the water column will become less stratified after the wind jet than before it. This is observed in all the studied wind-jet events but the surface mixed-layer depth (SML; i.e. the distance from the surface until the top of the pycnocline) after the wind jet obtained with the cRS run is larger (i.e. deeper) than the one obtained by the $uncR$ run. Thus, the vertical mixing is significantly enhanced when the waves are taken into account.

Analyzing the results from $uncR$ and cRS runs, it is found that there is a clear enhancement of the TKE when the waves are considered, also with some increase of the SStr (see Figure 5.9). Note that the SStr felt by the ocean is equal to the air-side stress, which in the cRS run include the

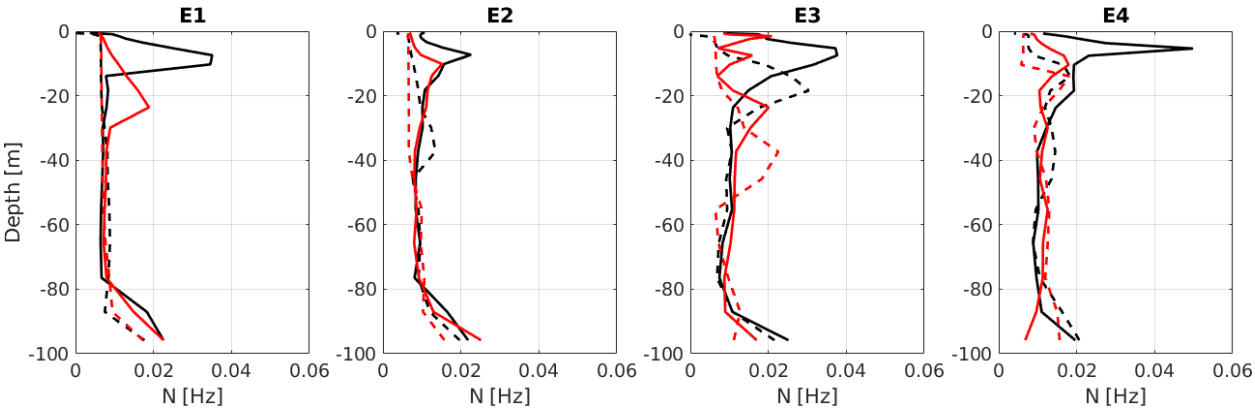

Figure 5.8: Comparison of the Brunt–Väisälä frequency at the start (solid line) and the end (dashed line) of each wind-jet event obtained from the results of the *uncR* (in black) and *cRS* run (in red) at P3.

wave-dependent sea surface roughness, but it does not account for the stress acting on waves and the dissipation due to wave breaking. The mean TKE and SStr values obtained with the model during the wind-jet event E3 at P3 shift from 8.14×10^{-4} m^2/s^2 and 0.25 N/m^2 with the *uncR* run to 5.13×10^{-3} m^2/s^2 and 0.31 N/m^2 with the *cRS* run. Additionally, the TKE and SStr peak coincide with the wind jet peak (25 April at 06:00) and the peak values found at P3 are 2.44×10^{-3} m^2/s^2 and 0.75 N/m^2 for the *uncR* run and 1.11×10^{-2} m^2/s^2 and 0.88 N/m^2 for the *cRS* run. Thus, the TKE is 1 order of magnitude higher when the waves are considered, which leads to an enhancement of the water column mixing and thus a decrease of the stratification.

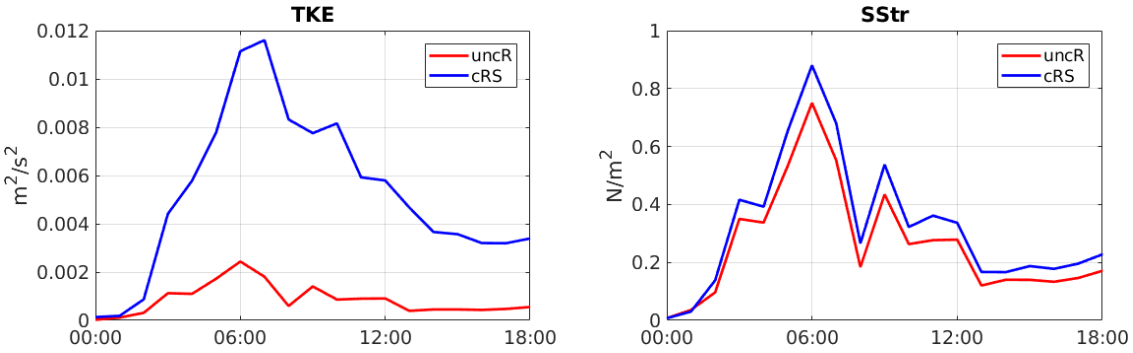

Figure 5.9: Time series comparison of the TKE (left) and SStr (right) obtained from the results of the *uncR* (in red) and *cRS* run (in blue) at P3 during the wind-jet event E3 (25 April 2014).

In order to evaluate how the waves' effects are taken into account in the momentum balance, the terms of equation 5.2 are analyzed. During a calm period before the wind jet, the cross-shelf momentum balance is between the *PG* and *COR* terms, and the remaining terms are (at least) 1 order of magnitude smaller. Thus, the wave effects on the momentum balance are negligible. In contrast, during a wind-jet event, more terms are involved in the cross-shelf momentum balance. From the coastline until 4 km offshore (∼50 m depth), the *WF* term (1.85×10^{-5} m/s^2) is on the same order of magnitude as the *PG* (2.42x10^{-5} m/s^2), *SStr* (2.73×10^{-5} m/s^2) and *HA* (1.99×10^{-5} m/s^2) terms. From that point until tens of kilometers offshore the *PG* (1.34×10^{-5} m/s^2) term is mainly balanced

by the *SStr* (1.07×10^{-5} m/s^2) and *WF* (5.05×10^{-6} m/s^2) terms, also including some contribution from the *COR* and *HA* terms. However, the *WF* term weight is half the weight of the *SStr* term. Thus, the *WF* term included by the VF formalism plays an important role in the momentum balance in the first kilometers offshore (i.e. in coastal regions). Analyzing the *WF* term, it is found that its main contributor is the surface streaming (B^{sf}; 1.65×10^{-5} m/s^2 and 3.94×10^{-6} m/s^2 for shallow and deep water, respectively), especially in shallow waters, with also some contribution of the wave breaking term (B^b; 2.01×10^{-6} m/s^2 and 1.11×10^{-6} m/s^2,respectively). Regarding the *PG* term, its weight is mainly due to the non-WEC contributions (P^c; 1.60×10^{-5} m/s^2 and 1.37×10^{-5} m/s^2, respectively) together with some contribution of the quasi-static response (P^{qs}; 1.37×10^{-5} m/s^2 and 3.21×10^{-6} m/s^2).

3.3 Description of the water current effects on waves

The irregular nature of wind causes irregular wind waves of different heights, periods and directions. For this reason, wind waves are usually described using spectral techniques, where the random motion of the sea surface is treated as a summation of harmonic wave components. In Figure 5.10 the wave response during a wind-jet event is analyzed in terms of the variance density spectrum $E(f,\theta)$ evolution obtained from the numerical model. The one- and two-dimensional frequency–direction spectra evolution at P2 (i.e. at the wind-jet axis) obtained with the *uncS* and *cRS* runs during the wind-jet event E3 are compared. The runs show similar spectra evolution patterns. When the wind jet starts, the wave field is adapted to the new wind, generating a bimodal spectrum with a wider peak at the NW (which is consistent with the new wind direction, i.e., it is a new sea system) and a peak at the south corresponding to the "old" sea system. At the peak of the wind jet, the spectra are dominated by the sea system and, when the wind-jet intensity diminishes, a new sea system occurs, while the energy due to the wind jet decrease gradually. In addition, a swell system appears at the northeast, due to the coexistence of NW wind at the region and northerly wind at the northern part of the coast (see Chapter IV). The main difference between the *uncS* and *cRS* runs is that the spectra obtained with the *cRS* run present less energy at the peak than the *uncS* run. An energy increase at higher frequencies (i.e. at the spectrum tail) can also be observed when the currents are considered, but overall the *uncS* run presents more energy. A less energetic spectrum means lower Hs values, which is consistent with the values obtained from the numerical results.

In Figures 5.5 and 5.6, it is observed that, during the wind-jet event, the wave field responds directly to the wind. In Figure 5.6, the 2D Hs maps show a clear increase of the wave height at the wind-jet axis that, at the wind-jet peak, reaches values up to 2.43 m. The time series presented

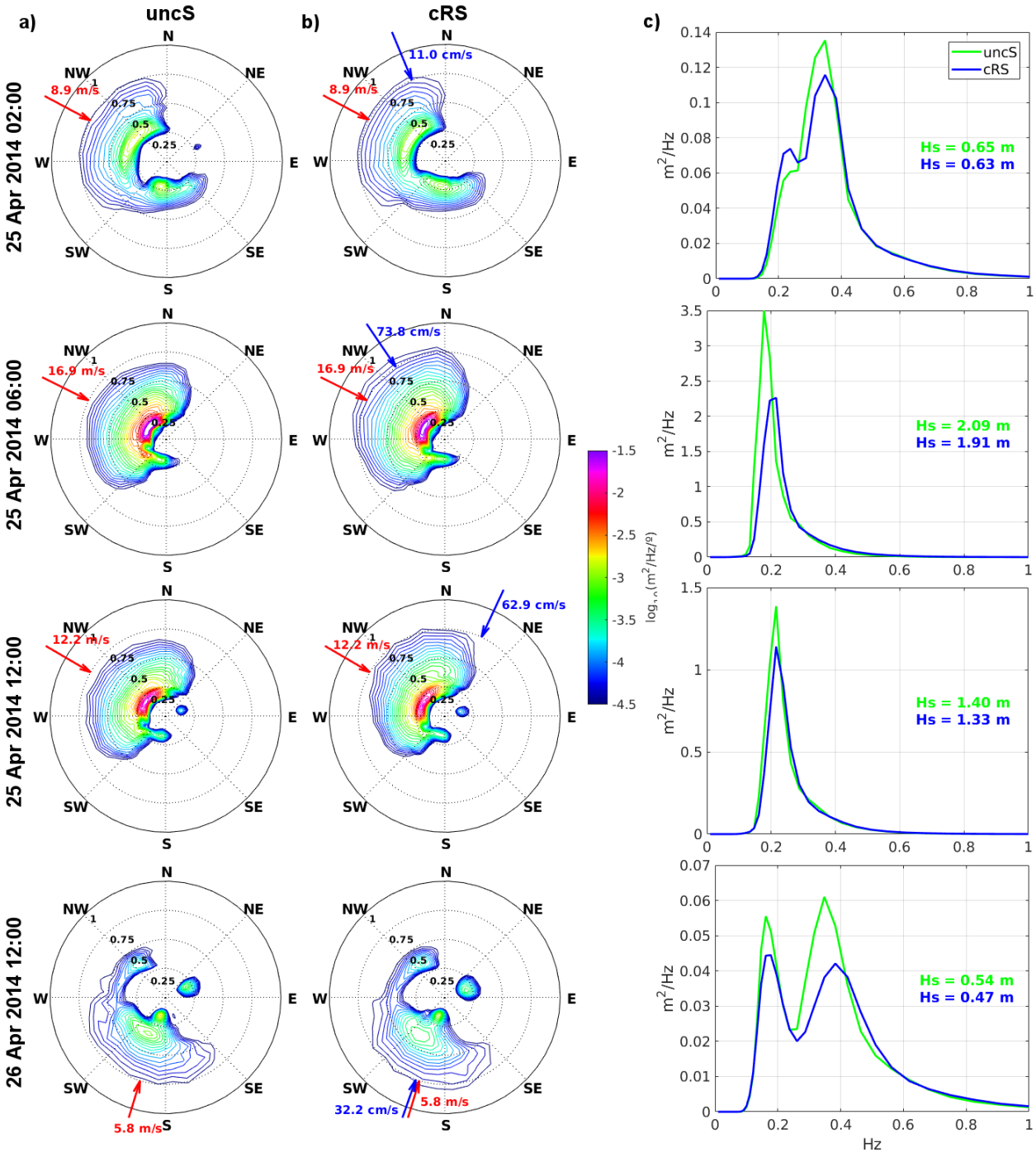

Figure 5.10: Spectra evolution during event E3 at P2. a) 2D spectrum from *uncS* run. b) 2D spectrum from *cRS* run. c) 1D spectra from both runs and the corresponding Hs values. The arrows shown in a) and b) indicate the direction and magnitude of wind (red) and current (blue).

in Figures 5.4 and 5.5 show that the Hs diminish when the water currents are considered and that the major differences (∼15–20 cm) occur during the wind-jet peak. Similar results are shown in Figure 5.7, where the mean differences show that the Hs from the *cRS* run tend to be lower than the Hs from the *uncS* run and that the major differences are observed during the wind-jet events. Under such conditions, the mean differences at shallow regions reach values of 15 cm, while the mean difference at the wind-jet axis is around 6 cm. Comparing the results from the *cRS* and the

uncS runs, it is found that considering the water currents produces a mean effect of 11% in the Hs parameter at CB location and a mean effect of 4% at DB location.

In order to analyze the Hs differences obtained with the two runs, Figure 5.11 shows the differences in Hs at P2, distinguishing the differences in the wave and current propagation directions. It is found that the Hs from the *cRS* run tends to be lower (higher) than the Hs from the *uncS* run when the difference between the propagation direction of waves and currents is lower (higher). This is to say that including the current effects on waves results in a decrease (increase) of Hs when the waves and the currents propagate in the same (opposite) direction. In general, the Hs differences between the runs are small ($\Delta Hs < 5$ cm). However, during the NW wind jets these differences increase up to 10–14 cm and, in the case of event E3, reach 20 cm. The mean differences observed at this point correspond to 10% of Hs.

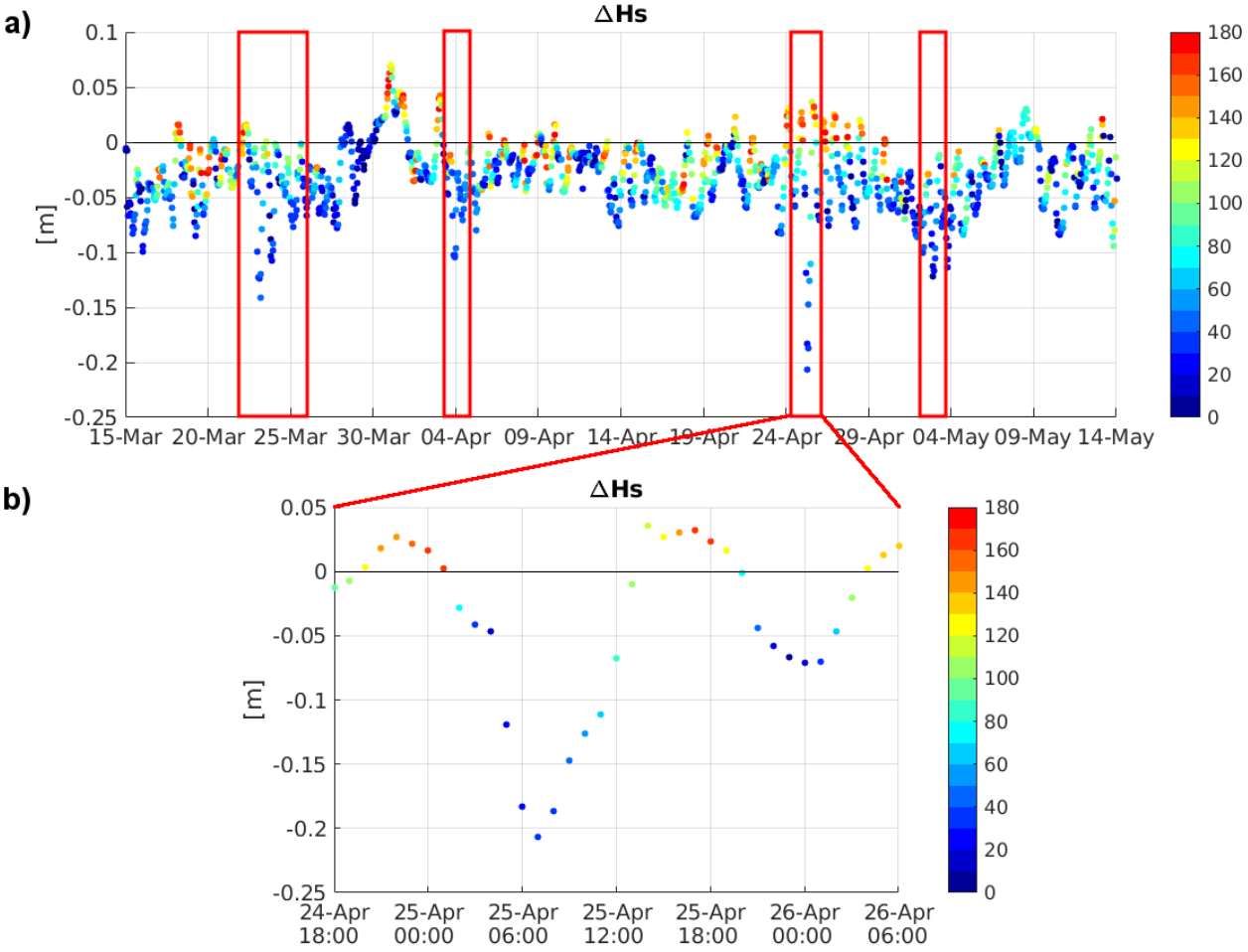

Figure 5.11: (a) Hs differences at P2. The different colors correspond to the angle between the directions of wave and current propagation. (b) Detailed view of the period corresponding to event E3.

The Tm_{02} obtained with the *cRS* tends to be higher than the one obtained with the *uncS* exceptuating the wind-jet event periods, where the Tm_{02} from the coupled run is lower (see Figure 5.4). This is consistent with the frequency increase in the *cRS* run detected in the spectra analysis during the wind-jet event E3. Figure 5.12 shows the Tm_{02} and Dir time series obtained with the *uncS*

and the *cRS* runs compared to the CB measured data. Note that the CB location is not affected by the wind jet. Qualitatively, the *cRS* run shows a clear improvement in the agreement of the Tm_{02} results with the measurements, which is consistent with the statistical parameters collected in Tables 5.1 and 5.2. Comparing the results from the *cRS* and the *uncS* runs, it is found that considering the water currents produces an average effect of 48% in the Tm_{02} parameter at the CB location. This effect is reduced to 27% at the DB location.

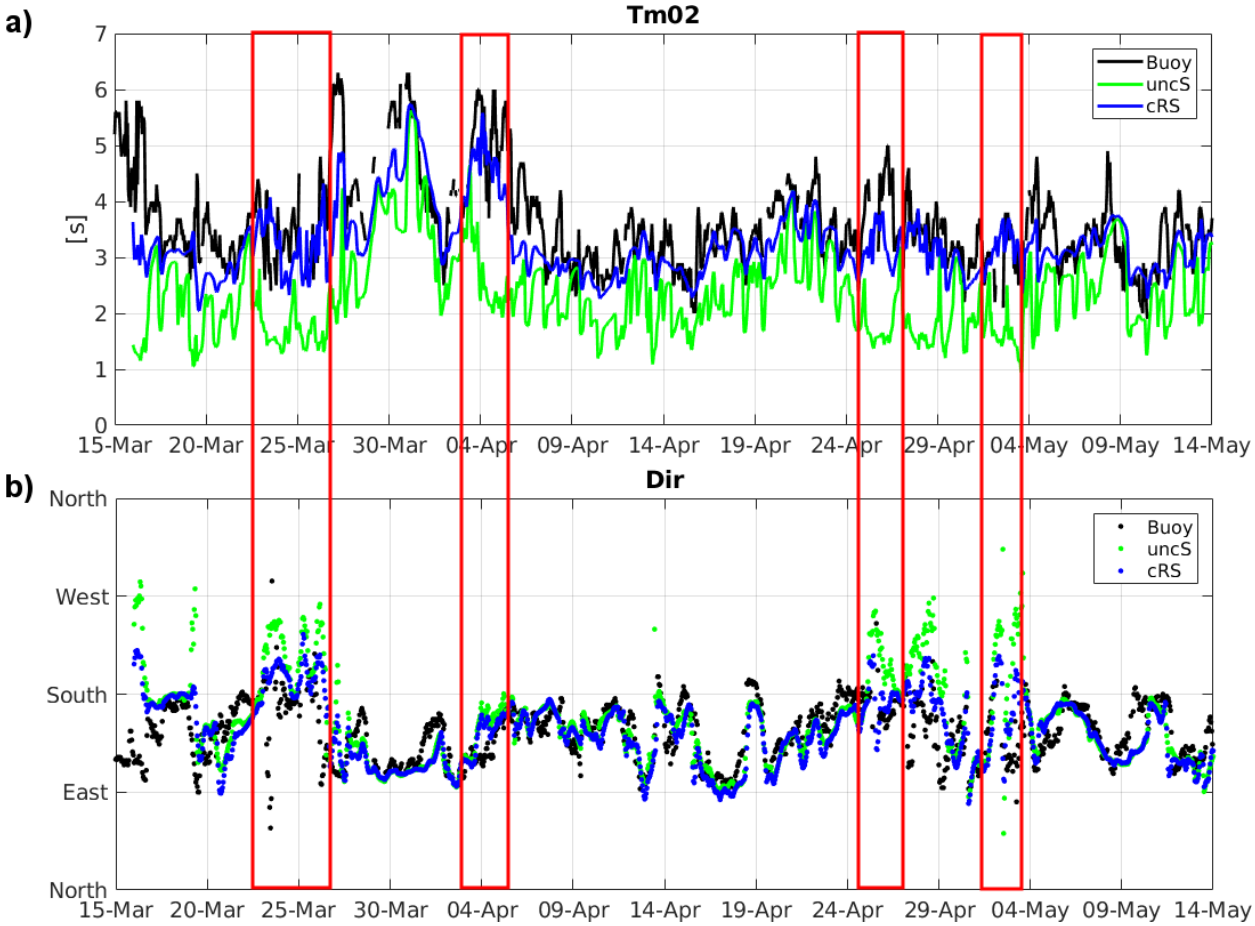

Figure 5.12: Comparison of the Tm_{02} and *Dir* parameters time series obtained with the *uncS* (green) and *cRS* (blue) runs with the data measured by CB (black). Note that the first 24 h of the model results have been rejected.

Regarding the mean wave direction, no relevant differences are observed between the *uncS* and *cRS* runs at deep water (not shown). However, similarly to the results presented in Table 5.2, Figure 5.12b shows that at the CB location (i.e. in shallow waters) the mean wave direction is improved during the wind-jet events. Analyzing the mean wave direction differences between the *uncS* and *cRS* runs, it is found that relevant differences occur near the coastline.

4 Discussion

4.1 Effects of waves on the current field

The main differences between the *uncR* and *cRS* runs have been detected in the water column structure. The vertical mixing of the water column is higher when the waves are considered. This behavior can be explained by the TKE injection and the use of a wave-dependent sea surface stress in the *cRS* run. Similar results have been observed in previous work. Rong et al. (2014) studied the WCI over the Texas–Louisiana Shelf and found that the wave effects can redistribute the freshwater both vertically and horizontally and thus affect the stratification. Bruneau and Toumi (2016) also found that the mixed-layer depths were enhanced in presence of waves. Niu and Xia (2017) investigated how the Lake Erie dynamics were impacted by the wave-induced surface stress and found that it produced an enhancement of the surface mixing and a weakening of the stratification strength. It is important to note that, although the results presented in this study are consistent, there are no available measurements to verify them. Thus, it can not be stated if the *cRS* run is more adjusted to the reality or if it is "over-mixing".

The results presented above show that including the wave effects does not produce a relevant difference to the water current velocity during a wind-jet event and has a weak impact on the water circulation patterns. Similar results were presented by Bruneau and Toumi (2016), who analyzed the wave-induced processes at the Caspian Sea and found that they have a weak impact on the dynamics of the region. The momentum balance analysis has shown that the WF term is one of the leading terms in very shallow areas (until ∼50 m water depth). For this reason, using a numerical domain at a more coastal scale with water depths up to 50 m would probably show more effects at the current field, rather than the domain used in this work, which is focused on the inner shelf, where the water depth reaches values higher than 100 m. As a matter of fact, Osuna and Wolf (2005) studied the WCI in the Irish Sea and found that the effect of waves on currents are evident in the eastern coastal areas, with daily mean current differences larger than 10 cm/s during strong wave events.

4.2 Effects of water currents on the wave field

The numerical results present an improvement in the Tm_{02} parameter when the coupling effects were considered (see Figure 5.12a). Consequently, the inclusion of the current velocity in the estimation of wave period is not negligible, and the Doppler shift must be considered if high-quality modeling is required (similar to Bolaños et al. (2014)). It should be noted that the results

show that the effects of currents on the wave field are stronger for the Tm_{02} parameter than for the Hs parameter. For instance, Osuna and Monbaliu (2004) found that the effect of coupling is 1 order of magnitude stronger for the Tm_{02} parameter (about 20%) than in the case of Hs (about 3%).

During a wind-jet event, a decrease of the Hs is found when the currents are taken into account. The decrease (increase) of Hs in the presence of a following (opposite) current is a well-known effect that has been investigated before by several authors (e.g. Benetazzo et al., 2013; Dutour Sikirić et al., 2013; Viitak et al., 2016). For example, Benetazzo et al. (2013) studied the WCI at the semi-enclosed Gulf of Venice and found that during Bora conditions, with the currents propagating in the same direction as waves, the comparison between coupled and uncoupled models showed a reduction of Hs on the order of 0.6 m when the waves were considered.

The differences in mean wave direction found in shallow waters could be due to the current-induced refraction (Wolf and Prandle, 1999; Olabarrieta et al., 2011). However, it is important to note that these differences were found very near the coastline, specifically until 2 km offshore. Since the model mesh resolution is of 350 m, there are very few grid points and thus it is not possible to extract a concise conclusion about this phenomenon with the results obtained in this study. A study at more coastal scales would be necessary to discern such processes.

Finally, considering the currents causes wave spectral reshaping. During a cross-shelf wind-jet event, the presence of currents induces a shoaling-like process. In general, a reduction of the energy peak and a slight increase of the energy at the tail of the spectrum is observed. This is consistent with the results presented in Fan et al. (2009), where the authors found that when the wave–current interactions were considered, the peak of the frequency spectrum was reduced and shifted toward higher frequency. Rusu (2010) also found that the presence of currents leads to a redistribution of the wave energy over the spectrum.

5 Conclusions

The wave–current interactions have been investigated using numerical models. Three different runs have been performed: an uncoupled ROMS run, an uncoupled SWAN run and a two-way coupled run. The comparison among these runs shows that at the continental shelf the surface water current presents similar results in the coupled and the uncoupled configurations and the momentum balance analysis reveals that the non-conservative wave forcing (WF) term plays an important role in shallow waters. The results show that including wave effects induces major mixing of the water column (the SML increase), mainly due to the TKE injection and the enhanced surface stress. Additionally, when the water currents are considered in the waves forecast, wave spectral reshaping occurs, the Tm_{02} improves and the wave energy (and thus the Hs) diminishes (increases) when the water currents and waves propagate in the same (opposite) direction. The results also indicate that more processes occur in shallower waters, e.g. current-induced refraction, but a more coastal domain with a finer grid is necessary to evaluate them.

Overall, the numerical results have demonstrated to be physically reasonable, being capable of reproducing the well known coupling effects. This has allowed to investigate the impact of the WCIs but more measurements would be needed in order to perform a more quantitatively analysis. Thus, in the future it would be interesting to perform some measurement campaigns to enable more accurate model validation and more exhaustive analysis of the dynamics of the region. In addition, it would also be interesting to investigate the role of the sea surface roughness coupling the ROMS and SWAN models with the WRF model.

Chapter VI

Implementation of an operational forecasting system

"The most reliable way to forecast the future is to try to understand the present."

John Naisbitt

1 Introduction

Nowadays, the ocean dynamics play an important role on many social-economic activities. For this reason, there is a growing interest in understanding the ocean dynamics and forecasting the sea state, not only from a scientific point of view, but also for other end users and fields such as water quality, coastal and port management, navigation, fisheries, tourism, etc. As a result of this increasing demand, wave and ocean circulation operational forecasting systems have been emerging progressively during the last years. In this sense, the Copernicus Marine Environmental Monitoring Service (CMEMS, `http://marine.copernicus.eu`) provides a wide range of oceanographic information at global and European regional scales.

With the aim of forecasting waves and currents at the Catalan coast, two operational forecasting systems have been developed and implemented at the Meteorological Service of Catalonia (SMC). The SMC was founded in 1921 and gave meteorology in Catalonia an enormous boost. Since then, the SMC has developed many meteorological products, has gained considerable international acclaim and has become a reference service regarding the meteorological conditions around the Catalan region. Now, the work presented here represents a first step to expand the maritime services that the SMC offers. In this sense, a wave forecasting system of up to 3 km horizontal resolution and an hydrodynamic forecasting system of 400 m horizontal resolution have been implemented using the Simulating Waves Nearshore (SWAN) model and the Regional Ocean Modeling System (ROMS), respectively. Both models have a forecasting horizon of 72 h and the systems design and implementation have been based on the gained knowledge during the investigations presented in Chapters III, IV and V. The SWAN model has been implemented in the SMC's machines since 2016 but the final version became operative on March 2017 and nowadays is considered the reference wave forecasting model at the SMC. The model is run twice every day, at 00:00 UTC and at 12:00 UTC. In contrast, the ROMS model is still in a pre-operative phase. The model is implemented at the SMC's machines and the latest version has run everyday since October 2017. In this case the model is initialized at 00:00 UTC.

The objective of this chapter is to describe and validate the wave and water current forecasting systems implemented at the SMC. The work is organized as follows. In Section 2, the data used to validate the system and the numerical model implementations are described. The skill assessment of the numerical models is presented in Section 3. A discussion is presented in Section 4, which also includes some future work proposals. Finally, the main conclusions are summarized in Section 5.

2 Methodology

2.1 Numerical Model Implementations

An scheme of the operational system flow is presented in Figure 6.1. In the next sections the ROMS and SWAN model configuration are explained in more detail.

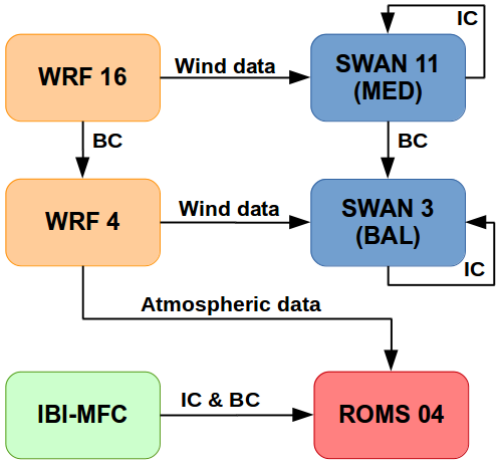

Figure 6.1: Operational system scheme. Data from the WRF (in orange) and IBI-MFC (in green) models are used to force the implemented SWAN (in blue) and ROMS (in red) models.

2.1.1 ROMS Model Implementation

Five coastal domains throughout the Catalan coast have been selected (see the red boxes in Figure 6.2; named TAR, GAR, BAR, GIR and ROS). Each numerical domain has a horizontal resolution of 400 m and a vertical resolution of 20 sigma-levels. The bathymetry of the domains were built using 0.0083° grid resolution bathymetric data from GEBCO (General Bathymetric Chart of the Oceans, www.gebco.net). This data was interpolated to the domain mesh and smoothed by means of a Shapiro filter with a maximum r-factor of 0.35.

The model is forced with data from a previous Weather Research and Forecasting (WRF) model run at the SMC with a spatial resolution of 4 km (which numerical domain is equal to the SWAN BAL domain, see Figure 6.2). It provides 10-m surface winds, atmospheric pressure, relative humidity, atmospheric surface temperature, precipitation and shortwave and longwave net heat fluxes to the ocean model. The ROMS uses these parameters in the COARE algorithm (Fairall et al., 1996) to compute ocean surface stresses and ocean surface net heat fluxes.

The initial and boundary conditions are taken from the IBI-MFC (Iberian Biscay Irish – Monitoring and Forecasting Centre) product. This product (`http://marine.copernicus.eu/`) includes

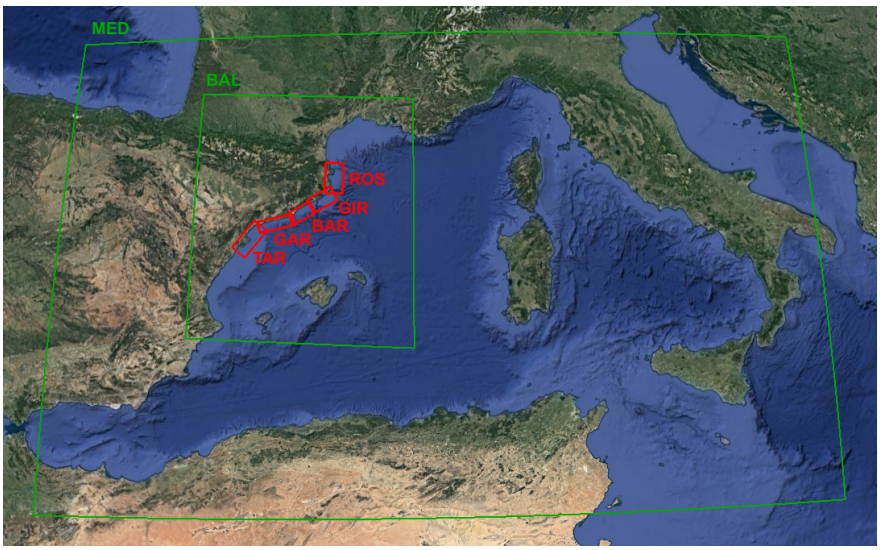

Figure 6.2: SWAN numerical domains (MED and BAL; in green) and ROMS numerical domains (TAR, GAR, BAR, GIR and ROS; in red).

all main forcings (i.e., tidal forcing, high-frequency atmospheric forcing, fresh water river discharge, etc.) and is based on a (eddy-resolving) NEMO model application run at 1/36° horizontal resolution. The outputs provided by the IBI-MFC used as open boundary conditions in our numerical model are 3D daily means of temperature, salinity, zonal velocity and meridional velocity, which are imposed using the clamped boundary conditions, and 2D (surface) hourly means of sea surface height, using the Chapman condition, and barotropic water currents, using the Flather condition.

The model implementation includes a Generic Length-Scale turbulent vertical mixing scheme with the k – ω parametrization, a logarithmic profile for the bottom boundary layer with a bottom roughness of 0.005 m and horizontal mixing terms in geopotential surfaces.

At the TAR domain, the Ebro River discharge is characterized with a climatology of river runoff and temperature generated by means of data from the Automatic Hydrologic Information System of the Ebro River basin (owned by the Confederaciṅn Hidrográfica del Ebro). The river salinity is imposed as a constant value of 18 psu.

2.1.2 SWAN Model Implementation

The wave forecasting system is composed of two numerical domains (see Figure 6.2) and is based on a downscaling technique. The largest domain (MED) covers the western Mediterranean Sea with a spatial resolution of 11 km and provides boundary conditions to a second-level domain (BAL), which covers the Balearic Sea with a spatial resolution of 3 km. The bathymetry introduced in the model is the same one used to create the bathimetric mesh in the ROMS model (0.0083° grid

resolution bathimetric data from GEBCO).

The model is forced with winds from two previous WRF model simulations that run operationally at the SMC. Winds from a WRF model run at 16 km horizontal resolution are used in the 11 km SWAN domain and winds from a WRF model run at 4 km horizontal resolution (and nested to the previous 16 km WRF domain) are used in the 3 km SWAN domain. As initial conditions, the outputs from the model run 12 hours before are used.

The model implementation considers non-stationary conditions, spherical coordinates and nautical convention. The wind growth is computed with a sum of a linear term and an exponential term. For the linear growth, the expression from Cavaleri and Malanotte-Rizzoli (1981) is used, and for the exponential growth, the expression and coefficients of Komen et al. (1984) are used. The nonlinear quadruplet wave interactions are integrated by a fully-explicit computation of the nonlinear transfer with the Discrete Interaction Approximation (DIA; proposed by Hasselmann et al., 1985) per sweep (using default coefficients). For the whitecapping, the Komen et al. (1984) formulation is used with $C_{ds} = 2.36 \cdot 10^{-5}$, $\delta = 1$ and $p = 4$. The spectrum is discretized with a constant relative frequency resolution of $\Delta f = 1.1$ (logarithmic distribution) and a constant directional resolution of $\Delta\theta = 10°$. The discrete frequencies are defined between 0.01 Hz and 1 Hz. Above the high-frequency cutoff, a diagnostic tail f^{-4} is added.

2.2 Data

In order to analyze the skill of the numerical models, different data sources have been used: in-situ measured data from buoys, tide-gauges and a High Frequency (HF) radar from Puertos del Estado (`http://www.puertos.es`) and Jason-3 (J3) and Sentinel-3A (S3A) satellite data from the SEALEVEL_GLO_WAV_L3_NRT_OBSERVATIONS_008_052 data product (`http://marine.copernicus.eu/`).

2.2.1 In-situ Measurements

In this chapter, all the buoys presented in Chapter II Section 2.3 are used. In total, there are 5 deep-water buoys, 2 coastal-water buoys and 2 tide-gauges that are summarized in Table 6.1 and which location can be seen in Figure 6.3b. Unlike the chapters before, in this chapter the buoys have been named with a 5-characters code, with the aim of ease the geographic location when naming them.

Besides the measured parameters shown in Table 6.1, the Tarragona buoy (*tarra*) also measures

water current, temperature and salinity but, unfortunately, it is out of the ROMS numerical domain.

Table 6.1: Puertos del Estado buoy characteristics.

	Code	Lon	Lat	Depth	Measured Parameters
Tarragona	tarra	1.47° E	40.68° N	688 m	Hs, Dir, Tm_{02}, Tp, $Wind$
Begur	begur	3.65° E	41.92° N	1200 m	Hs, Dir, Tm_{02}, Tp, $Wind$
Dragonera	drago	2.10° E	39.56° N	135 m	Hs, Dir, Tm_{02}, Tp, $Wind$
Mahon	mahon	4.42° E	39.72° N	300 m	Hs, Dir, Tm_{02}, Tp, $Wind$
Valencia	valen	0.21° E	39.52° N	260 m	Hs, Dir, Tm_{02}, Tp, $Wind$
Tarragona Coast	ttarr	1.19° E	41.07° N	15 m	Hs, Dir, Tm_{02}, Tp, sst
Barcelona Coast	tbarc	2.20° E	41.32° N	68 m	Hs, Dir, Tm_{02}, Tp, sst
Tarragona Tide Gauge	tartg	1.21° E	41.08° N	-	ssh, $Wind$
Barcelona Tide Gauge	bcntg	2.17° E	41.34° N	-	ssh, $Wind$

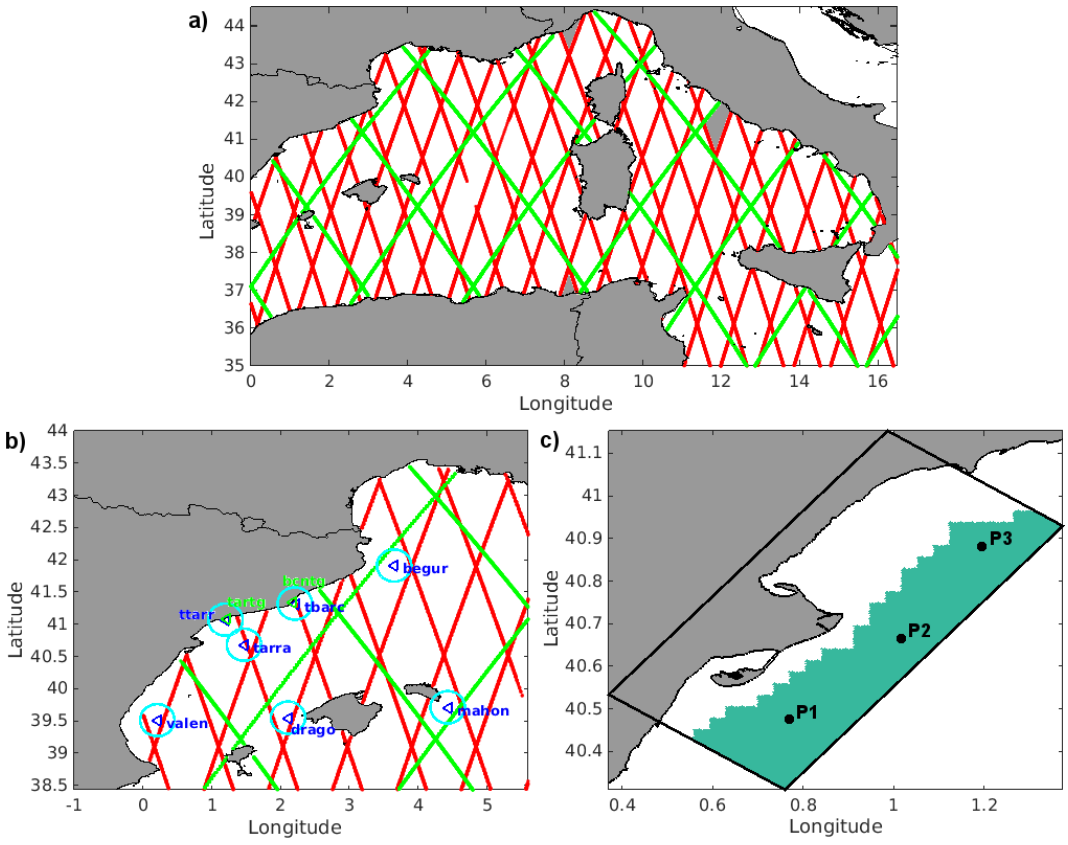

Figure 6.3: a) S3A (in red) and J3 (in green) satellite tracks for the whole MED domain. b) S3A and J3 satellite tracks for the BAL domain, buoy locations (blue triangles) with the corresponding collocation radius and tide gauge locations (green triangles). c) HF radar area with more than 50% of available data inside the TAR numerical domain and location of three validation points (P1, P2 and P3).

2.2.2 HF radar data

The HF radar provides hourly measurements of the current velocities in the top meter of the water column with a horizontal resolution of 3 km and a cut-off filter of 100 cm/s. The resulting HF radar validation area after rejecting the points with less than 50% data availavility (see Section 2.4 in Chapter II) is shown in Figure 6.3c. The figure also shows the points used for validation and analysis of the model results. The statistics from the comparison between HF radar data and sub-surface water currents measured in *tarra* are presented in Table 6.2. The results show good agreement for both along- and cross-shelf components but it is important to notice the relatively high RMSD values.

Table 6.2: Along- (u) and cross-shelf (v) current components statistics from the comparison between the available HF radar data and the available buoy data (*tarra*) for the study period.

	bias (cm/s)	RMSD (cm/s)	r	d
Along-shelf component	3.07	11.69	0.76	0.86
Cross-shelf component	-4.09	10.58	0.65	0.77

2.2.3 Satellite data

Data from Jason-3 (J3) and Sentinel-3A (S3A) are used, which are available at the Copernicus catalogue since July 2017. With the aim of studying the reliability of such data, a preliminary validation of the satellite data is performed. The satellite data has been collocated in space and time into the buoy locations (see Section 2.5 in Chapter II). In Figures 6.3a and 6.3b the satellite tracks and the collocation radius for each buoy are presented. It can be seen that, in the S3A case, all the buoy locations have satellite data within their collocation radius but, in the J3 case, only the *begur* and *mahon* buoys have data.

Some statistics comparing the buoy measured data and the S3A and J3 satellite data are presented in Tables 6.3 and 6.4, respectively. The period used to obtain these metrics is from 15 July 2017 to 15 March 2017 (8 months). First, it is important to notice the scarce number of samples, which limits the satellite data quality validation. From the obtained statistics, it is observed that S3A data is more biased from the observations than the J3 data. This is also observed in Figure 6.4a, where the scatter plots of the collocated buoy-satellite pair of points are presented. Additionally, S3A data show worst RMSD values than J3 data but, in general, both satellite data sets show good agreement with the observations. Finally, in Figure 6.4b the time series of *begur* and *mahon* buoys are plotted together with the satellite collocated data. The visual inspection allows to see that the

satellite data are able to capture the wave peaks.

Table 6.3: bias, MAE and RMSD (in meters) comparing each buoy data with the collocated S3A data during the period 15 July 2017 – 15 March 2018.

	bias (m)	MAE (m)	RMSD (m)	N samples
begur	0.31	0.33	0.52	15
drago	0.26	0.27	0.33	18
mahon	0.43	0.43	0.57	9
tarra	0.16	0.17	0.20	18
tbarc	0.22	0.22	0.24	6
ttarr	0.33	0.34	0.44	8
valen	0.10	0.14	0.16	15

Table 6.4: bias, MAE and RMSD (in meters) comparing each buoy data with the collocated J3 data during the period 15 July 2017 – 15 March 2018.

	bias (m)	MAE (m)	RMSD (m)	N samples
begur	-0.04	0.19	0.24	23
mahon	0.09	0.20	0.33	23

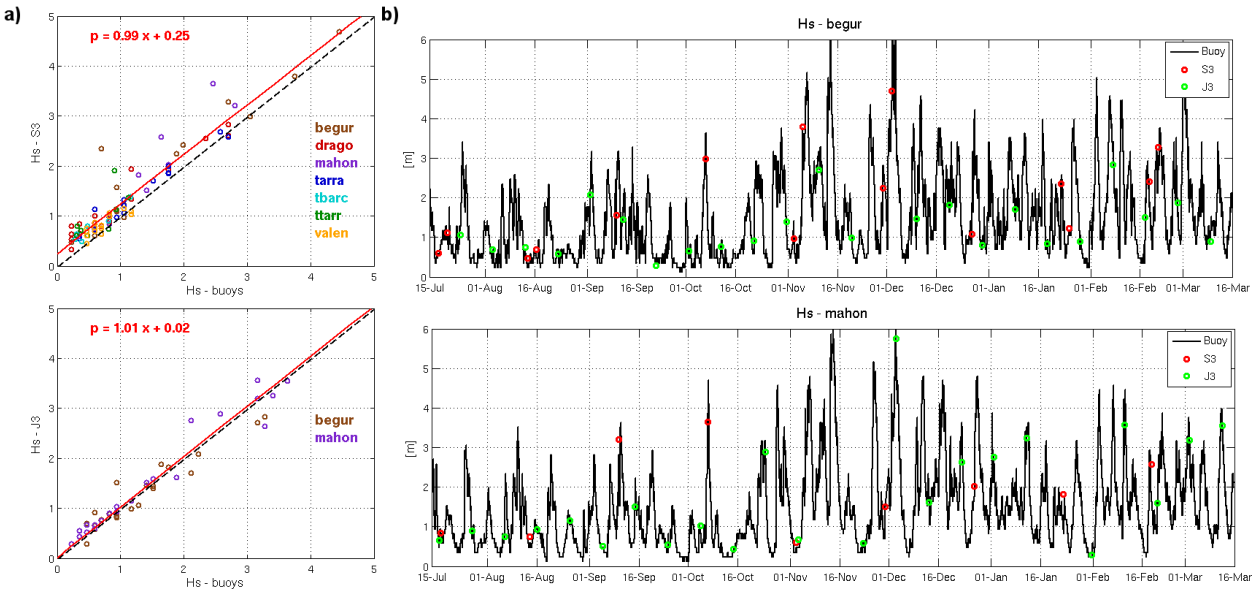

Figure 6.4: a) Scatter plots of the collocated buoy-satellite pair of points. b) Time series comparing buoy data and satellite data at *begur* and *mahon* buoy sites. The red line is the linear regression line (p=ax+b) and the black dashed line show the line that would correspond to a perfect agreement.

2.3 Wave Alerts Verification Method

A useful tool to validate the numerical model ability of forecasting wave storms is the wave alerts verification method used at the SMC. This method distinguish between two alerts: one for situations of $Hs > 2.5m$ (Level 1) and another for situations of $Hs > 4m$ (Level 2). The verification of these alerts is done calculating the daily maximum forecasted and observed Hs values at each buoy location and building a 3×3 contingency table like the one presented in Table 6.5.

Table 6.5: 3×3 contingency table. The Forecasted (F) Hs are set against the Observed (O) Hs and three levels of Hits, Misses and False Alarms (FA) are encountered.

	F < 2.5	**2.5<F<4**	**F > 4**
O < 2.5	Hit1	FA1	FA3
2.5<O<4	Miss1	Hit2	FA2
O > 4	Miss3	Miss2	Hit3

From this contingency table, the indexes used in the verification process are:

$$Bias = \frac{hits + falsealarms}{hits + misses} \tag{6.1}$$

$$POD = \frac{hits}{hits + misses} \tag{6.2}$$

$$FAR = \frac{falsealarms}{hits + falsealarms} \tag{6.3}$$

$$CSI = \frac{hits}{hits + misses + falsealarms} \tag{6.4}$$

where, POD is the Probability Of Detection, FAR is the False Alarm Ratio and CSI is the Critical Success Index. The definition of hits, misses and false alarms depend on the warning level that is verificated. Since the aim is to evaluate the model capacity of generating a Level 1 alert when a $Hs > 2.5$ m is observed and a Level 2 alert when a $Hs > 4$ m is observed, the following definitions have been adopted for each level:

Level 1	**Level 2**
hits = Hit2 + Hit3 + FA2 + Miss2	hits = Hit3
false alarms = FA1 + FA3	false alarms = FA2 + FA3
misses = Miss1 + Miss3	misses = Miss2 + Miss3

Finally, an index called "Accuracy" has also been defined as:

$$Accuracy = \frac{Hit2 + Hit3}{Hit2 + Hit3 + Miss1 + Miss2 + Miss3 + FA1 + FA2 + FA3} \tag{6.5}$$

which is the percentage of the successfully warned alerts with respect to all the alerts (including observed and forecasted).

3 Numerical Models Skill Assessment

3.1 ROMS Skill Assessment

The ROMS model has run every day since 1 October 2017, generating hourly information on water currents, sea surface temperature (*sst*) and sea surface height (*ssh*), among others. In this section these parameters are compared with observations in order to verify the numerical model results. The period used to perform this validation is from 1 October 2017 to 15 March 2018 (5.5 months). In addition, since the model has a forecasting horizon of 72 h (3 days), the validation process distinguish between the results obtained for the first 24 forecasted hours (DAY 1), from 25 to 48 forecasted hours (DAY 2) and from 49 to 72 forecasted hours (DAY 3).

First, in order to verify the model nesting with IBI-MFC, in Figure 6.5, the nested and parent solution for the surface water currents at 25 February 2018 04:00 (UTC) are presented together. It is observed that there is a continuity between both models and that the downscaling technique preserve the mesoscale information inherited from the IBI-MFC model.

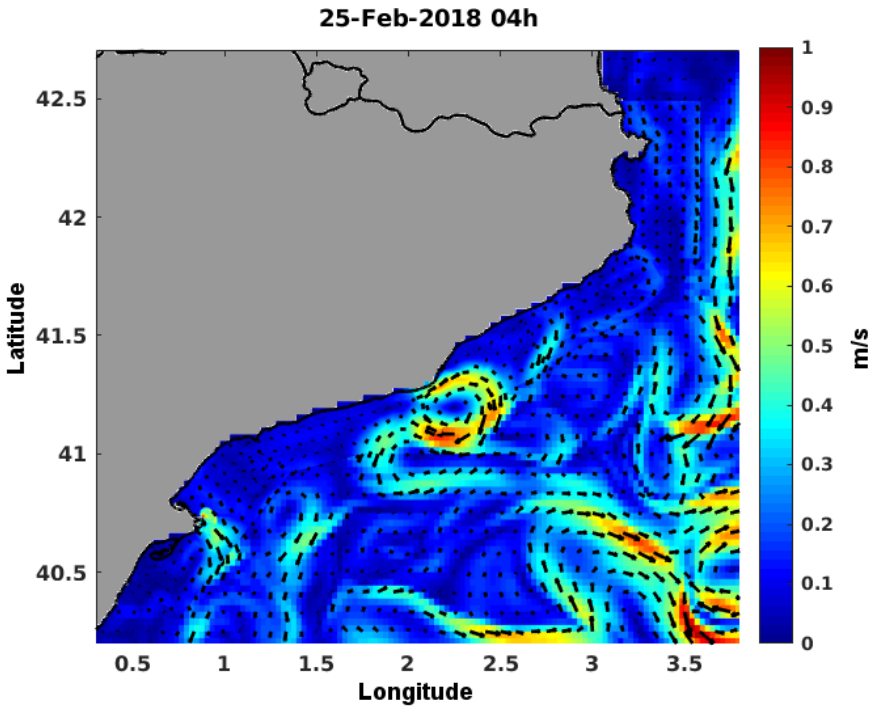

Figure 6.5: Surface water currents from IBI-MFC overlapped by the coastal domains results at 25 February 2018 04:00 UTC. The red arrows correspond to the IBI-MFC circulation and the black arrows to the coastal domains circulation.

The observed temperature time series from *tbarc* (3,049 available observations) and *ttarr* (3,907 available observations) buoys are compared with the forecasted *sst*. The comparison gives similar values for both buoys and for all the forecasting ranges (DAY 1, DAY 2 and DAY 3), with RMSD

values between 0.4 – 0.5° C and correlations around 0.98. Thereby, the results present a rather good agreement. Regarding the *ssh* skill assessment, it is done by means of the comparison with the *bcntg* (3,975 available observations) and *tartg* (3,943 available observations) tide gauges. In this case, the results are also very similar for both buoys and for all the forecasting ranges, with RMSD values between 5 – 6 cm and correlations around 0.88. In Figure 6.6, the *ssh* time series observed at *bcntg* is compared with the forecasted one (which has been obtained concatenating the first 24 forecasting hours, i.e. corresponds to the DAY 1 forecasting range). The figure also includes the meteorological tide, which has been substracted using the T_TIDE software (Pawlowicz et al., 2002). It is observed that the *ssh* variability is mainly due to effects of storm surges rather than due to the astronomical tide. This is because the Mediterranean Sea is a microtidal environment and, accordingly, the astronomical tides are not the main factor that contributes to the sea level variability, on the contrary, it is more influenced by the meteorological tide.

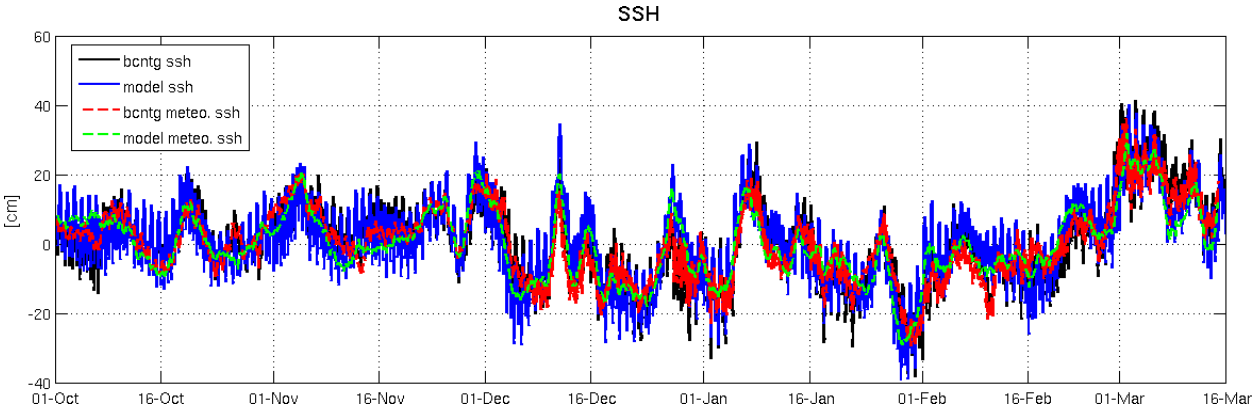

Figure 6.6: *ssh* and its meteorological component comparison at bcntg. The meteorological tide was obtained using the T_TIDE software (Pawlowicz et al., 2002).

The HF radar data allows a spatial validation of the model results from the TAR domain. The surface water currents have been rotated with the numerical domain inclination angle in order to obtain the along- and cross-shelf water current components. The along-shelf component is positive from SW to NE and the cross-shelf component is positive onshoreward, i.e. from SE to NW. In Figure 6.7 the 2D distribution of correlation and skill score comparing the numerical results from each forecasting range with the HF radar data is presented. It is observed that the modeled along-shelf water current show higher agreement with the HF radar data than the cross-shelf component. However, overall, the statistical metrics show a reasonable good agreement with the measurements. On the one hand, the along-shelf component reaches r values higher than 0.6 in front of the Ebro Delta and d values higher than 0.7 in most of the numerical domain. On the other hand, the cross-shelf component shows correlations between 0.4 and 0.6 and skill scores higher than 0.6.

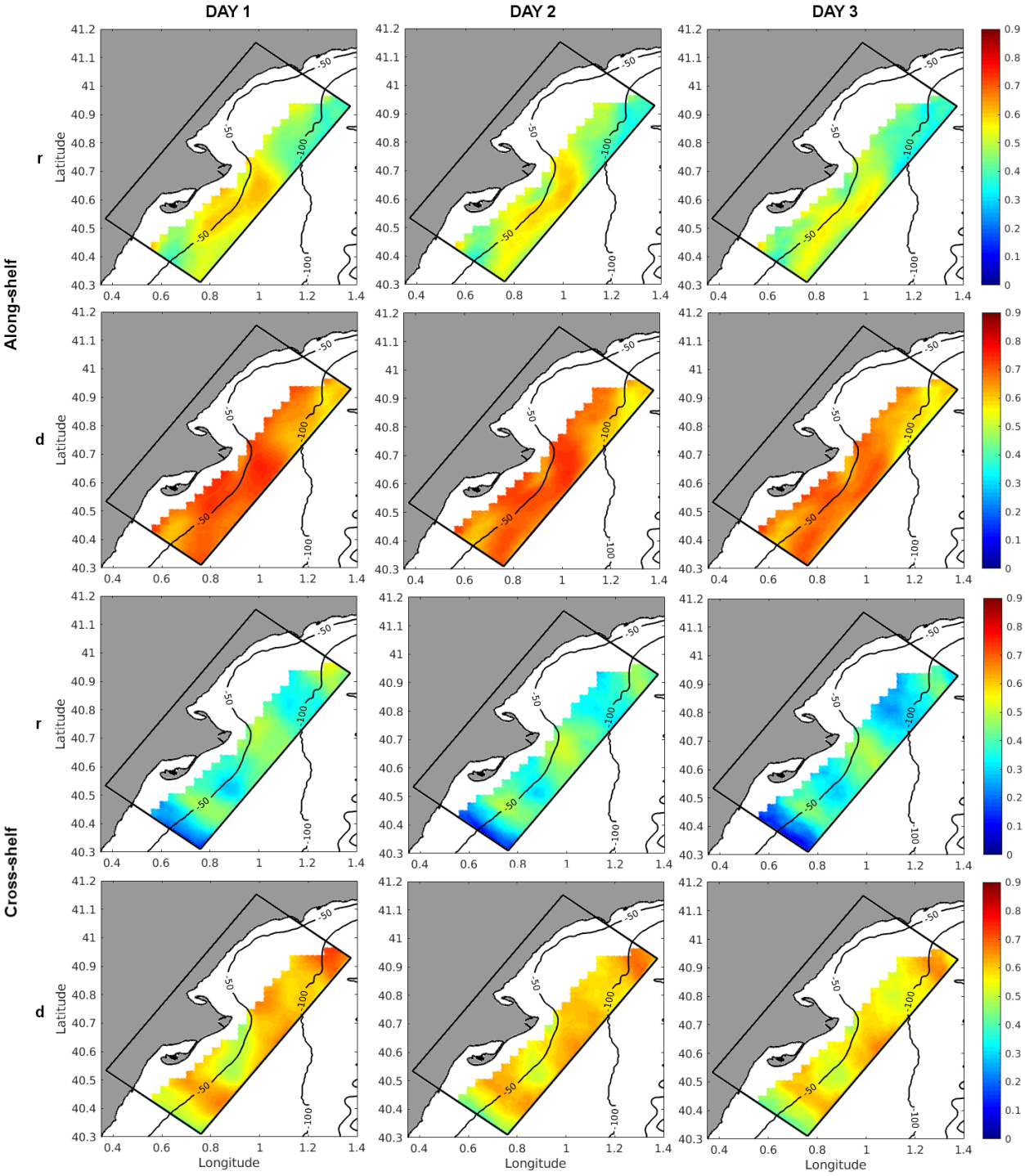

Figure 6.7: Along- and cross-shelf Pearson's correlation and skill score comparing the model results for each forecasting range with the HF radar data.

In Figures 6.8 and 6.9 the along- and cross-shelf modeled subtidal surface water currents, respectively, are compared with the IBI-MFC data and the HF radar data in the three points presented in Figure 6.3c. The model results correspond to the concatenated DAY 1 forecasting range results and the subtidal currents have been obtained applying a 10th order Butterworth filter with a cut-off period of 30 h. The results show that both IBI-MFC and forecasted along-shelf components have similar behaviour and major differences are observed in the cross-shelf component, where the

forecasted water currents seem to fit somehow better with the HF radar data than the IBI-MFC results. This is also observed in Tables 6.6 and 6.7, where the statistical metrics comparing IBI-MFC and forecasted subtidal water currents with the HF radar data are presented, respectively. The comparison of the statistical metrics of IBI-MFC and forecasted range DAY 1 shows that the forecasted results are better correlated witht the HF radar data than IBI-MFC, specially in the cross-shelf component, where the improvement is more remarkable. Additionaly, comparing the results for each forecasting range, it is found that the results fit diminish as the forecasting range increase, with higher bias and RMSD and lower r and d. However, in all cases, the obtained correlations are better than the IBI-MFC ones.

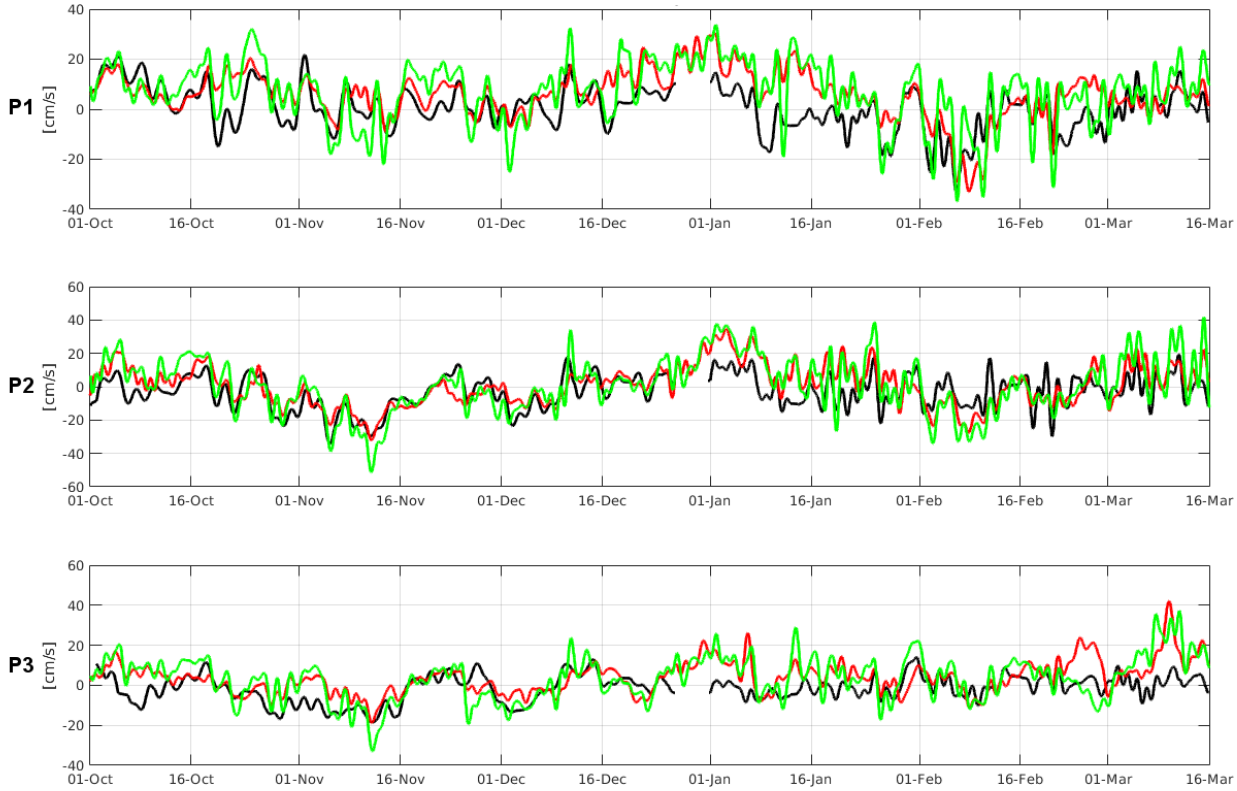

Figure 6.8: Along-shelf time series comparison of modeled (in green), IBI-MFC (in red) and HF radar (in black) subtidal water currents at the points presented in Figure 6.3c.

Table 6.6: Statistics comparing the along- and cross-shelf IBI-MFC subtidal water currents with the HF radar data. The bias and RMSD units are cm/s.

	Along-shelf				**Cross-shelf**			
	bias	RMSD	r	d	bias	RMSD	r	d
P1	5.16	10.00	0.58	0.72	3.23	7.04	0.37	0.58
P2	3.53	10.12	0.65	0.78	1.24	9.48	0.33	0.59
P3	5.02	9.06	0.45	0.59	9.10	13.79	0.18	0.46

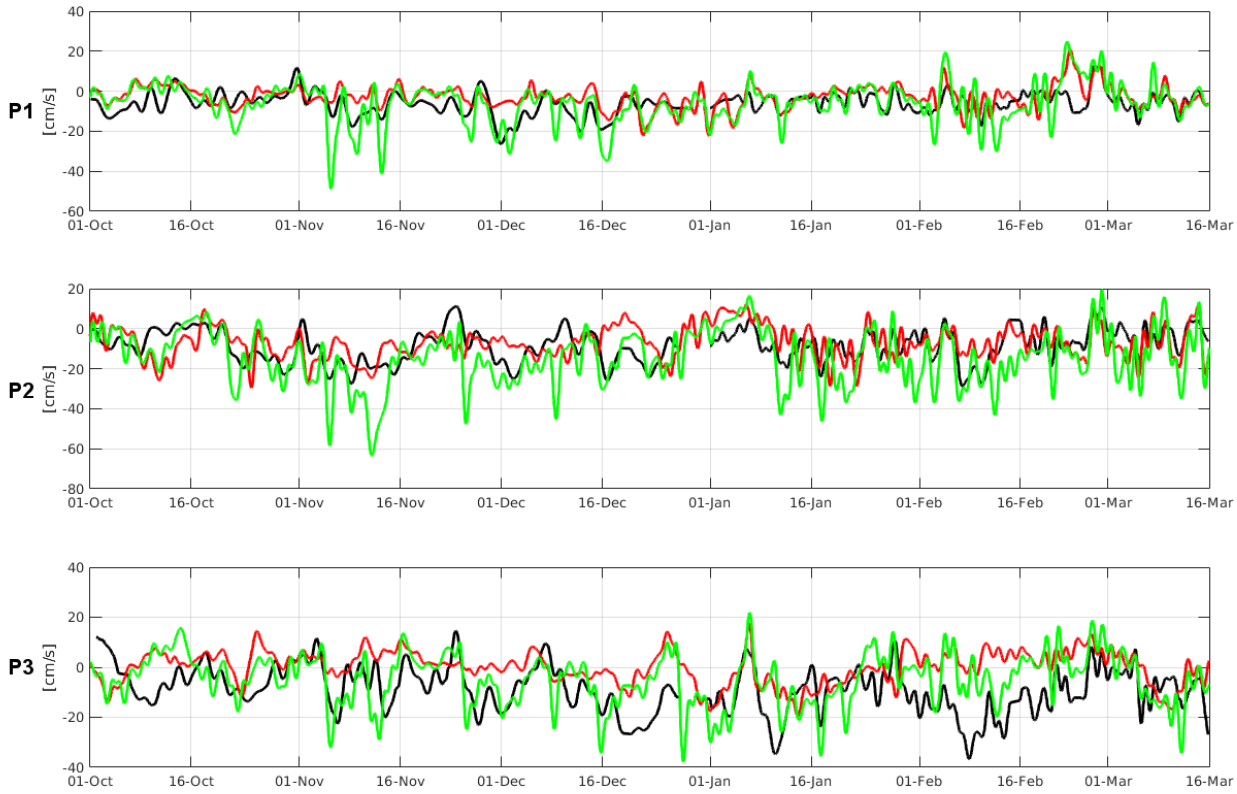

Figure 6.9: Cross-shelf time series comparison of modeled (in green), IBI-MFC (in red) and HF radar (in black) subtidal water currents at the points presented in Figure 6.3c.

Table 6.7: Statistics comparing the along-and cross-shelf modeled subtidal water currents with the HF radar data. The bias and RMSD units are cm/s.

Along-shelf												
	DAY 1				**DAY 2**				**DAY 3**			
	bias	RMSD	r	d	bias	RMSD	r	d	bias	RMSD	r	d
P1	6.11	11.21	0.65	0.73	6.83	12.20	0.61	0.69	7.25	12.22	0.60	0.68
P2	3.53	10.12	0.65	0.78	3.00	12.89	0.65	0.74	3.79	13.67	0.63	0.72
P3	4.66	9.96	0.55	0.65	3.90	9.83	0.52	0.64	4.02	10.25	0.51	0.63
Cross-shelf												
	DAY 1				**DAY 2**				**DAY 3**			
	bias	RMSD	r	d	bias	RMSD	r	d	bias	RMSD	r	d
P1	0.22	7.93	0.60	0.70	-0.87	8.81	0.58	0.67	-1.25	9.45	0.53	0.63
P2	-6.45	12.48	0.62	0.67	-4.50	12.75	0.62	0.69	-4.87	13.00	0.62	0.68
P3	4.23	11.50	0.40	0.62	5.42	11.87	0.42	0.62	5.29	12.04	0.43	0.63

Unfortunately, the lack of more observations along the Catalan coast does not allow to validate more exhaustively the five ROMS local domains. However the model results are consistent with the IBI-MFC results. The same main patterns are observed in both model results, with some

differences due to the higher resolution of the coastal domains. Thus, it is difficult to evaluate if the local domains are able to improve to IBI-MFC results along the Catalan coast beyond the TAR domain but, at least, they seem to be reliable and have the added value of higher resolution.

3.2 SWAN Skill Assessment

The SWAN application has run every day since March 2017, generating hourly information of significant wave height (Hs), mean wave period (Tm) and peak wave period (Tp), among others. In this section these parameters are compared with observations in order to verify the numerical model skill. The period used to perform this validation is from 15 March 2017 to 15 March 2018 (1 year). In addition, similarly as before, the validation process distinguish between the results obtained for the DAY 1, DAY 2 and DAY 3 forecasting ranges.

In the first place, the buoy wave roses are compared with the wave roses generated with the BAL domain results. In Figure 6.10 the wave roses obtained for each buoy and the forecasted ones (which have been generated considering the results corresponding to the DAY 1 forecasting range) are presented (nautical convention is used). In all cases, the model has captured the main wave direction measured by the buoys. Notice that *tbarc* and *ttarr* buoys do not measure wave direction. The highest Hs are found at *begur* and *mahon*, corresponding to northerly wave storms. At *drago* there are also high Hs from the NE. These northeasterly storms are usually associated to the same northerly winds that generated the northerly storms at *begur* and *mahon*. Such winds are then deviated to the SW developing the northeasterly wave storms at *drago* and the easterly storms at *tarra* and *valen*. At the *tarra* buoy location there are three differentiated wave directions: east, south and northwest, being the latest associated with the local wind-jet phenomena. Finally, it is observed that at *tbarc* and *ttarr* (coastal buoys) the wave directions correspond to onshoreward events and the Hs rarely exceeds 1 m.

A very useful method to obtain a quick view of the model skill at various locations is the Taylor diagram. In Figure 6.11 the Taylor diagrams of the results obtained with the BAL numerical domain at all the available buoys is presented. Three parameters are plotted for each forecasting range: Hs (circles), Tp (triangles) and Tm (diamonds). It is important to notice that in order to be able to compare different variables and different locations at the same Taylor diagram the STD and RMSD from the predicted data have been normalized by the STD of the observed data. For this reason, the "real" statistical metrics for each forecasting range are presented in Figures 6.12, 6.13 and 6.14. In general, Hs and Tp forecasts have similar variance compared to the observations, while the Tm parameter presents $\sim$1.5 – 1.7 times the observed variability (except at *ttarr*). The

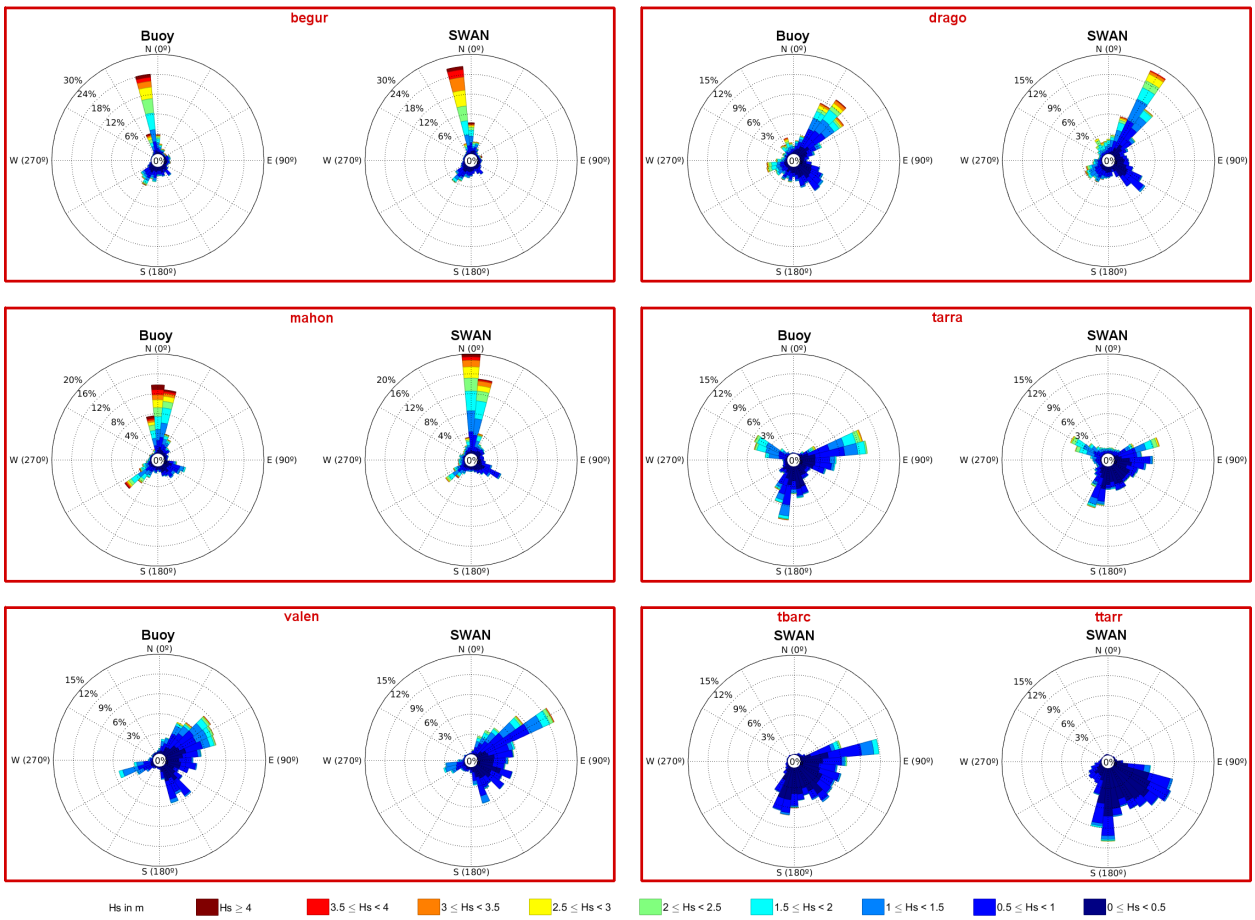

Figure 6.10: Modeled and measured wave roses (in nautical convention) at each buoy location.

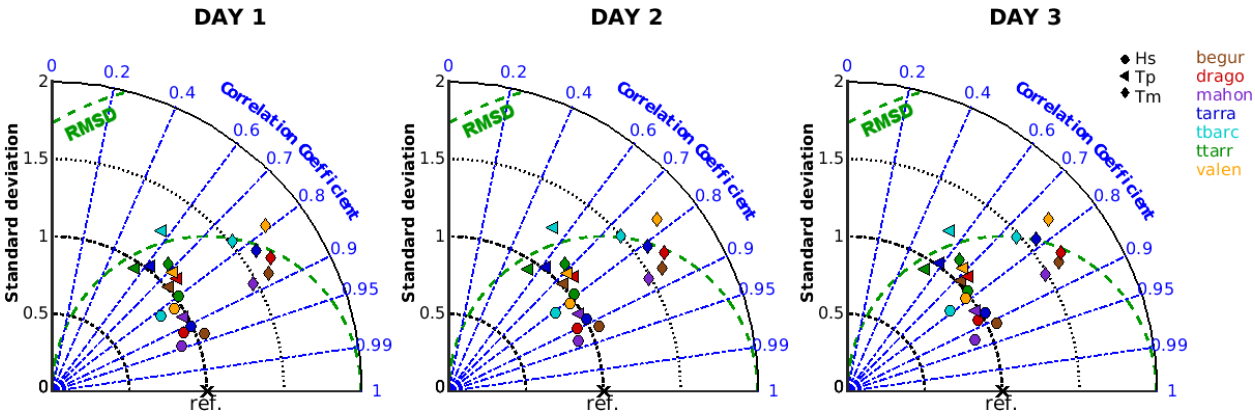

Figure 6.11: Taylor diagrams including Hs, Tp and Tm parameters for all buoys and for each forecasting range.

Hs parameter shows high correlations at all buoy locations but there is a clear difference between the ∼0.9 correlation at *begur*, *drago*, *mahon* and *tarra* and the ∼0.8 correlation at *tbarc*, *ttarr* and *valen*. Additionally, it can be observed that, going from DAY 1 to DAY 3, the correlation coefficient slightly diminish.

Regarding the results presented in Figures 6.12, 6.13 and 6.14, it is observed that, although the statistical metrics tend to get slightly worse as the forecasting range increases, the model results show good agreement for all the forecasting ranges. The Hs bias, MAE, RMSD and d are in the

ranges of -0.11 – 0.4 m, 0.12 – 0.30 m, 0.17 – 0.43 m and 0.87 – 0.97, respectively. Figure 6.12 show that the highest Hs MAE and RMSD occur at *begur* and *mahon* sites while the lower values are found at *ttarr* and *tbarc*. However, it is important to bear in mind that the Hs at *begur* and *mahon* sites is much higher than at *ttar* and *tbarc* sites (see Figure 6.10) and, considering the mean Hs values, the relative error at each buoy is very similar.

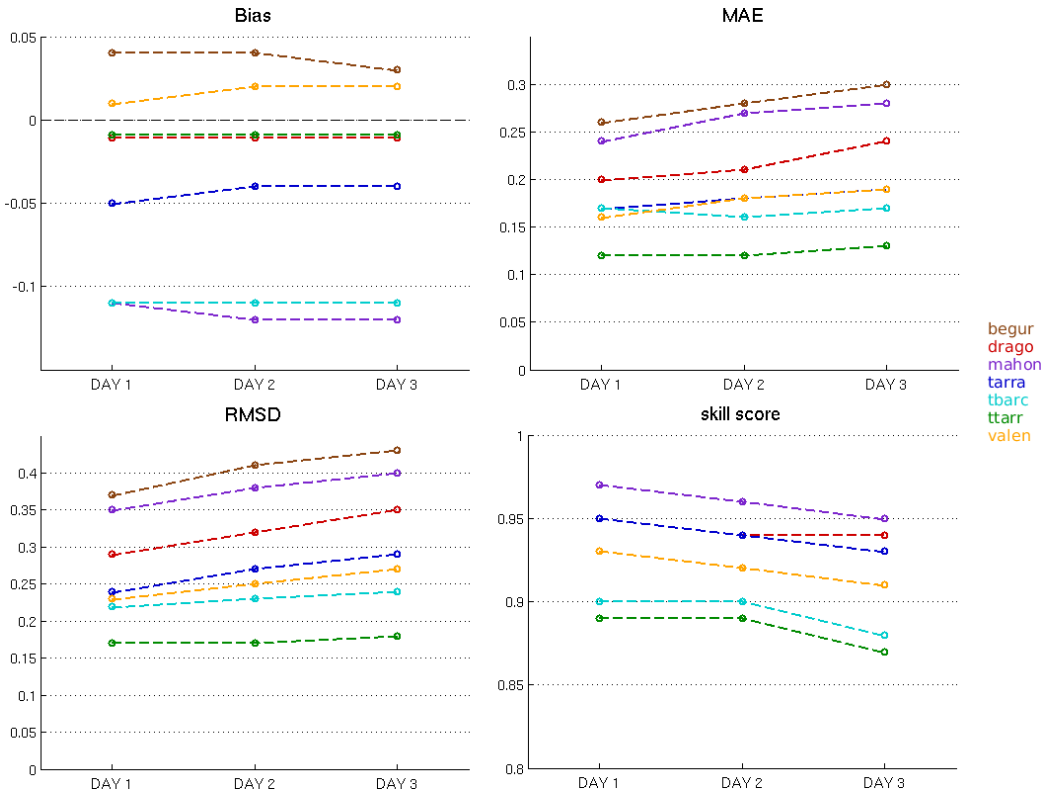

Figure 6.12: bias, MAE, RMSD and d comparing the predicted Hs with observations at each buoy location and for each forecasting range.

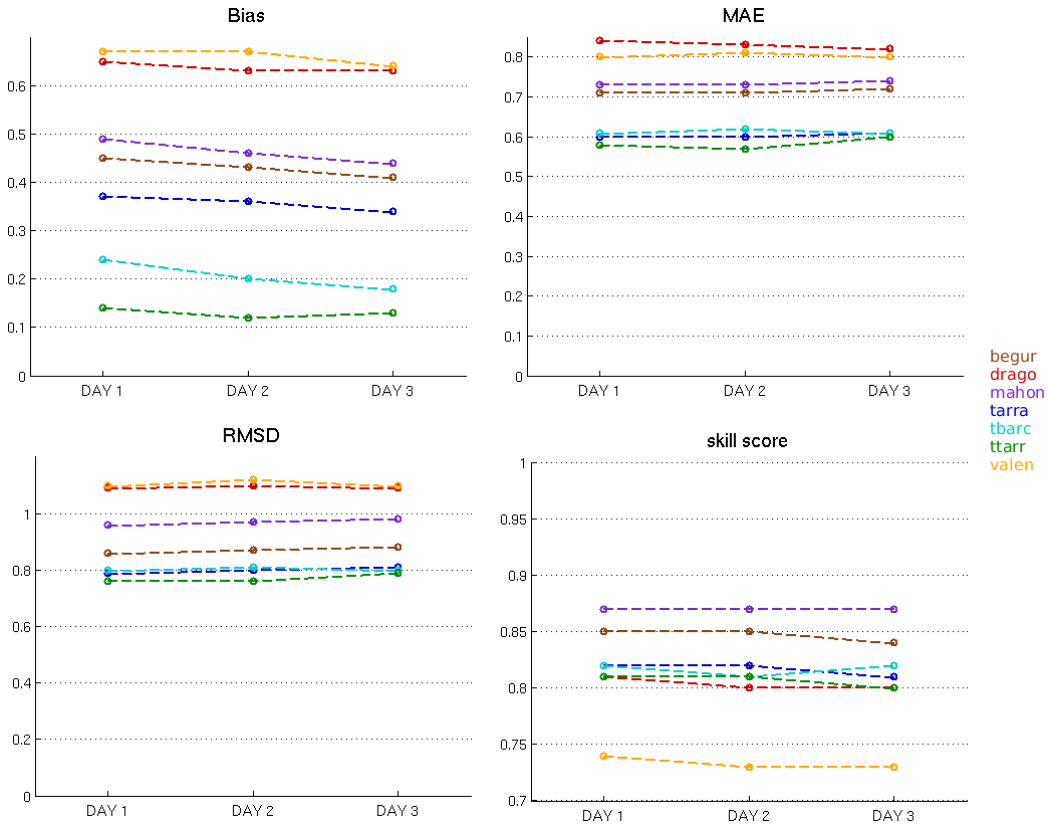

Figure 6.13: bias, MAE, RMSD and d comparing the predicted Tp with observations at each buoy location and for each forecasting range.

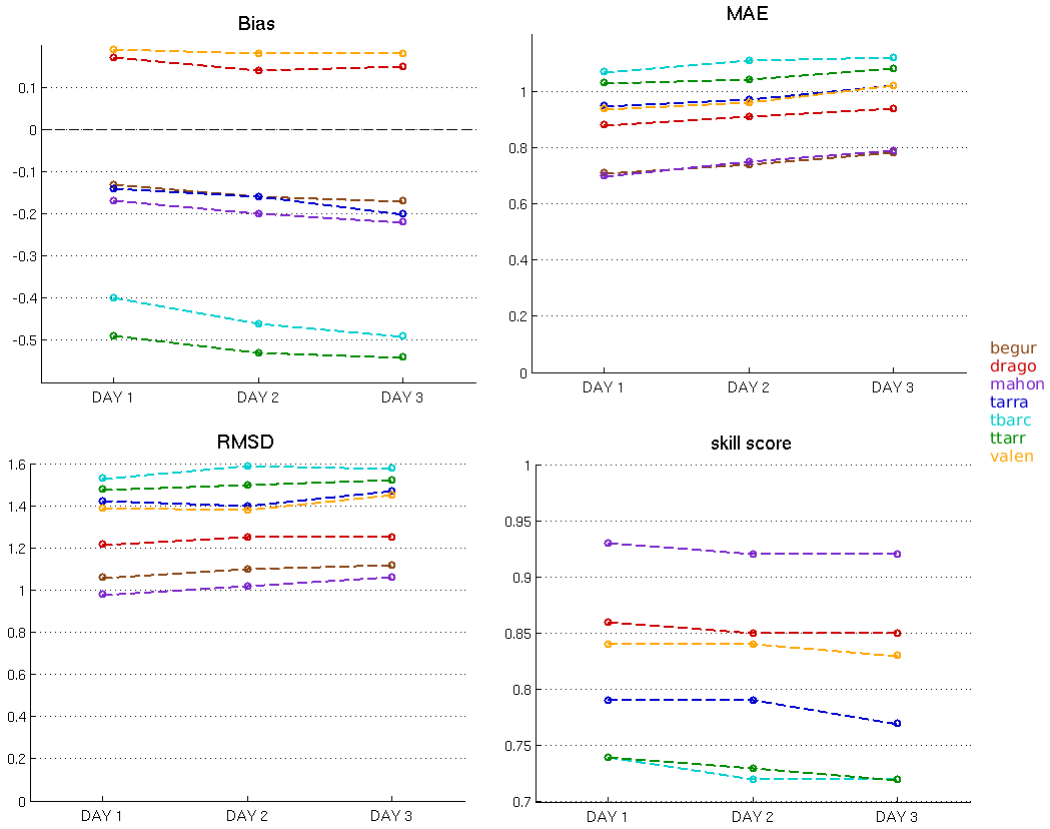

Figure 6.14: bias, MAE, RMSD and d comparing the predicted Tm with observations at each buoy location and for each forecasting range.

In Figure 6.15 the scatter plots obtained from the comparison between all the available buoy measurements and the BAL domain results for each forecasting range is presented. Although more dispersion is observed in the DAY 3 forecasting range, the results show a good fit with the measurements in the three cases, with regression slopes of 0.9 – 0.91.

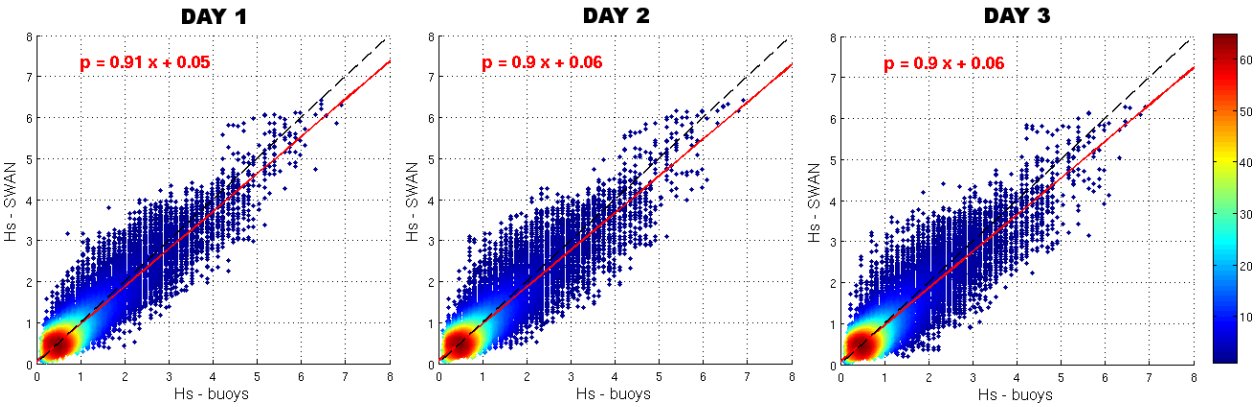

Figure 6.15: Scatter plots considering data from all buoys together. The colors represent the density of points. The red line is the linear regression line (p=ax+b) and the black dashed line show the line that would correspond to a perfect agreement.

Now the predicted Hs data is compared with S3A and J3 data. Since the satellite data is available from July 2017, the validation period is somehow reduced: from 15 July 2017 to 15 March 2018 (8 months). The scatter plots and the statistics comparing the modeled Hs with the S3A and J3 measurements are presented in Figure 6.16 and Tables 6.8 and 6.9, respectively. It is observed that the BAL domain is able to improve the MED domain results, achieving lower biases, higher skill scores and better regression slopes. The scatter plots show that the modeled and observed Hs have a better fit for Hs values lower than 4 m. For higher Hs values the modeled data tend to be more underestimated.

Table 6.8: Statistics comparing the modeled Hs and the S3A measurements for each forecasting range. The bias, MAE and RMSD unit is meters and the number of pair of points is also presented.

		bias	MAE	RMSD	r	d	N samples
MED	DAY 1	-0.32	0.36	0.44	0.94	0.94	26,966
	DAY 2	-0.33	0.38	0.46	0.93	0.93	
	DAY 3	-0.33	0.40	0.50	0.91	0.92	
BAL	DAY 1	-0.17	0.33	0.42	0.93	0.96	6,171
	DAY 2	-0.18	0.34	0.45	0.92	0.95	
	DAY 3	-0.20	0.37	0.50	0.90	0.94	

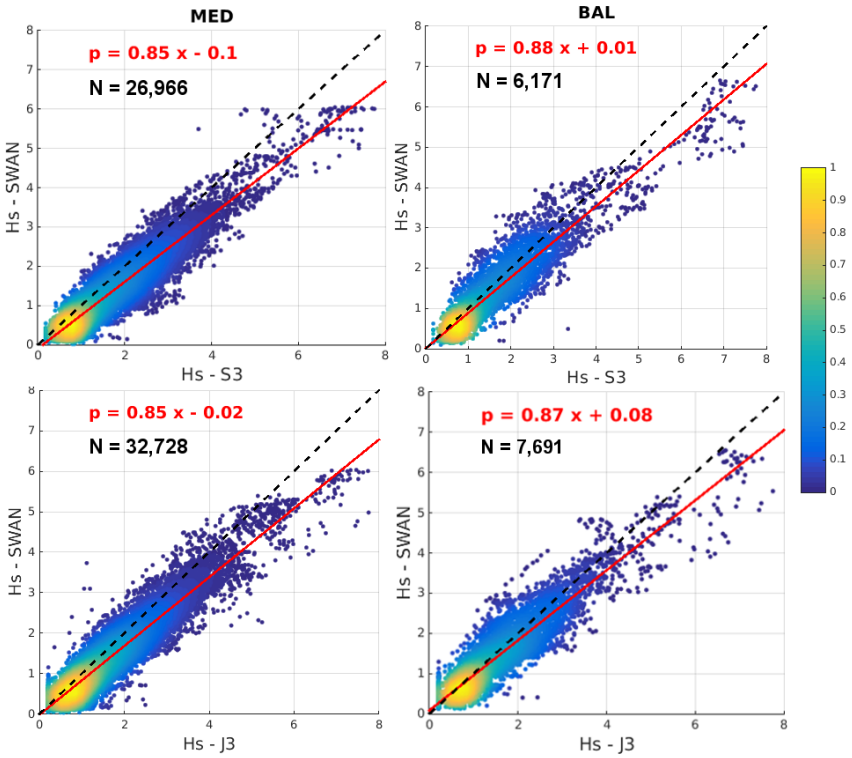

Figure 6.16: Scatter plots comparing the forecasted Hs values (DAY 1) with the observed ones by S3A (top) and J3 (bottom) for each domain. The colors represent the density of points. The red line is the linear regression line (p=ax+b) and the black dashed line show the line that would correspond to a perfect agreement. The number of satellite-model pair of points obtained after the collocation process is also presented.

Table 6.9: Statistics comparing the modeled Hs and the J3 measurements for each forecasting range. The bias, MAE and RMSD unit is meters and the number of pair of points is also presented.

		bias	MAE	RMSD	r	d	N samples
MED	DAY 1	-0.23	0.31	0.38	0.94	0.95	32,728
	DAY 2	-0.23	0.32	0.40	0.93	0.95	
	DAY 3	-0.25	0.35	0.44	0.92	0.94	
BAL	DAY 1	-0.11	0.32	0.41	0.92	0.96	7,691
	DAY 2	-0.10	0.33	0.41	0.92	0.96	
	DAY 3	-0.12	0.35	0.45	0.91	0.95	

With the aim of performing a spatial validation of the wave model, the collocated satellite-model pair of points for each available measured time lapse have been interpolated in a 2D mesh. In Figure 6.17, the bias, MAE and r are presented, including also a map of the available number of observation at each point. It is observed that the predicted Hs tends to be negatively biased and presents MAEs in the range 0.2 – 0.5 m. The worse bias and MAE values are found in the center of the domain. Regarding the correlation, the predicted Hs is very high correlated with the observed

one, with values higher than 0.9. Additionally, it is observed that, specially in the S3A case, the correlations tend to diminish near the coastline. However, it is difficult to state if this correlation decrease is due to the numerical model skill or due to the S3A ability in measuring the Hs near the coastline.

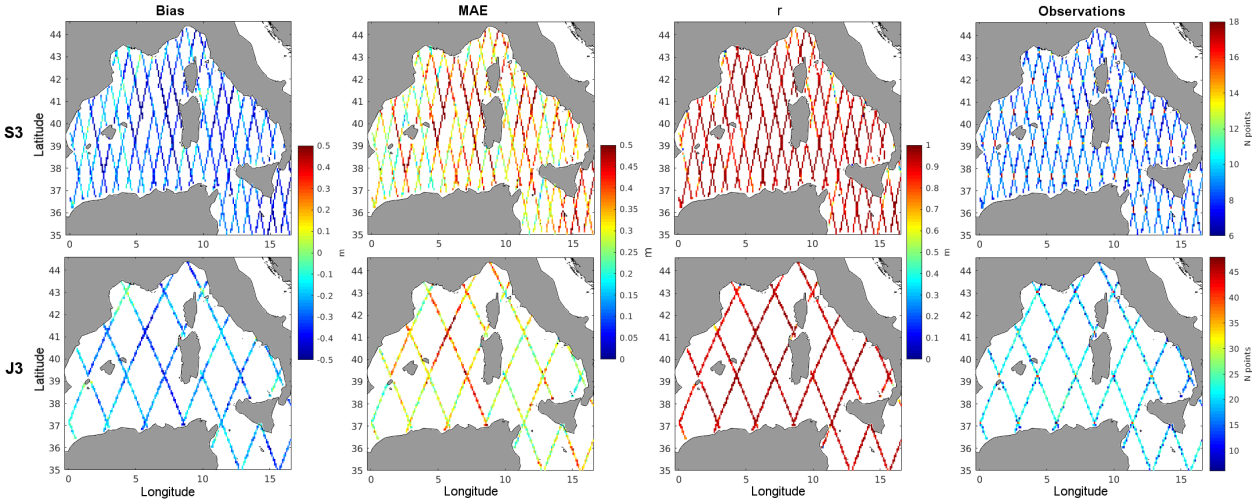

Figure 6.17: Spatial distribution of bias, MAE and r comparing the predicted Hs (form MED domain and DAY 1 forecasting range) with S3A (top) and J3 (bottom) data. The number of observations at each location is also presented.

Finally, the forecasted Hs is validated by means of the wave alert system verification method used at the SMC. In Figure 6.18 the number of days where Level 1 and Level 2 have been surpassed at each buoy location is presented (according to the buoy measurements from 15 March 2017 to 15 March 2018). As expected after Figure 6.10, *begur* and *mahon* buoys were the ones that registered more events, followed by *drago*, and *ttarr* and *tbarc* buoys together only registered 3 Level 1 events. In order to synthesize, just the results at the three locations that have measured more events (*begur*, *mahon* and *drago*) are presented below.

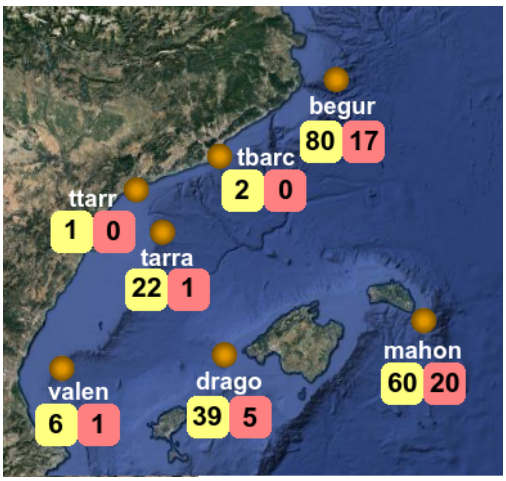

Figure 6.18: Number of days where Level 1 (in yellow) and Level 2 (in red) have been surpassed.

The contingency table and the alert statistics at *begur* are shown in Tables 6.10 and 6.11, respectively. In Table 6.10 it is observed that, three days in advance, the numerical model is able to predict 65 Level 1 events and 14 Level 2 events from the 80 and 17 observed events, respectively. As the wave storm events approach, one day in advance, the predicted Level 1 and Level 2 events increase up to 70 and 15, respectively, and the number of errors decrease but the false alarms increase. These results are also observed in Table 6.11, where the POD and FAR values are higher for DAY 1 forecasting range than for DAY 3 forecasting range.

Table 6.10: Contingency table at *begur*.

	DAY 1			**DAY 2**			**DAY 3**		
	F < 2.5	**2.5<F<4**	**F > 4**	**F < 2.5**	**2.5<F<4**	**F > 4**	**F < 2.5**	**2.5<F<4**	**F > 4**
O < 2.5	222	32	0	227	27	0	230	24	0
2.5<O<4	8	70	2	16	61	3	14	65	1
O > 4	0	2	15	0	1	16	0	3	14

Table 6.11: Alert statistics at *begur*.

	DAY 1				**DAY 2**				**DAY 3**			
	Bias	POD	FAR	CSI	Bias	POD	FAR	CSI	Bias	POD	FAR	CSI
Level 1	1.25	0.92	0.26	0.69	1.11	0.84	0.25	0.65	1.10	0.86	0.22	0.69
Level 2	1.00	0.88	0.12	0.79	1.12	0.94	0.16	0.80	0.88	0.82	0.07	0.78
	Accuracy = 65.89 %				Accuracy = 62.10 %				Accuracy = 65.29 %			

The results at the *drago* buoy location are presented in Tables 6.12 and 6.13. Unlike the previous case, in this case the false alarms diminish for DAY 1 forecasting range. Comparing from three to one day in advance, the model is able to increase the Level 1 event hits but the Level 2 event hits diminish from 2 to 1, leading to 4 underestimation errors from the whole 5 measured events. This results in good statistics for Level 1 events and not so good results for Level 2 events.

Table 6.12: Contingency table at *drago*.

	DAY 1			**DAY 2**			**DAY 3**		
	F < 2.5	**2.5<F<4**	**F > 4**	**F < 2.5**	**2.5<F<4**	**F > 4**	**F < 2.5**	**2.5<F<4**	**F > 4**
O < 2.5	297	4	0	295	6	0	293	8	0
2.5<O<4	9	30	0	12	27	0	14	24	1
O > 4	0	4	1	0	5	0	0	3	2

Table 6.13: Alert statistics at *drago*.

	DAY 1				DAY 2				DAY 3			
	Bias	POD	FAR	CSI	Bias	POD	FAR	CSI	Bias	POD	FAR	CSI
Level 1	0.89	0.80	0.10	0.73	0.86	0.73	0.16	0.64	0.86	0.68	0.21	0.58
Level 2	0.20	0.20	0.00	0.20	0	0	-	0	0.60	0.40	0.33	0.33
	Accuracy = 64.58 %				Accuracy = 54.00 %				Accuracy = 50.00 %			

Lastly, Tables 6.14 and 6.15 show the results obtained at the *mahon* buoy location. In this case, the Level 1 event alerts are slightly worse for DAY 1 forecasting range than form DAY 3 forecasting range, with the POD going from 0.74 to 0.71, respectively. In contrast, the Level 2 event alerts improve as the event becomes nearer in time, with a POD of 0.60.

Table 6.14: Contingency table at *mahon*.

	DAY 1			DAY 2			DAY 3		
	F < 2.5	**2.5<F<4**	**F > 4**	**F < 2.5**	**2.5<F<4**	**F > 4**	**F < 2.5**	**2.5<F<4**	**F > 4**
O < 2.5	224	3	0	224	3	0	220	7	0
2.5<O<4	22	38	0	21	38	1	20	39	1
O > 4	1	7	12	1	9	10	1	10	9

Table 6.15: Alert statistics at *mahon*.

	DAY 1				DAY 2				DAY 3			
	Bias	POD	FAR	CSI	Bias	POD	FAR	CSI	Bias	POD	FAR	CSI
Level 1	0.75	0.71	0.05	0.69	0.76	0.73	0.05	0.70	0.83	0.74	0.11	0.68
Level 2	0.60	0.60	0.00	0.60	0.55	0.50	0.09	0.48	0.50	0.45	0.10	0.43
	Accuracy = 60.24 %				Accuracy = 57.83 %				Accuracy = 55.17 %			

Regarding the *Accuracy* parameter, the best results are obtained at *begur* location, with more than 60% of successfully warned alerts. The worst calculated *Accuracy* is 50% (forecasting range DAY 3 at *drago*), which means that only half of the events have been successfully warned.

4 Discussion and Future Works

At the start of the forecasting system design, the necessity of coupling or not the SWAN and ROMS numerical models was posed. In Chapter V the wave–current interactions (WCIs) at the north Ebro Shelf have been analyzed and, although it has been proved that waves have an effect on the current field and vice versa, the differences observed between coupled and uncoupled systems would not be very significant, for example, in a decision making process or an early warning system. From a scientific point of view, it is interesting to analyze the WCIs in order to understand and know the phenomena that occur in the study area but when one wants to design a forecasting system one has to analyze if the computational effort of implementing a coupled system is worth it or not. As a matter of fact, Pallares (2016) showed that, at the Catalan coast, introducing the current fields into the wave model is only interesting when the magnitude of the current is one order of magnitude higher than usual (around 100 cm/s). Renault et al. (2012) analyzed the effects of including waves in the simulation of a storm event with winds up to 25 m/s that generated significant wave heights up to 5 m and found that using a fully-coupled system provided the most skillful results. Such conditions are very unusual at the study area and thus, having an operative coupled system would just be relevant during very few specific events. For this reason, it was considered that the priority was to have a reliable forecasting system run with affordable computational costs without considering the WCI. In the future, it could be interesting to analyze the WCI effects during those strong episodes where the WCIs might be relevant and study the frequency of such events. With this information in hand, if it were considered that such events are frequent enough and the WCIs were considered relevant, a possible solution would be to design a system that runs uncoupled by default but that is switched to a coupling mode when an event where the WCIs could be relevant is predicted.

Focusing on the skill assessment results presented in Section 3, the scarcity of measurements makes the skill assessment rather difficult, specially in the water currents case. However, both ROMS and SWAN models show good agreement with the available measurements and are considered reliable. The wave and currents forecasting systems are now running every day and their results are being monitored to carry out a tracing. This follow-up will permit a more exhaustive validation focused on the work to enhance the numerical model results. Currently, work is being done on changing the 5 coastal ROMS domains into a unique domain along the Catalan coast in order to avoid overlapping results and enlarge the area covered by the coastal domains. In addition, a coastal approachment of the wave forecasting is being designed, implementing the SWAN model at high resolution coastal domains and including processes such as depth-induced breaking and triad wave–wave interactions.

Finally, it is worth noting the wave alert verification methodology. The fact of basing the alert

verification calculus on the daily maximum values can lead to more false alarms and errors than the ones that have actually happened. For example, if a wave storm peak is measured at 00:00 h of one day and the numerical model predicts the peak at 23:00 h of the previous day, this verification methodology will see this as an error, but the wave event was predicted with just a temporal displacement of one hour. Such case would be a very specific case but a more frequent case could be to predict accurately the storm peak during one day and a faster decay during the next day than the measured storm. In Figure 6.19 two clear examples of this situation are observed (on 31 October and 2 March). The figure shows the Hs time series at *begur*, the calculated daily maximums and the errors and false alarms detected for DAY 1 forecasting range. In addition, when an event is undepredicted (overpredicted) and lasts more than one day, the error (false alarm) is multiplied (e.g. 6 – 8 January (19 – 22 January)). In the future, it would be interesting to improve this methodology and design a system based on measured and predicted events rather than in daily maximums and taking into account more parameters besides Hs, such as Tp, Dir, ssh and total energy, among others.

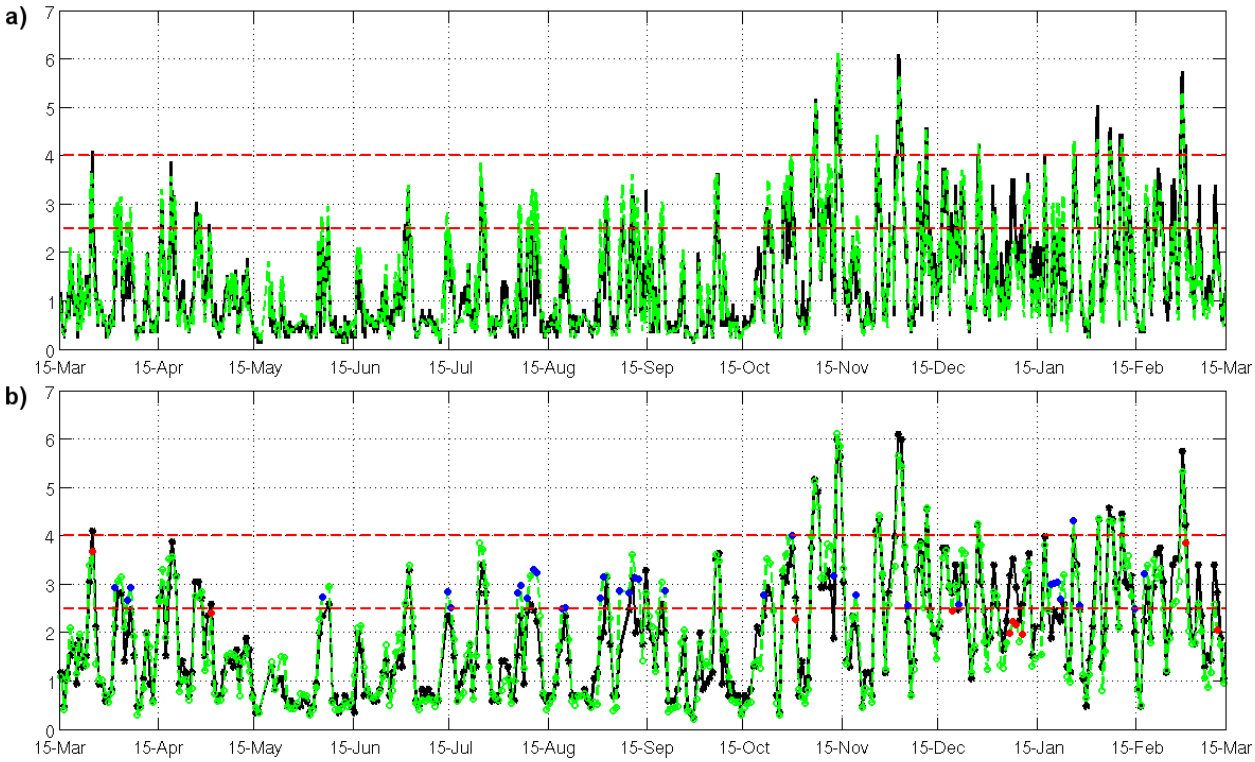

Figure 6.19: a) Modeled (in green) and measured (in black) Hs time series at *begur*. b) Daily maximums computed to generate the wave alerts. The blue circles correspond to false alarms and the red circles are forecasting errors. The results correspond to DAY 1 forecasting range and the red horizontal dashed lines are the Level 1 and Level 2 wave alert thresholds.

5 Conclusions

A wave forecasting system and a water current forecasting system have been implemented at the SMC. The numerical results have been validated using in-situ buoy measurements, HF radar data and satellite data, showing rather good agreement. Both systems are currently running everyday, providing sea state forecasting results along the Catalan coast with a forecasting horizon of 72 h. Besides, the numerical results are being collected in order to perform analysis of the data to enhance our knowledge on the water dynamics at the region. Overall, the validation results are encouraging but the scarcity of measurements causes the validation to be based on a rather qualitative analysis. For this reason, in order to be able to determine the reliability of the system, it is important to have a good knowledge of the water dynamics at the study region. In addition, the system monitoring will be focused on finding potential key improvements of the system in order to enhance the forecasting results and keep the system updated with the state of the art techniques and formulations.

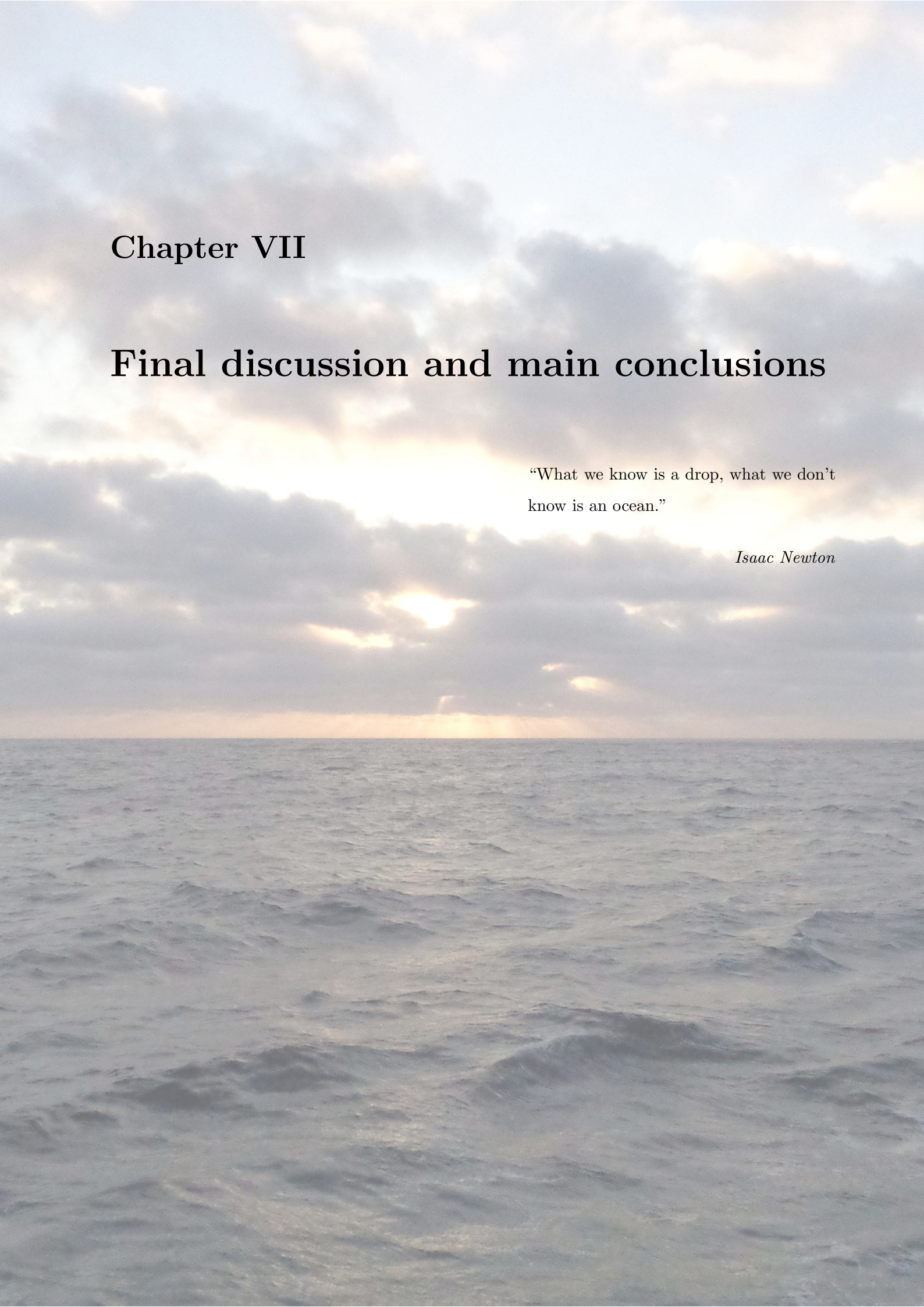

Chapter VII

Final discussion and main conclusions

"What we know is a drop, what we don't know is an ocean."

Isaac Newton

1 General discussion

The main objective of this thesis was to investigate the waves and ocean dynamics at the Catalan coast by means of numerical models. Most of the study has been focused at the north Ebro Shelf (NES) due to two main reasons. On the one hand, it is a wind-jet region, which makes it an interesting study area due to the wind jet influence on the wind-wave generation and the circulation patterns. On the other hand, the available water current measurements along the Catalan coast is very scarce and the presence of a HF radar at the Ebro Delta makes this region the most appropriate to calibrate and validate the numerical model. Then, with the knowledge gained from this investigation at the NES, an operational forecasting system of waves and currents at the Catalan coast has been implemented.

The waves and ocean dynamics at the NES have been investigated separately: first the hydrodynamic response to wind jets, then the wave field induced by wind jets and, finally, the effects of currents on waves and vice versa.

Regarding the hydrodynamic response to a wind jet, in Chapter III, results from a 6-months ROMS simulation have been used to investigate the water circulation at the NES. The results show that the sea-surface elevation undergoes a sea-level set-down throughout the wind jet. The along-shelf water current at deep regions shows a divergence zone east of the wind-jet axis and a convergence to its west, which is consistent with the Pond and Pickard (1983) theoretical study. The cross-shelf water current response to a wind jet show an upwelling zone near the coastline linked to a two-layer flow structure (offshoreward flow at the near-surface and onshoreward flow in deeper layers). This two-layer structure was also observed in previous works, such as Tilburg (2003), Fewings et al. (2008), Horwitz and Lentz (2014) and Grifoll et al. (2015). Previous studies present differences when establishing the influence of the stratification in the cross-shelf transport (Tilburg, 2003; Dzwonkowski et al., 2011; Lentz and Fewings, 2012; Grifoll et al., 2015). The results presented in this work show that the more stratified the water column, the thinner the SML and the SBL, leading to a reduction of the inner shelf region. Additionally, it has been found that the wind stress plays a smaller role when the SML depth is higher, because the affected water column is bigger and thus the stratification plays a major role. Lastly, following the distinct inner and mid-shelf response to cross-shelf winds of Lentz and Fewings (2012), the cross-shelf momentum balance analysis performed in this study has allowed to discern the different shelf regions during a wind-jet event depending on the main balancing terms: points located at the inner shelf present a balance between the pressure gradient and the surface stress terms; points at the mid-shelf show a balance between the Coriolis force and the surface stress terms; places where a combined balance between the Coriolis force, the pressure gradient and the surface stress terms are considered to be in a

transition region; and the regions that are not affected by the wind jet are in geostrophic balance.

Regarding the wind-jet effects on waves, in Chapter IV, results from a 2-months SWAN simulation have been used to investigate the wind-wave characterization at the NES. This 2-months study period is comprised in the 6 months study period used in Chapter III and includes four of the nine wind-jet events selected in the latter. It is important to remark that it is the first time that the temporal and spatial wave spectra evolution has been analyzed at the Ebro Delta. This analysis has shown that bimodal spectra occur at the start and the end of a wind jet. These bimodal spectra are developed due to the coexistence of NW wind at the Ebro Delta, associated with the wind-sea system, and northerly wind at the northern part of the coast that generates waves propagating to the south that are then diffracted to the east and reach the Ebro Delta as a swell system. It has also been observed that a wind turn of $\sim 90^{\circ}$ is able to develop a bimodal spectrum (similar to Young et al. (1987)). Following the work done by Shimada and Kawamura (2006), the directional spreading has also been analyzed and it has been found that it is lower at the wind-jet axis (of the order of $\sim 40^{\circ}$) than out of it. The results have shown that the wave directional spreading is negatively correlated with the wind intensity, while the Hs presents a positive correlation with it. Since the Ebro Delta HF radar provides wave data but no previous works have used them, the reliability of the wave measurements has been investigated. The HF radar raw data needs to be post-processed in order to be used. With this aim, a method combining the methods in Long et al. (2011) and Atan et al. (2016) has been used. The wave HF radar data has demonstrated to have a rather good quality and have proved to be able to capture the wave height tendency. However the time series are full of gaps and, since the measures are considered constant along a whole range cell, they are not reliable to validate a short-duration specific event in a region where the wave field is quite heterogeneous.

Regarding the wave–current interactions, in Chapter V, results from uncoupled ROMS and SWAN simulations have been compared with a coupled simulation in order to evaluate the effects of currents on the wave field and vice versa. In this case, the study period is the same one as the study period analyzed in Chapter IV. First, it is important to note that, although there are some previous studies about the current patters and the wave field at the NES, less efforts have been done in analyzing the WCIs in the region. The results have shown that the effects of waves on the current field during a wind-jet event is weak, being the major influence detected in the vertical mixing of the water column, which is enhanced when the waves are taken into account. This fact is consistent with the previous studies done by Rong et al. (2014), Bruneau and Toumi (2016) and (Niu and Xia, 2017). In contrast, the effect of water currents on the wave field has demonstrated to have a higher impact. When the water currents are considered, the Tm_{02} parameter is remarkably improved (with an average effect of 48% at deep regions). Although less affected, the Hs parameter has also

proved to be modified by the water currents, being decreased during a wind jet. This decrease is explained by the decrease of Hs in the presence of a following current observed before in several studies (Benetazzo et al., 2013; Dutour Sikirić et al., 2013; Viitak et al., 2016). In addition, the presence of currents produces a shoaling-like process that leads to a wave spectral reshaping, with a reduction of the energy peak and a slight increase of the energy at the tail of the spectrum. Finally, it is worth noting that the results have indicated that more effects occur at shallower regions. For instance, the momentum balance analysis has shown that the term related to the wave forces is one of the leading terms in very shallow areas and the differences observed in the wave direction near the coastline might be due to the current-refraction phenomenon. However, in order to further analyze these effects, a more coastal domain at higher resolution should be used.

So far, the ROMS and SWAN numerical model implementations used to investigate the waves and the circulation at the NES have demonstrated to perform rather well, presenting good agreement with measured data. For this reason, in Chapter VI, the knowledge gained so far has been used to implement an operational forecasting system at the Catalan coast in the SMC's calculus machines. On the one hand, the waves forecasting system consists in two nested domains, with a horizontal resolution of 11 km and 3 km, respectively. On the other hand, the hydrodynamics forecasting system consists in five coastal domains (each with a horizontal resolution of 400 m) that use the IBI-MFC data as boundary conditions. Both systems use meteorological data from the SMC operative WRF model. The scarcity of measured data along the Catalan coast does not allow to perform an exhaustive validation of the systems but the comparison with the available buoy measurements, the HF radar data at the Ebro Delta and the wave satellite data from Jason-3 and Sentinel-3A, has proven that the forecasting results agree fairly well with the measurements and show reliable patterns. In this sense, more efforts should be done in installing buoys or performing field campaigns along the Catalan coast in order to be able improve the calibration and validation of the numerical models. Currently, both models are running every day and their results are being analyzed in order to find potential actions that could allow an improvement of the forecasting systems.

2 Final conclusions

The final conclusions of this thesis can be grouped according to the established objectives:

1. **Study the local circulation induced by a wind jet**.
   - The cross-shelf circulation at the wind-jet axis presents a well-defined two-layer structure, with an offshore flow at near-surface and an onshore flow in deeper layers.
   - A decrease of the sea level near the coast and upwelling near the coastline occur.
   - The vertical structure of the water column highly depends on the wind stress and the water stratification. Increasing the stratification reduces the SML and the SBL, thus the inner shelf region is narrower.
   - During the warmer episodes, the water column presents a stratification reduction but, due to its initially higher stratification, it remains stratified after the wind jet.
   - During colder episodes, the wind momentum transfer penetrates unto deeper layers and the whole water column becomes mixed after the wind jet.
   - The cross-shelf momentum balance allow to discern between the different continental shelf regions. At the inner shelf, the balance is between the pressure gradient and the surface stress terms, at the mid-shelf the balance is between the Coriolis force and the surface stress terms, there are transition zones with a combined balance between the Coriolis, the surface stress and the pressure gradient terms and there are regions that are not affected by the wind jet and show a geostrophic balance.
2. **Study the effect of wind jets on waves**.
   - The significant wave height presents a positive correlation with the wind intensity and shows a spatial distribution in accordance with the wind field.
   - The wave directional spreading presents a negative correlation with the wind intensity, resulting in a lower wave dispersion at the wind-jet axis. There are also differences of wave directional spreading along the wind-jet axis, being higher in the nearshore zone.
   - During the wind-jet event the spectrum is unimodal (due to a wind-sea system), with the wave direction matching with the wind direction.
   - At the start and the end of the wind jet a bimodal spectrum occur, with the coexistence of sea and swell systems.
   - Bimodal spectra are very common in the region due to the synoptic conditions that induce the NW wind jets. These are usually accompanied by northerly winds at the north of the Catalan coast, which produce the swell system at the Ebro Delta.

- The HF radar wave time series are full of gaps and are not useful for studying the evolution of a short-duration specific event. Additionally, the samples are homogeneous along a range cell so, if the region presents big wave gradients, the HF radar data could be measuring something very different than the typical buoy data to which the authors are accustomed.

3. **Study the wave–current interactions under wind-jet conditions**.

   - The water current field presents similar results in the coupled and the uncoupled configurations.
   - The momentum balance analysis reveals that the non-conservative wave forcing term plays an important role in shallow waters.
   - Including wave effects induces major mixing of the water column (the SML increase), mainly due to the TKE injection and the enhanced surface stress.
   - When the water currents are considered, wave spectral reshaping occurs, the Tm_{02} improves and the wave energy (and thus the Hs) diminishes (increases) when the water currents and waves propagate in the same (opposite) direction.
   - The results also indicate that more processes occur in shallower waters.

4. **Implement an operational system**.

   - Waves and currents forecasting systems have been implemented at the SMC and are currently running every day.
   - In spite of the scarcity of available measurements, the validation shows encouraging results.
   - The forecasting results are being collected in order to find potential improvements and improve the knowledge of waves and water current dynamics of the region.
   - Some future works have been pointed out in order to keep working with the improvement of the implemented forecasting system.

Bibliography

Aijaz, S., Rogers, W., and Babanin, A. (2016), Wave response to sudden changes in wind direction in finite-depth waters, *Ocean Modelling*, *103*, 98–177, doi:10.1016/j.ocemod.2015.11.006.

Alomar, M., Sánchez-Arcilla, A., Bolaños, R., and Sairouni, A. (2014), Wave growth and forecasting in variable, semi-enclosed domains, *Continental Shelf Research*, *87*, 28–40, doi:10.1016/j.csr.2014.05.008.

Atan, R., Goggins, J., Harnett, M., and Agostinho, P. (2016), Assessment of wave characteristics and resource variability at a 1/4-scale wave energy test site in galway bay using waverider and high frequency radar (codar) data, *Ocean Engineering*, *117*, 272–291, doi:http://dx.doi.org/10.1016/j.oceaneng.2016.03.051.

Benetazzo, A., Carniel, S., Scalvo, M., and Bergamasco, A. (2013), Wave-current interaction: Effect on the wave field in a semi-enclosed basin, *Ocean Modelling*, *70*, 152–165, doi:10.1016/j.ocemod.2012.12.009.

Bolaños, R., Jorda, G., Cateura, J., Lopez, J., Puigdefabregas, J., Gomez, J., and Espino, M. (2009), The xiom: 20 years of a regional coastal observatory in the spanish catalan coast, *Journal of Marine Systems*, *77*, 237–260, doi:10.1016/j.jmarsys.2007.12.018.

Bolaños, R., Osuna, P., Wolf, J., Monbaliu, J., and Sánchez-Arcilla, A. (2011), Development of POLCOMS-WAM model, *Ocean Modelling*, *36*(1-2), 102–115, doi:10.1016/j.ocemod.2010.10.004.

Bolaños, R., Brown, J., and Souza, A. (2014), Wave-current interactions in a tide dominated estuary, *Continental Shelf Research*, *87*, 109–123, doi:10.1016/j.csr.2014.05.009.

Bolaños-Sanchez, R., Sánchez-Arcilla, A., and Cateura, J. (2007), Evaluation of two atmospheric models for wind-wave modelling in the NW mediterranean, *Journal of Marine Systems*, *65*, 336–353, doi:10.1016/j.jmarsys.2005.09.014.

Booij, N., Ris, R., and Holthuijsen, L. (1999), A third-generation wave model for coastal regions - 1. Model description and validation, *Journal of Geophysical Research*, *104*, 7649–7666, doi:10.1029/98JC02622.

Bretherton, F., and Garrett, C. (1968), Wavetrains in Inhomogeneous Moving Media, *Proceedings of the Royal Society of London. Series A, Mathematical and Physical Sciences*, *302*(1471), 529–554, URL `http://www.jstor.org/stable/2415989`.

Bruneau, N., and Toumi, R. (2016), A fully-coupled atmosphere-ocean-wave model of the Caspian Sea, *Ocean Modelling*, *107*, 97–111, doi:10.1016/j.ocemod.2016.10.006.

Cavaleri, L., and Bretotti, L. (2004), Accuracy of the modelled wind and wave fields in enclosed seas, *Tellus*, *56 A*, 167–175, doi:10.1111/j.1600-0870.2004.00042.x.

Cavaleri, L., and Malanotte-Rizzoli, P. (1981), Wind wave prediction in shallow water: Theory and applications, *Journal of Geophysical Research*, *86*, 961–973, doi:10.1029/JC086iC11p10961.

Csanady, G. (1980), Longshore pressure gradients caused by offshore wind, *Journal of Geophysical Research*, *85*(C2), 1076–1084, doi:10.1029/JC085iC02p01076.

Durand, N., Fiandrino, A., Frauni, P., Ouillon, S., Forget, P., and Naudin, J. (2002), Suspended matter dispersion in the Ebro ROFI: An integrated approach, *Continental Shelf Research*, *22*, 267–284, doi:10.1016/S0278-4343(01)00057-7.

Dutour Sikirić, M., Roland, A., Janeković, I., Tomažić, I., and Zumić, M. (2013), Coupling of the Regional Ocean Modeling System (roms) and Wind Wave Model, *Ocean Modelling*, *72*, 59–73, doi:10.1016/j.ocemod.2013.08.002.

Dzwonkowski, B., Park, K., and Jiang, L. (2011), Subtidal across-shelf velocity structure and surface transport effectiveness on the alabama shelf of the northeastern gulf of mexico, *Journal of Geophysical Research*, *116*(C10012), doi:10.1029/2011JC007188.

Ekman, V. (1905), On the Influence of the Earth's Rotation on Ocean-Currents, *Arkiv for Matematik, Astronomi Och Fysik*, *2*(11), 1–53.

Espino, M., Sánchez-Arcilla, A., and García, M. (1998), Wind-induced mesoscale circulation off the Ebro delta, NW Mediterranean: a numerical study, *Journal of Marine Systems*, *16*, 235–251, doi:10.1016/S0924-7963(97)00110-3.

Fairall, C., Bradley, E., Rogers, D., Edson, J., and Young, G. (1996), Bulk parameterization of air-sea fluxes for tropical ocean-global atmosphere Coupled-Ocean Atmosphere Response Experiment, *Journal of Geophysical Research*, *101*, 3747–3764, doi:10.1029/95JC03205.

Fan, Y., Ginis, I., Hara, T., Wright, C., and Walsh, E. (2009), Numerical Simulations and Observations of Surface Wave Fields under an Extreme Tropical Cyclone, *Journal of Physical Oceanography*, *39*, 2097–2116, doi:10.1175/2009JPO4224.1.

Fewings, M., and Lentz, S. (2010), Momentum balances on the inner continental shelf at Martha's Vineyard Coastal Observatory, *Journal of Geophysical Research*, *115*(C12023), doi: 10.1029/2009JC005578.

Fewings, M., Lentz, S., and Fredericks, J. (2008), Observations of Cross-Shelf Flow Driven by Cross-Shelf Winds on the Inner Continental Shelf, *Journal of Physical Oceanography*, *38*, 2358–2378, doi:10.1175/2008JPO3990.1.

Flexas, M., Durrieu de Madron, X., Garcia, M., Canals, M., and Arnau, P. (2002), Flow variability in the Gulf of Lions during the MATER HFF experiment (March-May 1997), *Journal of Marine Systems*, *33-34*, 197–214, doi:10.1016/S0924-7963(02)00059-3.

Font, J. (1986), La circulación general a la mar catalana, Ph.D. thesis, Universitat de Barcelona.

Font, J., Salat, J., and Tintoré, J. (1988), Permanent features of the circulation in the Catalan Sea, *Oceanologia Acta*, *9*, 51–57, URL `http://archimer.ifremer.fr/doc/00267/37808/`.

Font, J., Garcia-Ladona, E., and Gorriz, E. (1995), The seasonality of mesoscale motion in the Northern Current of the western Mediterranean: several years of evidence, *Oceanologia Acta*, *18*(2), 207–219, URL `http://archimer.ifremer.fr/doc/00096/20772/`.

García, M., Arnau, P., and Sánchez-Arcilla, A. (1998), Advection of anticyclonic eddies across the Blanes canyon, NW Mediterranean, *Rapports de la Commission Internationale pour l'exploitation Scientific de la Mer Méditerranée*, *35*(1), 142–143.

Graber, H., and Haus, B. (1997), HF radar comparisons with moored estimates of current speed and direction: Expected differences and implications, *Journal of Geophysical Research*, *102*(C8), 18,749–18,766, doi:10.1029/97JC01190.

Grifoll, M., Aretxabaleta, A., Pelegrí, J., Espino, M., Warner, J., and Sánchez-Arcilla, A. (2013), Seasonal circulation over the Catalan inner-shelf (northwest Mediterranean Sea), *Journal of Geophysical Research: Oceans*, *118*, 5844–5857, doi:10.1002/jgrc.20403.

Grifoll, M., Aretxabaleta, A., and Espino, M. (2015), Shelf response to intense offshore wind, *Journal of Geophysical research: Oceans*, *120*, 6564–6580, doi:10.1002/2015JC010850.

Grifoll, M., Navarro, J., Pallares, E., Ràfols, L., Espino, M., and Palomares, A. (2016a), Ocean-atmosphere-wave characterisation of a wind jet (Ebro shelf, NW Mediterranean Sea), *Nonlinear Processesin Geophysics*, *23*, 143–158, doi:10.5194/npg-23-143-2016.

Grifoll, M., Aretxabaleta, A., Pelegrí, J., and Espino, M. (2016b), Temporal evolution of the momentum balance terms and frictional adjustment observed over the inner shelf during a storm, *Ocean Science*, *12*, 137–151, doi:10.5194/os-12-137-2016.

Haidvogel, D., Arango, H., Budgell, W., Cornuelle, B., Curchitser, E., Lorenzo, E. D., Fennel, K., Geyer, W., Hermann, A., Lanerolle, L., Levin, J., McWilliams, J., Miller, A., Moore, A., Powell, T., Shchepetkin, A., Sherwood, C., Singell, R., Warner, J., and Wilkin, J. (2008), Ocean forecasting in terrain-following coordinates: Formulation and skill assessment of the Regional Ocean Modeling System, *Journal of Computational Physics*, *227*, 3595–3624, doi:10.1016/j.jcp.2007.06.016.

Hanson, J., and Phillips, O. (2001), Automated Analysis of Ocean Surface Directional Wave Spectra, *Journal of Atmospheric Oceanic Technology*, *18*, 277–293, doi:10.1175/1520-0426(2001)018⟨0277:AAOOSD⟩2.0.CO;2.

Hasselmann, K., Barnett, T., Bouws, E., Carlson, H., Cartwright, D., Enke, K., Ewing, J., Gienapp, H., Hasselmann, D., Kruseman, P., Meerburg, A., Müller, P., Olbers, D., Richter, K., Sell, W., and Walden, H. (1973), Measurements of wind-wave growth and swell decay during the Joint North Sea Wave Project (JONSWAP), *Tech. Rep. 12*, Deutches Hydrographisches Institut.

Hasselmann, S., Hasselmann, K., Allender, J., and Branett, T. (1985), Computations and parameterizations of the nonlinear energy transfer in a gravity wave spectrum. Part II: parameterizations of the nonlinear transfer for application in wave models., *Journal of Physical Oceanography*, *15*, 1378–1391, doi:10.1175/1520-0485(1985)015⟨1378:CAPOTN⟩2.0.CO;2.

Horwitz, R., and Lentz, S. (2014), Inner-shelf response to cross-shelf wind stress: The importance of the cross-shelf density gradient in an idealized numerical model and field observations, *Journal of Physical Oceanography*, *44*, 86–103, doi:10.1175/JPO-D-13-075.1.

ICGC (2010), Llibre verd de l'estat de la zona costanera a catalunya, 2010, generalitat de Catalunya.

Jacob, R., Larson, J., and Ong, E. (2004), M x n communication and Parallel Interpolation in CCSM using the Model Coupling Toolkit, Preprint ANL/MCS-P1225-0205, Mathematics and Computer Science Division, Argonne National Laboratory.

Janssen, P. (1991), Quasi-linear theory of wind generation applied to wave forecasting, *Journal of Physical Oceanography*, *21*, 1631–1642, doi:10.1175/1520-0485(1991)021⟨1631:QLTOWW⟩2.0.CO;2.

Jenkins, A. (1987), Wind and wave induced currents in a rotating sea with depth-varying eddy viscosity, *Journal of Physical Oceanography*, *17*, 938–951, doi:10.1175/1520-0485(1987)017⟨0938:WAWICI⟩2.0.CO;2.

Jiang, H., Farrar, J., Beardsley, R., Chen, R., and Chen, C. (2009), Zonal surface wind jets across the Red Sea due to mountain gap forcing along both sides of the Red Sea, *Geophysical Research Letters*, *36*(L19605), doi:10.1029/2009GL040008.

Jimenez, J., Sancho-García, A., Bosom, E., Valdemoro, H., and Guillén, J. (2012), Storm-induced damages along the Catalan coast (NW Mediterranean) during the period 1958-2008, *Geomorphology*, *143-144*, 24–33, doi:10.1016/j.geomorph.2011.07.034.

Jordà, G. (2005), Towards data assimilation in the Catalan continental shelf, Ph.D. thesis, Universitat Politècnica de Catalunya, Barcelona, Spain.

Jorda, G., Bolaños, R., Espino, M., and Sánchez-Arcilla, A. (2007), Assessment of the importance of the current-wave coupling in the shelf ocean forecasts, *Ocean Science*, *3*, 345–362, doi:10.5194/os-3-345-2007.

Kirby, J., and Chen, T.-M. (1989), Surface waves on vertically sheared flows: approximate dispersion relations, *Journal of Geophysical Research*, *94*, 1013–1027, doi:10.1029/JC094iC01p01013.

Kohut, J., Roarty, H., Licthenwalner, S., Glenn, S., Barrick, D., Lipa, B., and Allen, A. (2008), Surface current and wave validation of a nested regional HF radar Network in the Mid-Atlantic Bight, in *2008 IEEE/OES 9th Working Conference on Current Measurement Technology*, pp. 203–207, doi:10.1109/CCM.2008.4480868.

Komen, G., Hasselmann, S., and Hasselmann, K. (1984), On the existence of a fully developed wind-sea spectrum, *Journal of Physical Oceanography*, *14*, 1271–1285, doi:10.1175/1520-0485(1984)014⟨1271:OTEOAF⟩2.0.CO;2.

Kuik, A., Van Vledder, G., and Holthuijsen, L. (1988), A Method for the Routine Analysis of Pitch-and-Roll Buoy Wave Data, *Journal of Physical Oceanography*, *18*, 1020–1034, doi:10.1175/1520-0485(1988)018⟨1020:AMFTRA⟩2.0.CO;2.

Kumar, N. (2013), Measurement and Three-Dimensional Modeling of Hydrodynamic Processes In the Inner Shelf and Surf Zone, Ph.D. thesis, University of South Carolina.

Kumar, N., Voulgaris, G., Warner, J., and Olabarrieta, M. (2012), Implementation of the vortex force formalism in the coupled ocean-atmosphere-wave-sediment transport (COAWST) modeling system for inner shelf and surf zone applications, *Ocean Modelling*, *47*, 65–95, doi:10.1016/j.ocemod.2012.01.003.

La Violette, P., Tintoré, J., and Font, J. (1990), The surface circulation of the Balearic Sea, *Journal of Geophysical Research*, *95*(C2), 1559–1568, doi:10.1029/JC095iC02p01559.

Laface, V., Arena, F., and Guedes-Soares, C. (2015), Directional analysis of sea storms, *Ocean Engineering*, *107*, 45–53, doi:10.1016/j.oceaneng.2015.07.027.

Larson, J., Jacob, R., and Ong, E. (2004), The Model Coupling Toolkit: A new fortran90 toolkit for building parallel coupled models, Preprint ANL/MCS-P1208-1204, Mathematics and Computer Science Division, Argonne National Laboratory.

Lee, T., Ho, W., Kourafalou, V., and Wang, J. (1984), Circulation on the continental shelf of the southeastern United States. Part I: subtidal response to wind and gulf stream forcing during winter, *Journal of Physical Oceanography*, *14*, 1001–1012, doi:10.1175/1520-0485(1984)014⟨1001:COTCSO⟩2.0.CO;2.

Lentz, S. (1992), The surface boundary layer in coastal upwelling regions, *Journal of Physical Oceanography*, *22*, 1517–1539.

Lentz, S., and Fewings, M. (2012), The Wind- and Wave-Driven Inner-Shelf Circulation, *Annual Review of Marine Science*, *4*, 317–343, doi:10.1146/annurev-marine-120709-142745.

Lentz, S., Guza, R., Elgar, S., Feddersen, F., and Herbers, T. (1999), Momentum balances on the North Carolina Inner Shelf, *Journal of Geophysical Research*, *104*(C8), 205–226, doi:10.1029/1999JC900101.

Lipa, B., and Nyden, B. (2005), Directional Wave Information From the SeaSonde, *IEEE Journal of Oceanic Engineering*, *30*, 221–231, doi:10.1109/JOE.2004.839929.

Liu, Y., and Weisberg, R. (2005), Momentum balance diagnoses for the west florida shelf, *Continental Shelf Research*, *25*, 2054–2074, doi:10.1016/j.csr.2005.03.004.

Long, R., Barrick, D., Largier, J., and Garfield, N. (2011), Wave Observations from Central California: SeaSonde Systems and In Situ Wave Buoys, *Journal of Sensors*, *2011*, 1–18, doi:10.1155/2011/728936.

Lorente, P., Piedracoba, S., Soto-Navarro, J., and Alvarez-Fanjul, E. (2015), Evaluating the surface circulation in the Ebro delta (northeastern Spain) with quality-controlled high-frequency radar measurements, *Ocean Science*, *11*, 921–935, doi:10.5194/os-11-921-2015.

Lorente, P., Piedracoba, S., Sotillo, M., Aznar, R., Amo-Balandron, A., Pascual, A., Soto-Navarro, J., and Alvarez-Fanjul, E. (2016a), Characterizing the surface circulation in ebro delta (nw mediterranean) with hf radar and modeled current data, *Journal of Marine Systems*, *163*, 61–79, doi:10.1016/j.jmarsys.2016.07.001.

Lorente, P., Piedracoba, S., Sotillo, M., Aznar, R., Amo-Balandron, A., Pascual, A., Soto-Navarro, J., and Alvarez-Fanjul, E. (2016b), Ocean model skill assessment in the NW Mediterranean using multi-sensor data, *Journal of Operational Oceanography*, pp. 1–18, doi:10.1080/1755876X.2016.1215224.

Madsen, O. (1994), Spectral wave-current bottom boundary layer flows, in *Coastal Engineering 1994*, pp. 384–398, Proceedings of the 24th International Conference on Coastal Engineering, Kobe, Japan.

Masó, M., and Tintoré, J. (1991), Variability of the shelf water off the northeast Spanish coast, *Journal of Marine Systems,*, *1*, 441–450, doi:10.1016/0924-7963(91)90008-I.

McWilliams, J., Restrepo, J., and Lane, E. (2004), An asymptotic theory for the interaction of waves and currents in coastal waters, *Journal of Fluid Mechanics*, *511*, 135–178, doi:10.1017/S0022112004009358.

Mellor, G. (2003), The three-dimensional current and surface wave equations, *Journal of Physical Oceanography*, *33*(9), 1978–1989, doi:10.1175/1520-0485(2003)033⟨1978:TTCASW⟩2.0.CO;2.

Mellor, G. (2005), Some consequences of the three-dimensional current and surface wave equations, *Journal of Physical Oceanography*, *35*(11), 2291–2298, doi:10.1175/JPO2794.1.

Mellor, G. (2011), Reply, *Journal of Physical Oceanography*, *41*, 2013–2015, doi:10.1175/JPO-D-11-071.1.

Mestres, M., Sierra, J., Sánchez-Arcilla, A., González del Río, J., Wolf, T., Rodríguez, A., and Ouillon, S. (2003), Modelling of the Ebro River plume. Validation with field observations, *Scientia Marina*, *67*(4), 379–391, doi:10.3989/scimar.2003.67n4379.

Millero, F., and Poisson, A. (1981), International one-atmosphere equation of state of seawater, *Deep Sea Research Part A. Oceanographic Research Papers*, *28*(6), 625–629, doi:10.1016/0198-0149(81)90122-9.

Millot, C. (1987), Circulation in the Western Mediterranean Sea, *Oceanologica Acta*, *10*(2), 143–149, URL `http://archimer.ifremer.fr/doc/00108/21915/`.

Millot, C. (1999), Circulation in the Western Mediterranean Sea, *Journal of Marine Systems*, *20*, 423–442, doi:10.1016/S0924-7963(98)00078-5.

Niu, Q., and Xia, M. (2017), The role of wave-current interaction in Lake Erie's seasonal and episodic dynamics, *Journal of Geophysical Research: Oceans*, *122*, 7291–7311, doi:10.1002/2017JC012934.

O'Donncha, F., Hartnett, M., Nash, S., Ren, L., and Ragnoli, E. (2015), Characterizing observed circulation patterns within a bay using HF radar and numerical model simulations, *Journal of Marine Systems*, *142*, 96–110, doi:10.1016/j.jmarsys.2014.10.004.

Olabarrieta, M., Warner, J., and Kumar, N. (2011), Wave-current interaction in Willapa Bay, *Journal of Geophysical Research*, *116*(C12014), doi:10.1029/2011JC007387.

Osuna, P., and Monbaliu, J. (2004), Wave-current interaction in the Southern North Sea, *Journal of Marine Systems*, *52*, 65–87, doi:10.1016/j.jmarsys.2004.03.002.

Osuna, P., and Wolf, J. (2005), A numerical study on the effect of wave-current interaction processes in the hydrodynamics of the Irish Sea, in *Ocean Wave Measurement and Analysis, Fifth International Symposium WAVES*, Madrid, Spain, paper number: 93.

Ovchinnikov, I. (1966), Circulation in the surface and intermediate layers of the mediterranean, *Oceanology*, *6*, 48–59.

Pallares, E. (2016), High-resolution wave forecasting. The Catalan coast case. Modelling, coupling and validation, Ph.D. thesis, Universitat Plolitècnica de Catalunya.

Pallares, E., Sánchez-Arcilla, A., and Espino, M. (2014), Wave energy balance in wave models (SWAN) for semi-enclosed domains - Application to the Catalan coast, *Continental Shelf Research*, *87*, 41–53, doi:10.1016/j.csr.2014.03.008.

Pascual, A., Buongiorno Nardelli, B., Larnicol, G., Emelianov, M., and Gomis, D. (2002), A case of an intense anticyclonic eddy in the Balearic Sea (western Mediterranean), *Journal of Geophysical Research*, *107*(C11), doi:10.1029/2001JC000913.

Pawlowicz, R., Beardsley, B., and Lentz, S. (2002), Classical tidal harmonic analysis including error estimates in MATLAB using T-TIDE, *Computational Geosciences*, *28*, 929–937, doi:10.1016/S0098-3004(02)00013-4.

PDUSC (2004), Pla Director Urbanístic del Sistema Costaner, departament de Política Territorial i Obres Públiques, Generalitat de Catalunya.

Pollard, R., Rhines, P., and Thompson, R. (1972), The deepening of the wind-mixed layer, *Geophysical Fluid Dynamics*, *4*(1), 381–404, doi:10.1080/03091927208236105.

Ponce de León, S., and Guedes Soares, C. (2008), Sensitivity of wave model predictions to wind fields in the Western Mediterranean sea, *Coastal Engineering*, *55*, 902–929, doi:10.1016/j.coastaleng.2008.02.023.

Pond, S., and Pickard, G. (1983), *Introductory Dynamical Oceanography*, 2 ed., Butterworth-Heinemann.

Port, A., Gurgel, K., and Staneva, J. (2011), Tidal and wind-driven surface currents in the German Bight: HFR observations versus model simulations, *Ocean Dynamics*, *61*, 1567–1585, doi:0.1007/s10236-011-0412-9.

Ràfols, L., Grifoll, M., Jordà, G., Espino, M., Sairouní, A., and Bravo, M. (2017a), Shelf circulation induced by an orographic wind jet, *Journal of Geophysical Research: Oceans*, *122*, 8225–8245, doi:10.1002/2017JC012773.

Ràfols, L., Pallares, E., Espino, M., Grifoll, M., Sánchez-Arcilla, A., Bravo, M., and Sairouní, A. (2017b), Wind-Wave Characterization in a Wind-Jet Region: The Ebro Delta Case, *Journal of Marine Science and Engineering*, *5*(12), doi:10.3390/jmse5010012.

Ralston, D., Jiang, H., and Farrar, T. (2013), Waves in the Red Sea: Response to monsoonal and mountain gap winds, *Continental Shelf Research*, *65*, 1–13, doi:10.1016/j.csr.2013.05.017.

Renault, L., Chiggiato, J., Warner, J., Gomez, M., Vizoso, G., and Tintoré, J. (2012), Coupled atmosphere-ocean-wave simulations of a storm event over the Gulf of Lion and Balearic Sea, *Journal of Geophysical Research*, *117*(C09019), doi:10.1029/2012JC007924.

Riosalido, R., Vázquez, L., Gorgo, A., and Jansà, A. (1986), Cierzo: Northwesterly wind along the Ebro Valley as a meso-scale effect induced on the lee of the Pyrenees mountain range: a case study during ALPEX Special Observing Period, *Scientific Results of the Alpine Experiment (ALPEX)*, *2*(108), 565–575.

Rong, Z., Hetland, R., Zhang, W., and Zhang, X. (2014), Current-wave interaction in the Mississippi-Atchafalaya river plume on the Texas-Louisiana shelf, *Ocean Modelling*, *84*, 67–83, doi:10.1016/j.ocemod.2014.09.008.

Rusu, E. (2010), Modelling of wave-current interactions at the mouths of the Danube, *Journal of Marine Science Technology*, *15*(2), 143–159, doi:10.1007/s00773-009-0078-x.

Sánchez-Arcilla, A., González-Marco, D., and Bolaños, R. (2008), A review of wave climate and prediction along the Spanish Mediterranean coast, *Natural Hazards and Earth System Sciences*, *8*, 1217–1228, doi:10.5194/nhess-8-1217-2008.

Shchepetkin, A., and McWilliams, J. (2005), The regional oceanic modeling system (ROMS): a split-explicit, free-surface, topography-following-coordinate oceanic model, *Ocean Modelling*, *9*, 347–404, doi:10.1016/j.ocemod.2004.08.002.

Shimada, T., and Kawamura, H. (2006), Wind-wave development under alternating wind jets and wakes induced by orographic effects, *Geophysical Research Letters*, *33*(2), doi:10.1029/2005GL025241.

Skamarock, W., Klemp, J., Dudhia, J., Gill, D., Barker, D., Duda, M., Huang, X., Wang, W., and Powers, J. (2008), *A Description of the Advanceed Research WRF, Version 3*, NCAR Technical Note.

Suárez, J., and Rodríguez, J. (2007), *Atlas of the European Seas and Oceans*, ediciones del serbal: first ed., Spanish Ministry of Education and Science Project BSO2002-03576.

Svendsen, I. (1984), Wave heights and set-up in a surf zone, *Coastal Engineering*, *8*, 303–329, doi:10.1016/0378-3839(84)90028-0.

Svendsen, I., Haas, K., and Zhao, Q. (2002), *Quasi-3D nearshore circulation model SHORECIRC*, Center for Applied Coastal Researc, Department of Civil Engineering, University of Delaware, Newark, user's Manual, Draft Report.

Tang, C., Perrie, W., Jenkins, A., DeTracey, B., Hu, Y., Toulany, B., and Smith, P. (2007), Observation and modeling of surface currents on the Grand Banks: a study of the wave effects on surface currents, *Journal of Geophysical Research*, *112*, doi:10.1029/2006JC004028.

Taylor, P., and Yelland, M. (2001), The dependence of sea surface roughness on the height and steepness of the waves, *Journal of Physical Oceanography*, *31*, 572–590, doi:10.1175/1520-0485(2001)031⟨0572:TDOSSR⟩2.0.CO;2.

Tilburg, C. (2003), Across-Shelf Transport on a Continental Shelf: Do Across-Shelf Winds Matter?, *Journal of Physical Oceanography*, *33*, 2675–2688, doi:10.1175/1520-0485(2003)033⟨2675:ATOACS⟩2.0.CO;2.

Tintoré, J., Wang, D., and La Violette, P. (1990), Eddies and thermohaline intrusions of the shelf/slope front off north-east Spanish coast, *Journal of Geophysical Research*, *95*, 1627–1633, doi:10.1029/JC095iC02p01627.

Trasviña, A., Barton, E., Brown, J., Velez, H., Kosro, P., and Smith, R. (1995), Offshore wind forcing in the Gulf of Tehuantepec, Mexico: The asymmetric circulation, *Journal of Geophysical Research*, *100*(C10), 20,649–20,663, doi:10.1029/95JC01283.

Uchiyama, Y., McWilliams, J., and Schepetkin, A. (2010), Wave-current interaction in an oceanic circulation model with a vortex-force formalism: Application to the surf zone, *Ocean Modelling*, *34*, 16–35, doi:10.1016/j.ocemod.2010.04.002.

Viitak, M., Maljutenko, I., Alari, V., Suursaar, Ü., Rikka, S., and Lagemaa, P. (2016), The impact of surface currents and sea level on the wave field evolution during St. Jude storm in the eastern Baltic Sea, *Oceanologia*, *58*, 176–186, doi:10.1016/j.oceano.2016.01.004.

Warner, J., Sherwood, C., Arango, H., and Signell, R. (2005), Performance of four turbulence clousure methods implemented using a generic length scale method, *Ocean Modelling*, *8*, 81–113, doi:10.1016/j.ocemod.2003.12.003.

Warner, J., Perlin, N., and Skyllingstad, E. (2008a), Using the Model Coupling Toolkit to couple earth system models, *Environmental Modelling and Software*, *23*, 1240–1249, doi: 10.1016/j.envsoft.2008.03.002.

Warner, J., Sherwood, C., Signell, R., Harris, C., and Arango, H. (2008b), Development of a three-dimensional, regional, coupled wave, current, and sediment-transport model, *Computers and Geosciences*, *34*, 1284–1306, doi:10.1016/j.cageo.2008.02.012.

Warner, J., Armstrong, B., He, R., and Zambon, J. (2010), Development of a Coupled Ocean-Atmosphere-Wave-Sediment Transport (COAWST) Modeling System, *Ocean Modelling*, *35*, 230–244, doi:10.1016/j.ocemod.2010.07.010.

Weatherly, G., and Martin, P. (1978), On the structure and dynamics of the oceanic bottom boundary layer, *Journal of Physical Oceanography*, *8*, 557–570, doi:10.1175/1520-0485(1978)008⟨0557:OTSADO⟩2.0.CO;2.

Willmott, C. (1981), On the validation of models, *Physical Geography*, *2*, 184–194, URL `https://www.tandfonline.com/doi/abs/10.1080/02723646.1981.10642213`.

Wolf, J., and Prandle, D. (1999), Some observations of wave-current interaction, *Coastal Engineering*, *37*, 471–485, doi:10.1016/S0378-3839(99)00039-3.

Wu, J. (1982), Wind-stress coefficients over sea surface from breeze to hurricane, *Journal of Geophysical Research*, *87*(C12), 9704–9706, doi:10.1029/JC087iC12p09704.

Wyatt, L. (1994), The Effect of Fetch on the Directional Spectrum of Celtic Sea Storm Waves, *Journal of Physical Oceanography*, *25*, 1550–1559, doi:10.1175/1520-0485(1995)025⟨1550:TEOFOT⟩2.0.CO;2.

Xie, L., Wu, K., Pietrafesa, L., and Zhang, C. (2001), A numerical study of wave-current interaction through surface and bottom stresses: Wind-driven circulation in the South Atlantic Bight under uniform winds, *Journal of Geophysical Research*, *106*, 16,841–16,855, doi:10.1029/2000JC000292.

Young, I., Hasselmann, S., and Hasselmann, K. (1987), Computations of a Wave Spectrum to a Sudden Change in Wind Direction, *Journal of Physical Oceanography*, *17*, 1317–1338, doi: 10.1175/1520-0485(1987)017⟨1317:COTROA⟩2.0.CO;2.

Zhou, L., Wang, A., and Guo, P. (2008), Numerical simulation of sea surface directional wave spectra under typhoon wind forcing, *Journal of Hydrodynamics, Ser. B*, *20*(6), 776–783, doi: 10.1016/S1001-6058(09)60015-9.